Université de Bourgogne

Faculté des Sciences

Laboratoire Interdisciplinaire Carnot de Bourgogne

Département Nanosciences

Optical nano-antennas: passive properties and active control

Thèse présentée à l'Université de Bourgogne pour obtenir
le grade de Docteur (Mention Physique)

par

HUANG Caijin

Soutenue le 12 Mars 2010 devant la commission d'examen composée de :

Marco de Lucas	C.	Professeur, Univ. Bourgogne	Président
FELIDJ	N.	Professeur, Univ. Paris Diderot	Rapporteur
BACHELOT	R.	Professeur, Univ. de Technologie de Troyes	Rapporteur
GROSJEAN	T.	Chargé de recherche CNRS, Univ. Franche-Comté	Examinateur
CLUZEL	B.	Maître de conférence, Univ. Bourgogne	Examinateur
WENGER	J.	Chargé de recherche CNRS, Institut Fresnel	Examinateur
BOUHELIER	A.	Chargé de recherche CNRS, Univ. Bourgogne	Co-directeur de thèse
DEREUX	A.	Professeur, Univ. Bourgogne	Directeur de thèse

Acknowledgement

First of all, I would like to thank Alain Dereux for giving me the chance to work in his group. The enjoyable and active atmosphere in the group has motivated me a lot in the past three years.

I would like to acknowledge in particular my supervisor Alexandre Bouhelier who led me to the beauty world of physics and was at the origin of my research interests. There were so many differences in culture and disorders in communication. So thank you for your endurance for my countless time stupid questions. Thank you for all the advices and guidance that you gave me. I express my gratitude to Gérard Colas des Francs and Jean-Claude Weeber for answering my boring questions and simulating theoretical calculations.

A warm thank you goes to Laurent Markey, Yvon Lacroute and Juan-Miguel Arocas for their kind help in technics and Elly Lacroute for all the administrative tasks. I am grateful to Johann Berthelot, Jonathan Grandidier and Mingxia Song for resolving my difficulties during writing up this thesis.

I appreciate everyone who I work together with in the group. It is obvious that without your helps I wouldn't have been able to achieve such results.

I also thank a part of the Laboratoire de Nanotechnologie et d'Instrumentation Optique of Université Technologique de Troyes: Prof. R. Bachelot, Prof. P. Royer, Dr. A. Bruyant and Dr A. -L. Baudrion for their help in the success of my work. A special thanks goes to Miss Odile Thiéry for all she did to help me to find a PhD position and to succeed in my studies. Many thanks to all of my friends who generously give their concern and help to me which contributed indirectly to the success of my work. Their fantastic wine, delicious food and nice time we spent together will be a part of the most wonderful memory in my life.

I express my gratitude particularly to my parents, my wife and my pretty daughter. Thank you for your support and concern in not so easy times of the last seven years. I love you forever.

Contents

Chapter 1

Introduction

1.1 Nano-optics: the context

Nano-optics is an emerging field focusing on optical phenomena occurring at a scale considerably smaller than the wavelength. Very much like nano-electronics or nano-chemistry, light-matter interactions reveal unique proprieties by reducing the length scale from macroscopic to nanoscopic. The promise of nano-optics covers a broad spectrum of topics ranging from fundamental investigations to application-driven research and reaches fields ranging from physics, chemistry and biology [1, 2, 3, 4]. Without going through an exhaustive list of applications, let us mention the drive for miniaturizing integrated optical devices used in data transfer [5, 6, 7], the development of ultra sensitive optical sensors employed in a lab-on-a-chip configuration for biomedical and environmental applications [8, 9], and the quest for improving light harvesting in photovoltaic devices [10, 11, 12]. From the fundamental stand point, the combination of nano-optics with ultrafast laser spectroscopy brings the possibility to measure and control dynamic processes on a femtosecond time frame with unprecedented spatial resolution [13, 14].

Nano-optics is a counter-intuitive field. First, photons do not like to be confined; the diffraction limit imposes a lower value to the volume where free-space photons can be localized. The development of nano-optics was therefore greatly fostered by our capability to probe light-matter interactions at the relevant length scale. In this context, near-field microscopy is certainly a prime investigation tool to achieve that [15, 16, 17, 18, 19]. Second, individual dye molecules or quantum dots are typically considered to be the ultimate light sources for nano-optics because of their resolutely small size (a few atoms) and quantum properties (discrete emission lines, photon antibunching, etc...). However

these sources are intrinsically poor emitters. Despite improvement in the synthesis of dyes with a quantum yield close to unity, their absorption cross sections remain extremely low with typical value on the order of 10^{-15} cm^2. In other word, only one photon out of 1 peta is absorbed by the emitter. Furthermore, these emitters are plagued by their poor long-term stability (photobleaching) and blinking behavior (triplet incursion, surface charges) limiting thus their use in practical devices. Lastly, because these ultimate light sources are dipolar in nature, they loose their energy within a large solid angle and only a fraction of the photons emitted are potentially useful in an application-driven nano-device.

Tackling these considerations is a major research endeavor for nano-optics. In this context, optical antennas, or more generally metal nanoparticles, are interesting entities as they can bring effective solutions to the limitations listed above. As such, optical antennas are becoming a necessary unit in the nano-optics's scaffold by providing elementary devices capable of controlling light-matter interactions at the nanoscale. The work presented in this manuscript is covering some aspects in this context.

1.2 Optical antennas: a definition

An optical antenna is usually referred to metal nanoparticles and arrangement of the same. While there isn't a consensus around a precise definition, Bharadwaj *et al.* proposed the following argumentation that more or less covers the essence of an optical antenna: "a device designed to efficiently convert free-propagating optical radiation to localized energy, and vice versa" [20]. The definition above is quite broad and does not explicitly introduce the type of device nor the material. Some authors argued that because an optical cavity is localizing electromagnetic field, it should therefore be considered as an optical antenna. However, one may also argue that the sheer size of the structures in play (several wavelengths) hardly belong to the field of nano-optics and the confinement reached remains diffraction-limited since a large spectrum of wave-vectors isn't required (interference-induced localization). Let us step back in time and track the origin of optical antennas to propose a more accurate definition.

It is interesting to note that the concept of optical antenna first appeared in the context of near-field microscopy. It was introduced by J. Wessel [21] on the basis of a small metal particle receiving an incoming electromagnetic field similar to the behaviour of macroscopic radio-frequency antennas. The analogy was formally discussed by D. W. Pohl, one of the founding father of near-field optical microscopy, in a famous article entitled "near-field optics seen as an antenna problem" [22]. By comparing the similarities between opti-

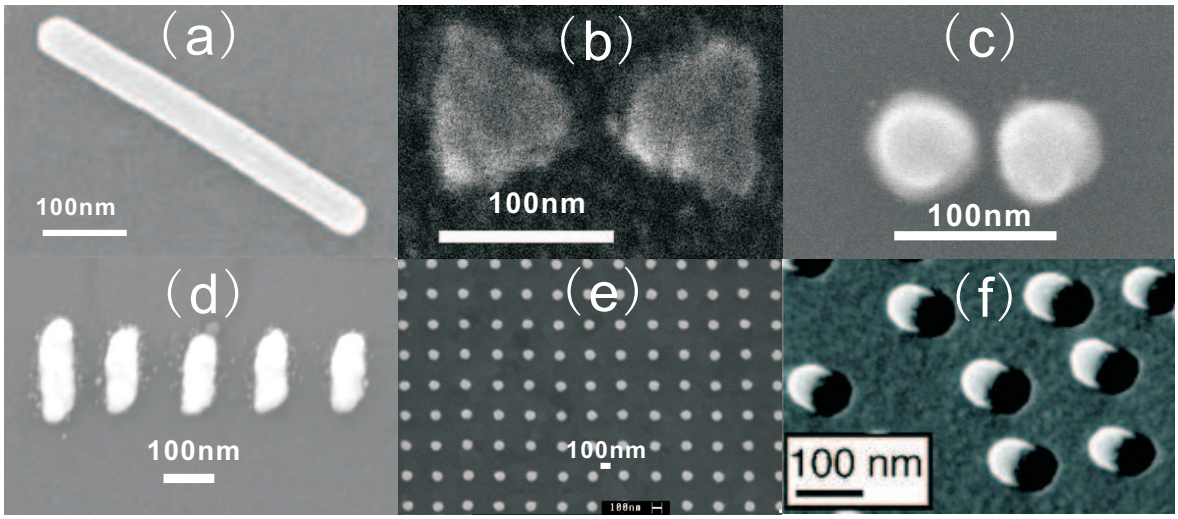

Fig 1.1: Various geometries of optical nanoantennas: (a) Nanorod [23], (b) Bow-tie [24], (c) Nanodisk dimer, (d) Yagi-Uda, (e) Array of gold nanoparticles [25] and (f) Nanocups [26].

cal near-field probes and canonical antennas, antenna theory was suggested to be applied to near-field optics. In these two seminal papers, optical antennas were discussed in terms of metal nanoparticles, essentially for their role in near-field microscopy. The underlying optical response of these nanoparticles are deeply rooted to surface plasmon resonances. To continue on the parallel between optical antennas and their radio-wave counterparts it is important to note that the properties are inferred from design parameters and are defined by a series of characteristics such as operating wavelength, bandwidth, and directivity. For optical antennas constituted of metal nanoparticles, their morphologies are also dictating the spectral position of surface plasmon resonances hence their operating wavelength. It is straightforward to see that the essential characteristics defining an optical antenna are strongly modified at the surface plasmon resonance allowing thus a form of passive control of this optical device. The capability of tuning the operating wavelength at will introduces a large number of possible designs and a few antenna geometries are reported in Fig. 1.1. The images show a series of metal structures spanning from simple geometries such as individual nanorods, to coupled units like the bow-tie, the dimer and the Yagi-Uda, and to arrays of self-similar designs like the nanocups. All these antennas have particular spectral resonances and/or polarization response and constitute a library of geometries for the designers.

Despite strong similarities between antennas operating in the optical regime and radio-wave antennas, the vast know-how acquired over the past century for roof-top devices is

not–directly– applicable to the optical spectrum by simple scaling laws. While metal can be considered as perfect for millimeter wave, absorption losses are no longer negligible in the near-infrared and visible part of the spectrum. The consequence is that an effective, shorter, wavelength taking into account material properties needs to be introduced in order to borrow standard designs rules [27]. Another point of divergence between the two operating regimes is the functionality of the antenna itself. Radio-frequency antennas are receiving and emitting devices and are essentially a transducer converting an electromagnetic field into a measurable electrical current. An optical antenna does not operate as a complete transducer; currently it merely serves as a wave-vector converter.

From the discussion above, we could tentatively provide a more general definition that the one proposed by Bharadwaj in his review paper [20]. Taking into account the concept of the directivity, we define an optical antenna as a system consisting of one or several nano-objects used for efficiently *collecting*, highly *concentrating* incident radiation and *redirecting* it in a desired direction.

1.3 The drive for optical antennas

As briefly discussed above, optical antennas were introduced to tackle some important limitations plaguing the development of nano-optics. First and foremost, optical nanoantennas are providing a means to confine electromagnetic field within dimensions much smaller than the wavelength:

Confinement

Field confinement is a distinct nature of the localized surface plasmon supported by an optical antenna. A single small metal nanoparticle is often regarded as a dipole. The consequence is that the radiated field contains a broad spectrum of wave-vectors responsible for the large confinement brought about by the structure. Figure 1.2(a) shows the extend of the near-field distribution surrounding a simple nanoparticle. The spatial extension of the field was measured by locally inducing matter migration of a photosensitive polymer. The largest response is tightly confined close to the antenna along the polarization direction indicating a high degree of confinement.

One may reasonably question how a confined field might be useful to improve ultimate light sources. There are two sides at this interrogation. First, the optical antenna is a externally driven optical source by itself and possesses unique properties. Figure 1.2(b)

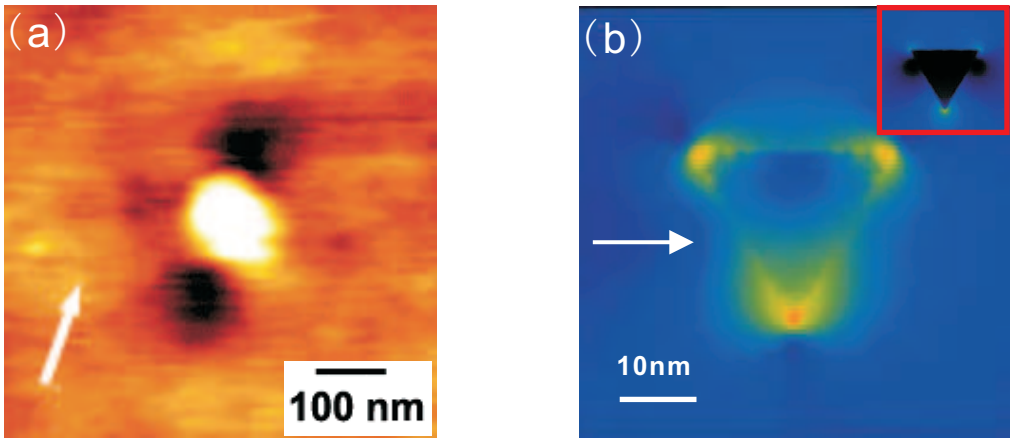

Fig 1.2: (a) Optical near-field around a silver nanoparticle through a photochemical imaging technique. A layer of photosensitive azobenzene-dye polymer covering the particle gives rise to topological deformations around the particle (dark spots) along the polarization direction (white arrow). The two dark spots result from the near field distribution in the vicinity of the particle. Image adapted from Ref. [28]. (b) Electric field intensity distribution for a silver nanoparticle (27 nm equilateral triangle) on resonance and off resonance (shown in the inset). Image adapted from Ref. [29].

shows an example of such nanosource. Here, a silver triangle excited on resonance displays 3 point-like sources located at the corners [29]. When the triangle is excited off resonance, these light sources vanish offering thus a switching mechanism between an "on" state and an "off" state simply by tuning the excitation frequency. Because nanoparticles made out of gold have large non-linear coefficient, optical nanoantennas can be used to convert radiation coherently to higher harmonics (second harmonic [30, 31], third harmonic[32, 33]) or to a white-light continuum [17, 34]. The second point towards the use of optical antennas is that they are a close to an optimized interface between free-space radiation and a quantum emitter because their respective field distribution is very close. An example is that the antennas can act as secondary nanosources to ameliorate the emission rate of a nearby emitter. For Raman scattering and fluorescence, the antenna highly confines incident radiation and couples it to the neighboring dye molecules, and then also scatters the radiation coming from the dye molecules [35]. In solar cells, by trapping incoming light, the antenna serves as a strong local source for transferring the energy into the nearby silicon layer, improving therefore the efficiency of solar cells [36, 37, 38, 39].

Another important property characterizing optical antennas is that for particular geometries, notably strongly coupled pair of particles, a dramatic enhancement of the electromagnetic field can take place. This is a distinct phenomenon which is not necessarily

searched for in radio wave antennas.

Field enhancement

At the surface plasmon resonance, the polarizability of a small particle is strongly increased. This will be discussed in more details in the main body of this manuscript. As the result, the induced dipole is also significantly increased creating thereby an enhancement of the electromagnetic field. This property is at the origin of surface-enhanced spectroscopies widely employed to boost the cross sections of very weak optical processes like Raman scattering [40, 41, 42, 43] and fluorescence [44, 45, 46], or to promote nonlinear responses [47, 48]. Optical antennas are therefore attractive devices providing a strong local field excitation for quantum emitters. The presence of the antenna typically leads to an increase in the excitation rate accompanied by an augmentation of the radiation intensity [44, 49]. For low quantum yield dyes, optical antennas can give rise to much higher fluorescence enhancements [50, 51]. The presence of the antenna also increases the nonradiative relaxation rate of the emitter because of the transfer of nonradiative energy to the antenna from the excited molecular state [52, 53]. Tam *et al.* reported an enhancement by more than a factor of 50 for fluorescent emitter by using an antenna taking the form of a single silica-gold core-shell nanoparticles [54].

The optical antenna is here playing its dual role of emitter and receiver. By interfacing a free-space electromagnetic field and providing a confined and potentially enhanced excitation, the antenna acts as an optimized receiver. The optical antenna is also serving as a scatterer to radiate the response of the molecules in the far-field. However, it is important to point out that there is a subtle balance between increasing the excitation rate of a molecule and improving its radiation outreach because these two processes are occurring at different wavelengths. The operating wavelength of the optical antenna can therefore be tuned to overlap the absorption maximum of the molecule or its red-shifted fluorescence maximum, or to be maximized in between.

It is important to mention at that point that not all optical antennas are equal in providing an important enhancement of the electromagnetic field. While all metal particles excited at resonance are able to generate an amplification, some particular geometries are able to sustain an increase of several order of magnitudes. This is particularly the case for strongly coupled pairs of nanoparticles separated by very small gaps. An example is shown in Fig. 1.3. There is a high enhancement of the field around a dimer Ag nanoparticles (36nm in diameter) separated by 2 nm excited at $\lambda = 520$ nm with the polarization

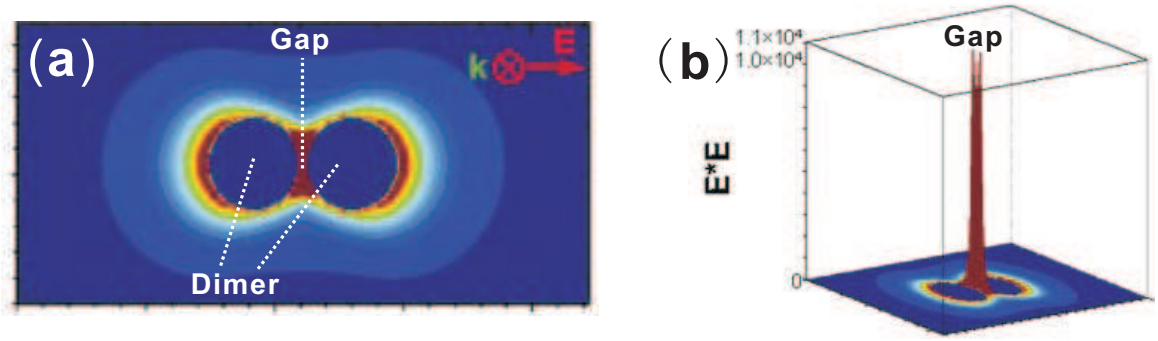

Fig 1.3: (a) E-field enhancement of a dimer of Ag nanoparticles (36nm in diameter) separated by 2 nm. (b) 3D plot of (a), the axis perpendicular to the dimer plane shows the amount of field enhancement around the dimer. $\lambda_{exc} = 520$ nm. The polarization is oriented along the dimer axis. Image adapted from Ref. [55].

oriented along the dimer axis [55]. In particular, the largest field occurring within the dimer gap is calculated 11 000 times the applied field, which is yet to be confirmed by experimental measurements.

Finally, optical antennas are completing their roles by providing a well-defined channel in which the emission of a quantum emitter can be released. In other words, the presence of an optical antenna modifies the source's emission pattern.

Radiation pattern

From general antenna theory, the directivity is a key parameter defining the characteristics of an antenna. It quantifies the power radiated by an antenna in the direction of its maximum emission normalized to the total radiated power. This is an important property to use for the control of an emitter's emission direction, which is usually radiating in a large solid angle. Taminiau *et al.* demonstrated that the fluorescence emission of a single molecule could be redirected by approaching an antenna [56] as shown in Fig. 1.4. As the antenna is 100 nm away from the dipole emitter (Fig. 1.4 (b)), the molecular emission into the glass appears a typical two-lobe pattern which is similar to the emission of a dipole oriented parallel to a dielectric interface [57]. However, while the distance between the antenna and the emitter decreases to 20 nm (Fig. 1.4 (c)), the radiation pattern changes dramatically and gives an appearance of a cone because of the interaction of the dipole and the antenna.

Furthermore, controlling the interaction between elements constituting a more complex geometry enables to modify the scattering diagram of a neighboring dipole in a manner

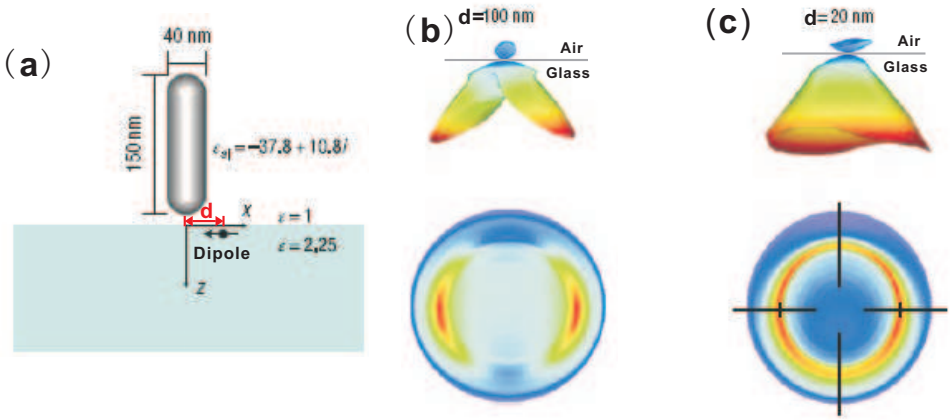

Fig 1.4: (a) A x-oriented dipole emitter is embedded in the sample 6 nm below the surface. An aluminium antenna is placed 4 nm above the surface. d represents the distance between the dipole and the antenna axis. Far-field three dimensional radiation intensity distribution (λ_{em} = 570 nm) of the dipole while (b) d = 100 nm and (c) d = 20 nm. The bottom panel is the corresponding radiation diagram in the back focal plane. Image adapted from Ref. [56].

similar to radio-wave Yagi-Uda antennas [58, 59, 60]. Figure 1.5 shows a 5-element Yagi-Uda like optical antenna proposed to redirect the emission of a nearby emitter with high directivity. The near-field coupling of the emitter and the Yagi-Uda antenna concentrates the emission in a single highly-directed lobe pattern (Fig. 1.5 (b)).

1.4 Research motivations

In the vast majorities of the work and properties highlighted above, the impact of the presence of an antenna was essentially performed by measuring the modifications of reporter molecules. The confinement is deduced by fluorescence lifetime measurements, the amount of enhancement is calculated from Raman signature, and the emission diagram is inferred from molecular responses. These examples are obviously great demonstrators, because they demonstrate the effect of the antenna directly on the end product. However, the use of probe molecules is plagued by several drawbacks. First, the optical antenna is sensitive to a modification of its surrounding environment that can lead to spectral variations of its spectroscopic response [61, 62, 63]. Second, the detected field enhancement given by optical antennas is a result of the excitation occurring at the molecular probe *excitation or emission* wavelength, not at the antennas' self resonant wavelength. Third, the inherent stability (e. g. photobleaching, blinking) as well as the interaction

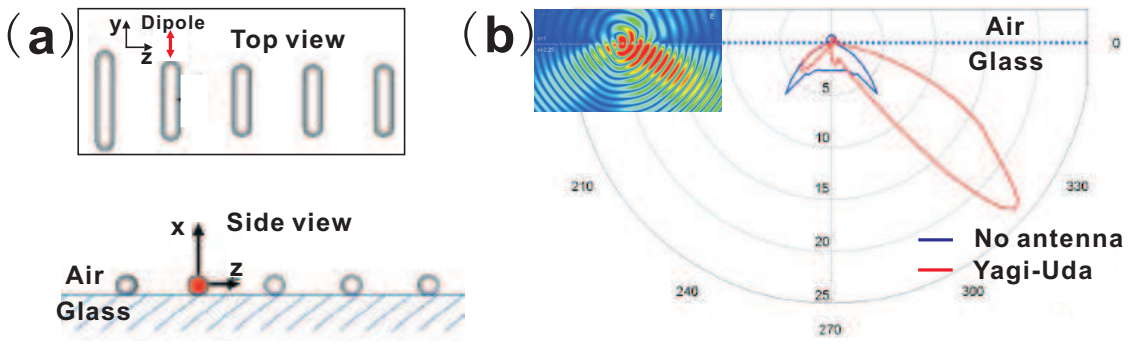

Fig 1.5: (a) A y-oriented emitter (red arrow) coupled to a Yagi-Uda antenna with a distance of 4 nm. The antenna is placed on a dielectric substrate ($\epsilon = 2.25$). (b) The angular directivity in the half space below the sample for only the emitter (blue curve) and the system (red curve) of the emitter and the antenna. Inset represents a snapshot of the local field (xz plane). Image adapted from Ref. [60].

of the emitter and the antenna should be taken into account. Because optical antennas are essentially operating in the near-field, the antenna is an inherent part of the emitter's response thus forming a coupled system. This characteristic is unique to optical antennas. The presence of a receiving radio antenna at the other side of the world is certainly not affecting the emission properties of a radio station.

Discarding the use of molecular probes is therefore a requirement to study the antennas' proper features. In this thesis, we have characterized optical antennas through their Rayleigh scattering. Rayleigh scattering is an interesting properties to investigate because it conveys the ability of the antenna to interact with light. For example, at the surface plasmon resonance the scattering cross section is enhanced and can be directly quantified. Measuring elastic scattering allows us to define the performances of optical antenna by notably determining their operating wavelength and bandwidth, their gain and scattering diagrams.

Is it is interesting to note that the characteristics mentioned above are essentially inferred from design parameters. The size and shape of the optical antenna is defining most of its properties, much like with radio-frequency antennas. However, the richness brought about by surface plasmon resonances, notably their sensitivities to the environment opens the possibility to act on the antenna. This property is also unique to optical antennas; roof-top devices are operating in air, the tunability being introduced by lump elements. So, instead of fixing the characteristics of an optical antenna by fabrication, taking profit of the properties of surface plasmons resonances allows a form of active control of an

optical antenna.

This manuscript is divided into three major parts: in the first part, we introduce the concept of the local electromagnetic density of states (LDOS) in conjunction to localized surface plasmons. These two quantities will help us to understand the scattering properties of optical antenna by measuring their differential scattering cross sections. We will describe how we measured these parameters and demonstrate our approach with LDOS mapping of optical corrals and stadiums. In the second part, we will focus our attention on individual optical antennas. These geometries considered here are relatively simple since the antennas measured are typically single particles and dimers. The typical parameters characterizing an antenna such as operating frequency, bandwidth, gain, detuning and radiation pattern are introduced, measured and compared. In the third and final part, we demonstrate an external control over the scattering properties of individual optical antennas by using an electrically-active medium. Upon application of an electrical command, we demonstrate that the detuning, gain and scattering diagram can be modified by changing the load of the antenna. Some conclusive remarks and perspectives will be given at the end of this thesis.

Chapter 2

Far-field imaging of the electromagnetic local density of states

The local electromagnetic density of states (LDOS) uniquely describes the available optical eigenmodes in which photons can exist at a specific spatial location. According to the Fermi's golden rule, it is the LDOS, not the molecular polarizability, that determines the transition rate of an emitter. In vacuum the LDOS is a constant quantity. However, the LDOS is modified in the presence of an interface, which for an emitter results in an alteration of its emission rate, emitted radiation, and the apparent quantum yield [64]. The LDOS is therefore a key parameter to understand the intrinsic optical response of nanostructures such as optical antennas, interacting with photons.

A measure of the LDOS is usually performed by indirect methods by determining for instance the lifetime of fluorescent molecules [65] or by using a point-like source such as a near-field probe [66]. However, these methods are plagued by intrinsic limitations. Notwithstanding the inherent stability of fluorescent molecules (photobleaching, blinking, ...), the determination of the LDOS around a structure is based on a random, uncontrolled location of a molecular probe [65]. To overcome this limitation, techniques employed by proximal probe microscopies were used to precisely place a small aperture at the end of a tip next to a structure of interest [66]. Here too, the approach suffers from several drawbacks. First of all, the morphology of the tip is playing an important role. Its size and symmetry define the quality of the dipolar response and it is notoriously difficult to (re)-produce a well-defined nano-aperture. Second of all, the interaction between

the aperture and the structure of interest cannot longer be neglected as their sizes are comparable thus facilitating mutual coupling.

The aim of this chapter is to obtain information about the LDOS without involving a molecular reporter and to image, in far-field, the characteristics of a series of predetermined nanostructures. To achieve this, we have developed a novel imaging technique capable of measuring the differential scattering cross section by Fourier-filtering parts of the scattered wave-vector spectrum.

2.1 Electromagnetic local density of optical states

2.1.1 Theoretical description of the LDOS

The electromagnetic local density of states (LDOS) is a fundamental quantity used widely in solid state physics. The LDOS defines the probability to detect the intensity of the electromagnetic field associated with photons of energy $\hbar\omega$ at a given position $\mathbf{r}$. The LDOS $\rho(\boldsymbol{r},\omega)$ therefore includes the sum of an electric contribution $\rho^E(\boldsymbol{r},\omega)$ and a magnetic contribution $\rho^H(\boldsymbol{r},\omega)$. Joulain *et al.* pointed out that the approximation $\rho(\boldsymbol{r},\omega) = \rho^E(\boldsymbol{r},\omega)$ can hold while the LDOS is measured at a short distance from the surface of a material sustaining surface mode (plasmon or phonon polaritons) [67, 68]. A resonance in the LDOS occurs at frequencies such that $Re[\varepsilon(\omega)] = -1$. In the context of this thesis, noble metals and incident laser frequency near surface plasmon resonances are typically used. Therefore, the total LDOS $\rho(\boldsymbol{r},\omega)$ can be replaced by $\rho^E(\boldsymbol{r},\omega)$. Finally, using multiple scattering formalism, ρ^E is easily related to the system Green tensor $\boldsymbol{G}$:

$$\rho^E(\boldsymbol{r},\omega) = \frac{\omega}{\pi c^2}\Im\{Tr\,\boldsymbol{G}(\boldsymbol{r},\boldsymbol{r},\omega)\}, \tag{2.1}$$

where $\Im$, $Tr$and c represent the imaginary part, the trace and speed of light in the vacuum, respectively. Physically, the electric field $E(\boldsymbol{r})$ scattered at $\boldsymbol{r}$ in the system by a dipole $\mathbf{P}$ located at $\boldsymbol{r}_0$ is given by

$$E(\mathbf{r}) = \frac{\omega^2}{\epsilon_0 c^2}\boldsymbol{G}(\boldsymbol{r},\boldsymbol{r}_0)\cdot\mathbf{P}, \tag{2.2}$$

where ϵ_0 is the free space permittivity. Without using any structure, that is for vacuum, the free space LDOS ρ_v^E is

$$\rho_v^E(\boldsymbol{r},\omega) = \frac{\omega^2}{2\pi^2 c^3}. \tag{2.3}$$

In the presence of a surface or a nanostructure, the LDOS is modified [69] and the change of the LDOS (*i.e.* the difference between the total and vacuum LDOS) is then:

$$\Delta\rho^E(\boldsymbol{r},\omega) = \frac{\omega}{\pi c^2}\Im\{Tr\,\boldsymbol{G}(\boldsymbol{r},\boldsymbol{r},\omega)\} - \frac{\omega^2}{2\pi^2 c^3}. \tag{2.4}$$

Equation 2.4 provides the theoretical basis to calculate and simulate the spatial variation of the LDOS. Colas des Francs *et al.* established a relationship between images obtained by scanning near-field optical microscopy and LDOS maps providing that the tip employed essentially behaves as a dipole. Figure 2.1 shows a conceptual sketch of an experiment that could determine the LDOS [70]. Owing to the vectorial character of light fields and

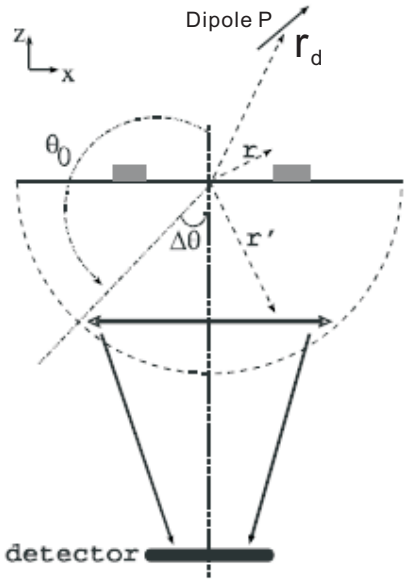

Fig 2.1: Sketch of an ideal setup of Scanning Near-field Optical Microscopy (SNOM). The sample is illuminated by a point-like dipolar light source located at $\mathbf{r}_{tip}$. The scattered light transmits through the transparent substrate and is collected with a large detection angle. Image adapted from [70].

the orientation-preferred dipole moment, the total LDOS can be written as the sum of three projected LDOS:

$$\rho^E(\boldsymbol{r}_d,\omega) = \sum_{\alpha=x,y,z} \rho^E_\alpha(\boldsymbol{r}_d,\omega), \tag{2.5}$$

in which x, y, z and r are Cartesian coordinates and the position of the dipole, respectively, and

$$\rho^E_\alpha(\boldsymbol{r}_d,\omega) = \frac{\omega}{\pi c^2}\Im\boldsymbol{G}_{\alpha\alpha}(\boldsymbol{r}_d,\boldsymbol{r}_d,\omega). \tag{2.6}$$

By assuming a dipolar source **p** oriented along one of the Cartesian axes $\alpha(x, y, z)$ (Fig. 2.1), the transmitted intensity detected in the hemisphere below the sample can establish a link with the projected LDOS [71]:

$$\boldsymbol{I}(\boldsymbol{r}_d, \omega) = \frac{\pi\omega^2}{2\epsilon_0}\mathbf{P}^2\rho_\alpha^E(\boldsymbol{r}_d, \omega). \tag{2.7}$$

Equation 2.7 indicates a proportional relation between the detected signal and the projected LDOS and opens up a feasible access to directly map the optical LDOS at a selected frequency ω. This relation holds for large detection angle and has been used by numerous authors to associate their experimental images with the underlying LDOS [66, 72, 73].

2.1.2 Mapping LDOS of optical corrals and stadiums

The presence of a surface modifies the *electronic* local density of states [74] as well as the *electromagnetic* [69]. Crommie *et al.* [75] presented for the first time images of the change of the electronic LDOS of quantum corral using a Scanning Tunneling Microscope (STM). Figure 2.2 shows spatial images of the electronic eigenstates of a circular and stadium shaped corrals constituted of iron atoms constructed on the Cu(111) surface [75, 76]. The wave function of the electrons on the copper surface were confined to the corrals. The standing wave patterns inside the structure features the interior electronic LDOS dominated by the eigenstates density sustained by the corral.

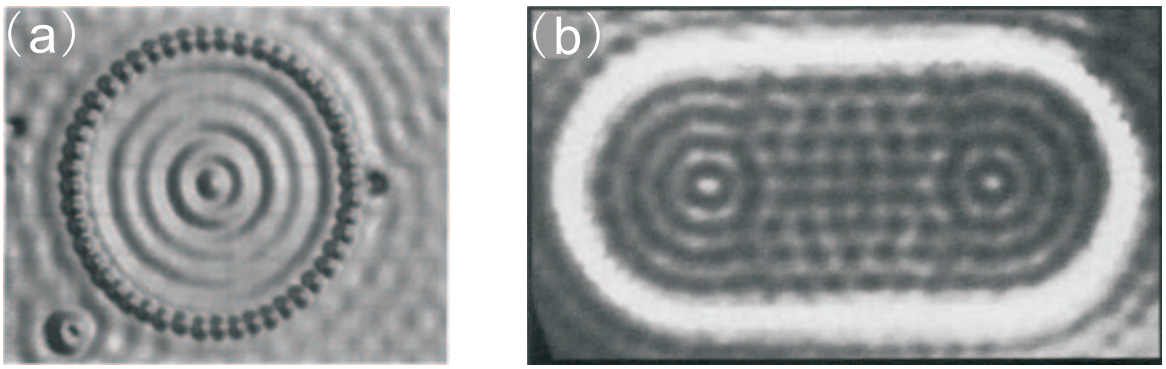

Fig 2.2: STM images of spatial LDOS variations. (a) a circular quantum corral: 48-atom Fe ring constructed on the Cu(111) surface (V= 0.01 volt, I = 1.0 nA). Diameter of the ring (atom center to atom center) is 142.6 $\mathring{A}$ [75]. (b) 76-Fe-adatom stadium of dimensions of 141 $\times$ 285 $\mathring{A}$ (V= 0.01 volt) [76]. Images adapted from Ref. [75, 76].

By analogy with STM, some authors demonstrated a link between the images obtained

by a scanning near-field optical microscope and the electromagnetic LDOS and proposed a unified formalism [77, 78]. Colas des Francs *et al.* presented numerical simulations showing the change of the electromagnetic LDOS around the optical equivalent of a quantum stadium and corral [79]. Figure 2.3 shows the calculations. The standing wave pattern of the LDOS already demonstrated in Fig. 2.2 for the electronic LDOS are also observed inside the optical structures, indicating a strong modulation of the change of LDOS. Completing the analogy, the modulation reflects the electromagnetic modes supported by the corral and the stadium.

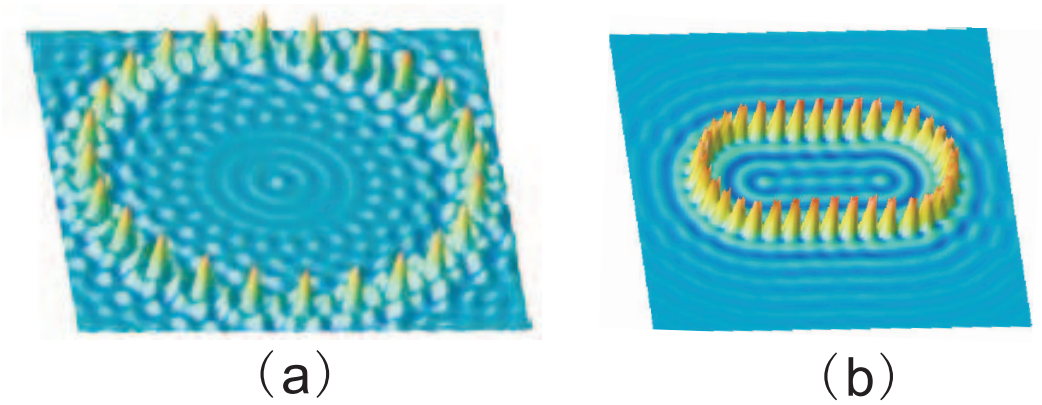

Fig 2.3: Optical LDOS simulations near nanostructures arranged as (a) a corral with a diameter of 3.6 μm and (b) a stadium. The calculations were performed at the wavelengths λ=440nm and 633nm, respectively. Each individual units is a truncated cylinder of 100nm in height and 100nm in diameter with an optical index of 2.2. Courtesy from Gérard Colas des Francs.

The first experimental electromagnetic LDOS images were observed with a "forbidden light" Scanning Near-field Optical Microscopy (SNOM) by using a near-field tip acting as a point-like source by Chicanne *et al.* [66]. In this experiment, the spatial variation of the LDOS was imaged around a stadium and a very good agreement between the theoretically predicted maps and the experimental data was obtained, especially inside the stadium. Imura *et al.* demonstrated a correlation between the expected LDOS and near-field transmission measurements performed on single gold nanorods even with a low collection angle (allowed light) [80]. It has been an issue that the signal detected with an aperture tip in Ref. [80] could be related to the magnetic contribution of the LDOS ρ^H which is in essence different to the approach of Ref. [66]. The eigenstates of semiconductor quantum dots and metallic nanostructures were also mapped by near-field techniques [81, 82, 83]. However, the interpretation of the images is difficult since the contrast can be plagued by the quality of the near-field tip, which often differs from an ideal illuminating dipole. Additionally, theoretical approaches unifying the LDOS maps

and the SNOM images neglect the cross-coupling mechanism between the tip and the structure.

2.1.3 Research motivation

The experimental setup performed by Chicanne [66] is based on Fig. 2.1 with the difference that the light transmitted below the critical angle is blocked. Detection of the radiation emitted at supercritical angles (forbidden light) leads to higher resolution imaging [84, 85]. The point-like tip acts as a source and scans over the sample. The transmitted intensity is measured and, in absence of a sample, reflects the evanescent components carried by the tip and converted by the glass interface [86]. A variation of the signals occurs when the tip is scanned over the nanostructures and represents therefore a differential measurement.

The beginning of a new project is always motivated by flaws. In our approach, discussed later on, the tip is replaced by a far-field illumination source focused by an objective. The object's LDOS is therefore not encoded in the response of a dipole and is fundamentally different to the experiment of Chicanne. It is crucial to emphasize that in our approach, a scattered signal is detected only in the presence of a structure, and the strength of the signal is directly proportional to its scattering cross-section. When the particles are excited at their surface plasmon resonance, the scattering intensity is enhanced. Before discussing further the experimental details, it is necessary to introduce a brief introduction describing surface plasmon resonances occurring in metal nanoparticles, hence optical antennas, as they will be extensively employed throughout this manuscript.

2.2 Localized surface plasmon

Surface plasmon resonances are supported by materials possessing a negative real part of the dielectric constant and a small positive imaginary part. In this thesis, we will for the most part deal with localized surface plasmons supported by metal nanoparticles. We will therefore omit of the discussion surface plasmon waves excited in extended metal films. When tiny metal particles are irradiated by an electromagnetic wave, the conduction electrons oscillate collectively thus creating a polarization on the nanoparticle. Figure 2.4(a) schematically shows the oscillation at the surface of a spherical nanoparticle as a response of a time-oscillating electromagnetic field. At a particular wavelength, the collective motion is greatly enhanced. This behavior is referred to as the surface plasmon resonance of the system. The resonance is determined by the electrons density, the ef-

fective electron mass, the shape and size of the charge distribution and the surrounding environment [87, 88, 89].

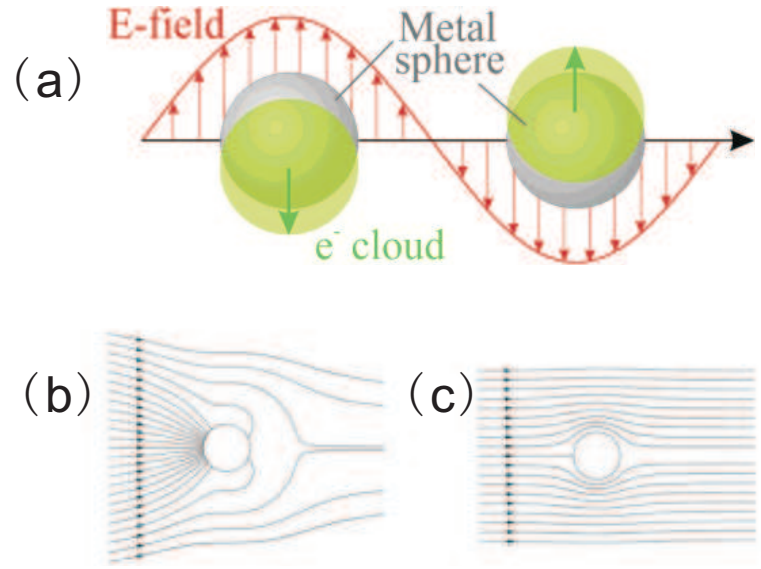

Fig 2.4: (a) Schematic of oscillation of the conduction electron cloud for a small metal sphere in the presence of an external electromagnetic field. Image adapted from Ref. [90]. (b)-(c): Distribution of field lines (excluding that scattered) surrounding a small aluminum particle irradiated by light with energy of (b) 8.8 eV and (c) 5 eV . A resonance occurs in (b), but not in (c). Image adapted from Ref. [91].

In order to relate the resonance frequency of a small particle to the dielectric constant, we assume that the particle is spherical and behaves as a dipole, that is the size of the particle (the radius a) is much smaller than the wavelength. Under these circumstances, the electric field remains quasi-constant across the particle and the interaction can be treated by electrostatics considerations. The electric field outside the metal sphere $\boldsymbol{E}_{out}$ and the polarizability of the induced dipole α are then:

$$\boldsymbol{E}_{out} = \boldsymbol{E}_0\hat{\mathbf{x}} - \alpha\boldsymbol{E}_0(\frac{\hat{\mathbf{x}}}{r^3} - \frac{3x\mathbf{r}}{r^5}) \tag{2.8}$$

with

$$\alpha = 4\pi a^3 \frac{\epsilon_m - \epsilon_s}{\epsilon_m + 2\epsilon_s}. \tag{2.9}$$

$\boldsymbol{E}_0$ is the electric field of the electromagnetic wave incident along the x-axis. $\hat{\mathbf{x}}$ is an unit vector. ϵ_m and ϵ_s denote the dielectric constants of the metal particle and its surrounding medium, respectively. A complete formalism based upon Maxwell's equations shows that the static dipole field used in Eq. 2.8 is in fact a radiating dipole. Hence, it contributes

to absorption and Rayleigh scattering by the metal sphere and their efficiencies (ratio of the optical cross-section to the geometrical cross-section πa^2) can be expressed as:

$$Q_{abs} = 4bIm\left(\frac{\epsilon_m - \epsilon_s}{\epsilon_m + 2\epsilon_s}\right) \tag{2.10}$$

and

$$Q_{sca} = \frac{8}{3}b^4\left|\frac{\epsilon_m - \epsilon_s}{\epsilon_m + 2\epsilon_s}\right|^2, \tag{2.11}$$

where $b = 2\pi a\sqrt{\epsilon_s}/\lambda$. According to Eq. 2.9, the plasmon resonance occurs when the following condition is satisfied:

$$Re(\epsilon_m + 2\epsilon_s) = 0. \tag{2.12}$$

The metal dielectric constant ϵ_m is strongly dependent on the frequency of the incident light. For a small metallic spherical particle, the resonance frequency is located in the green part of the spectrum for Au, and on the blue part of the spectrum for Ag.

Equation 2.9 is valid for the simple case of a spherical particle. For a more general shape, like ellipsoidal metal particle, the polarizability can be written as a function of a size parameter L [91, 92]:

$$\alpha_i = \frac{4}{3}\pi abc\frac{\epsilon_m - \epsilon_s}{\epsilon_s + L_i(\epsilon_m - \epsilon_s)}, \quad \sum_{i=1}^{3} L_i = 1 \tag{2.13}$$

where a, b and c are 3 semiaxes of an ellipsoid along xyz coordinate and L_i is a geometrical depolarization factor along the principal axes (x, y, z). By taking $L_1 = L_2 = L_3 = 1/3$, the polarizability reduces to that of a sphere (Eq. 2.9), as required by $\alpha_1 = \alpha_2 = \alpha_3 = \alpha$.

For large particles (e. g. Ag particle of radius 60 nm), higher-order resonance modes, especially the quadrupole are contributing to the extinction and the scattering behavior by modifying their spectral response [90]. The dipole resonance is redshifted and strongly broadens while the higher-order resonance appears at shorter wavelengths [93]. As the size of particle continues to increase, the redshift and broadening of the dipole plasmon are becoming more and more significant. A concomitant decrease of magnitude is caused by a dynamic depolarization [94] and a radiation damping effect [95] whereby the conduction electrons do not act simultaneously in phase. The effects of dynamic depolarization and radiation damping serve as the lowest-order correction to the quasi-static theory. However, they provide a transparent and inspiring way to interpret the physical phenomena occurring at the plasmon resonance. In addition, Eq. 2.8 can describe quite accurately the

near-fields at the particle surfaces for small enough particles, but radiative contributions become important at the field of 100nm away from the particle center and are not taken into account in Eq. 2.8.

Equation 2.12 also demonstrates that the resonance wavelength λ_{lsp} can be shifted by changing the local environment, for example, by an adsorbate. The variation of wavelength $\Delta\lambda_{lsp}$ can be written [96, 97, 98]:

$$\Delta\lambda_{lsp} = m\Delta n(1 - e^{-2d/l_d}), \tag{2.14}$$

where m is referred to as the bulk refractive-index sensitivity of the nanoparticle, Δn denotes the variation of the refractive index n, d is the effective thickness of the adsorbate layer, and l_d represents the length of characteristic electromagnetic field decay. While the particle is immersed in a liquid (e.g. liquid crystal in chapter 4), by assuming that the thickness d in Equation 2.14 tends to ∞ with respect to the size of the particle, we can get the linear relation between λ_{lsp} and n which has also been observed in Ref.[99, 100].

2.3 Experimental methods

Let us turn our attention to the main experimental methods used in this thesis. Since the antennas are small objects compared to the wavelength, their interactions with light are weak. Typical scattering cross sections are on the order of $10^{-16}m^2$ for small particles [101, 102, 103] at resonance and are therefore difficult to measure in presence of a large background.

To address this issue, we have developed a modified confocal microscope to retrieve the scattering responses of individual optical antennas. A schematic is depicted in Fig. 2.5(a). Our measurement platform is based on an inverted microscope. The illumination is provided by either a series of lasers spanning the green, red and near-infrared spectrum. The lasers are fiber-coupled to bring the light to a diascopic arm used for excitation of the optical antenna. The arm is composed of a combination of a polarizer and a wave plate to adjust the orientation of the outgoing polarization. The diascopic arm is then terminated by a low numerical aperture objective (N.A.=0.65) employed as a focusing element. The estimated excitation spot is on the order of the wavelength used. The reason we used a weak focalization will become clear in the following.

Our detection path essentially relies on the combination of a high N.A. objective (1.45) and a beam stop. The latter being merely an aluminum disk placed in the Fourier plane of the microscope and therefore acts as a spatial filter. The diameter of the disk is chosen

such that it rejects the light angularly distributed below the critical angle. Only the signal emitted between the beam stop and the largest numerical aperture (here 1.45) is detected by a photomultiplier in a confocal arrangement.

It is important to note that the focal spot of the excitation and the detection spot spatially overlap at the sample plane in three dimensions. The sample is placed on a x, y piezoelectric scanner and can be precisely positioned in the foci. In absence of structures, no signal is detected because the angular distribution of the illumination is rejected by the beam stop. It is only when a structure is present that a signal is recorded. The signal is arising from high angular regions and is therefore linked to the scattering characteristics of the sample under investigation. Since we used a detection window higher than the critical angle and the illumination is entirely rejected, the majority of the signal must originate from converted evanescent components associated with the structure.

In some particular occasions, notably during alignment and calibration procedures described later in the text, the setup depicted in Fig. 2.5(b) was used. Instead of relying on a low-N.A. diascopic illumination, an episcopic illumination was utilized whereby the high N.A. objective was employed for the excitation and the detection. The apparatus operates therefore in a back-reflection mode, the Fourier filtering with the beam stop remaining the same as in Fig. 2.5(a). From the detection point of view, this particular configuration resembles the one used by Chicanne *et al.* to measure the LDOS in that the information results from a differential measurement: there is always a detected signal even without the presence of a structure.

2.3.1 Imaging characteristics of our apparatus

To characterize the imaging properties of our apparatus, we introduce at that stage the concept of the point-spread function (PSF) of a microscope. The PSF of an optical system maps the three-dimensional intensity distribution resulting from a single point source in the object plane of the microscope. Even if the source is an ideal point, the image is not because of aberrations in the optical system spreading the image over a finite area (blurring), and diffraction effects. The process of imaging can be formulated using the convolution of the PSF and the real light source (or object), which shows the linear

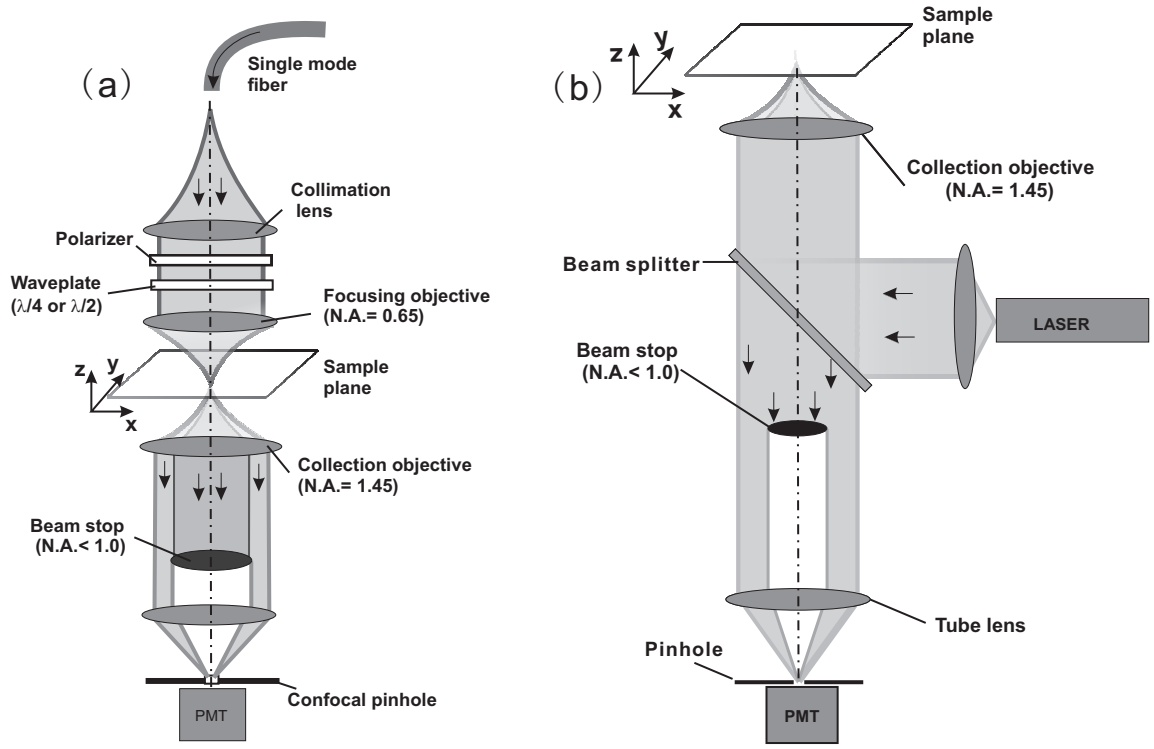

Fig 2.5: Experimental schemes. (a) Diascopic illumination: the structures are illuminated by a focusing objective (0.65 N.A.). The scattered components and the directly transmitted signal are collected through a large detection angle by a high N.A. oil-immersion objective (N.A.=1.45). A beam stop removes the signal radiated below the critical angle whereas signal emitted above is detected by photomultiplier (PMT). (b) Episcopic illumination: the high N. A. objective is used for excitation and for detection. The beam stops plays the same role of selecting the signal emitted above the critical angle.

property of the optical imaging systems. The formula is given by [104]:

$$i(x,y) = \int\int_{-\infty}^{+\infty} O(\xi,\eta)h(x-\xi,y-\eta)\mathrm{d}\xi\mathrm{d}\eta, \tag{2.15}$$

where $i(x,y)$ and $O(\xi,\eta)$ are the functions describing the image and the object, respectively. The term $h(x-\xi,y-\eta)$ represents the PSF, and is the Fourier transform of the aperture function of the pupil when illuminated by coherent light. Figure 2.6 (a) and (b) show a computed PSF in a case of point-like source in a $x-z$ plane parallel to the propagation (axial) and in a lateral $x-y$ plane. In both planes, the image of the source is convoluted by the response function of the instrument.

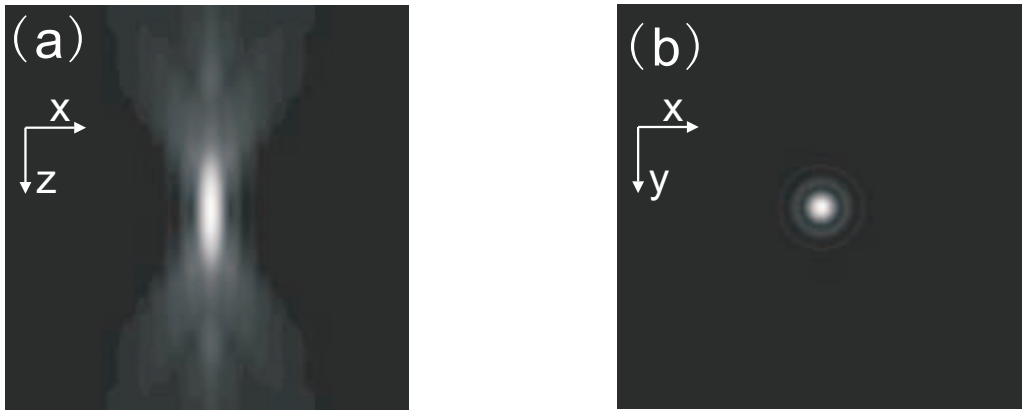

Fig 2.6: (a)-(b): Computed sections (dimensionless representation) of an ideal point source of the three-dimensional PSF (a) in $z-x$ (axial)-direction, and (b) in $x-y$ (lateral) direction in the absence of beam stop. Image adapted from Ref. [105].

Imaging single colloidal gold nanoparticles

Preliminary experiments were performed on single colloidal gold nanoparticles to gain further information of the intrinsic optical response of our microscope. Incidentally, this type of nanoparticles forms the simplest kind of optical antennas. The measurements described below are not only interesting from the point of view of the microscope but give insights on the scattering properties of simple optical antennas.

The gold nanoparticles (diameter 80 nm) were randomly deposited on a glass substrate covered by a very thin layer (< 30 nm) of indium tin oxide (ITO). The ITO layer is a conductive, optically transparent material compatible with scanning electron microscopy (SEM). A SEM micrograph of a selected region of the glass sample is shown in Fig. 2.7 (a) where four individual nanoparticles are visible. Figure 2.7 (b) is an image of the same sample area but acquired by our confocal microscope with a diascopic illumination. A nearly one-to-one correspondence with Fig. 2.7 (a) is observed. The excitation wavelength was fixed at $\lambda = 532$ nm with a polarization indicated by the black arrow on the bottom right of the image. At the location of the nanoparticle, we observe a bright contrast corresponding to an increased intensity surrounded by concentric rings on an otherwise constant background.

We understand the detected signal as being a measure of the integrated differential scattering cross section (DSCS) characterizing the nanoparticles. The DSCS represents the probability to observe a scattered photon per solid angle unit. The term 'differential' is referred to as $\mathrm{d}I/\mathrm{d}\Omega$, where I and Ω represent scattered intensity and solid angle (Fig. 2.8).

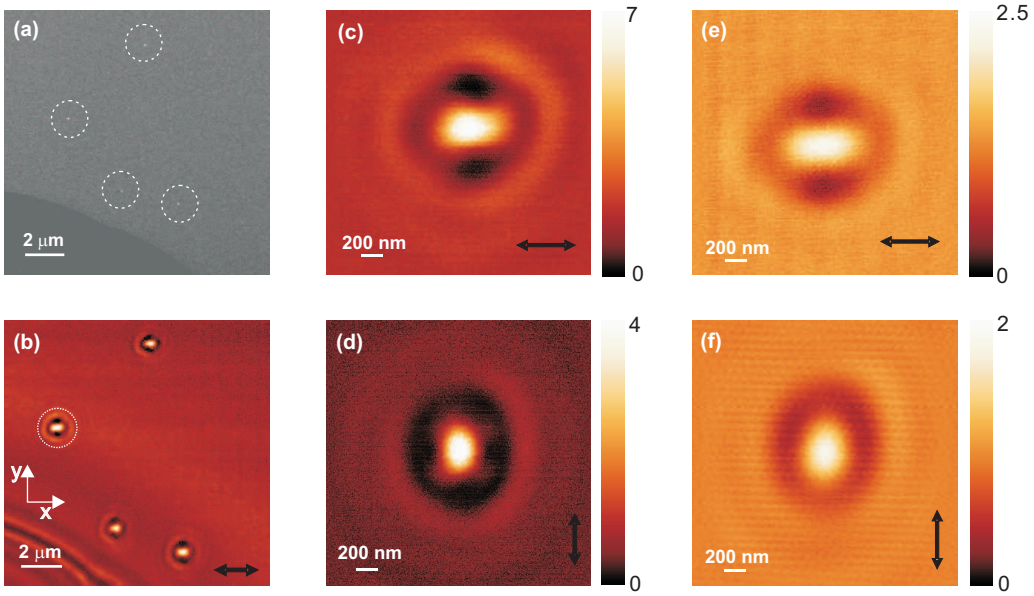

Fig 2.7: (a) Scanning electron micrograph of a selected zone showing 4 individual gold colloids nanoparticles (80nm in diameter) circled by dashed lines. (b) Scanning confocal micrograph of the same selected zone via a diascopic illumination and a beam stop (Fig. 2.5(a)). (c)-(d) close-up images of a selected single particle (circled in (b)) under two orthogonal polarizations (arrows). (e)-(f) were obtained by removing the beam stop. λ_{exc}=532nm.

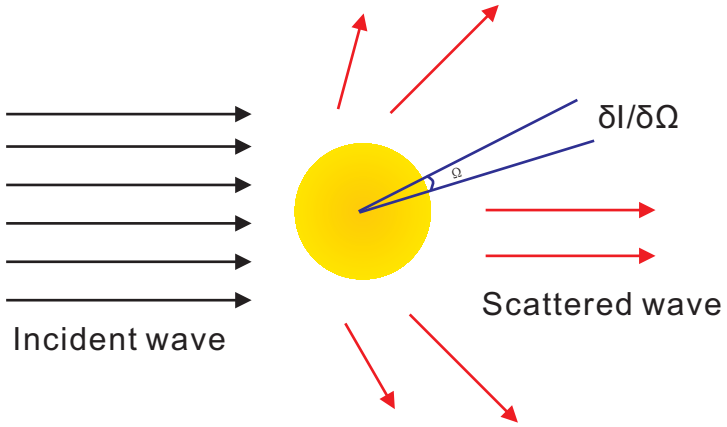

Fig 2.8: Illustration of the differential scattering cross section ($\mathrm{d}I/\mathrm{d}\Omega$) of a small particle. I and Ω are scattered intensity and solid angle, respectively. Black and red arrows represent the external and the scattered fields, respectively.

In our case, the integration runs over a limited solid angle bound by the beam stop for the lower angles and by the N.A. of the detection objective for the largest one. The signal reflects therefore only a partial DSCS. It is also understood that intensity distribution

does not reflect the intrinsic response of the nanoparticles, but the point-spread function of the microscope.

Figure 2.7(c) and (d) are close-up images of an individual particle for two orthogonal incident polarizations. We observed a slight asymmetry of the pattern oriented with the polarization. This is due to the inhomogeneous field distribution inside the focal region. In comparison, a similar pattern was found in Fig. 2.7(e) and (f) by moving away the beam stop. The background is now more important because the direct illumination is collected, thus reducing the contrast of the intensity scattered off the nanoparticle. It is important

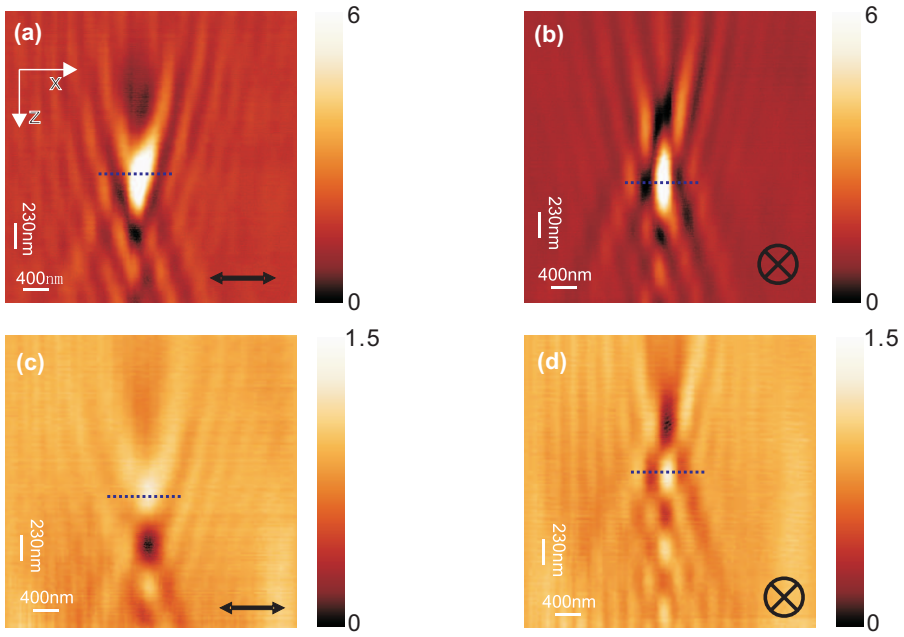

Fig 2.9: Axial confocal scanning micrographs ($x-z$ plane) of a single gold nanoparticle. (a)-(b) were obtained for two orthogonal polarizations (black arrows). (c)-(d) were obtained for the same polarizations but without the beam stop. The focus of the collecting objective is located around the dashed line. λ_{exc}=532nm.

to point out that the intensity distribution is very sensitive to the axial position of the focus of the collection objective. We conducted a x, z scan to measure the axial intensity distribution. Figure 2.9(a)-(b) show images of the integrated DSCS for a constant y-axis taken through the center of the nanoparticle and for two different polarizations. The z-direction was varied by using a piezoelectric actuation of the collection objective for a fixed position of the excitation objective. The images show a bright rod-like elongated structure indicating the vertical extend of the point spread function of this excitation/collection scheme. The position of the optimal focus of the collecting objective is located around

the dashed lines in Fig. 2.9. Figure 2.9 (c)-(d) were taken under the same experimental conditions but without the beam stop. The contrast is naturally reduced and essentially shows the same general pattern that the patterns obtained with the beam stop. This is an important fact as the partial detection of the DSCS with our spatial filtering does not a priori reduce the information contained in the images.

For the sake of comparison, we have also observed the response of the same set of gold particles by using the episcopic mode depicted in Fig. 2.5 (b). Figure 2.10 (a) and (b) show the result of the scan for the two polarizations considered. A dark contrast is now observed at the location of the particles as it can be seen in the close up image of Fig. 2.10 (c). We understand this dark contrast as the interference of the reflected field

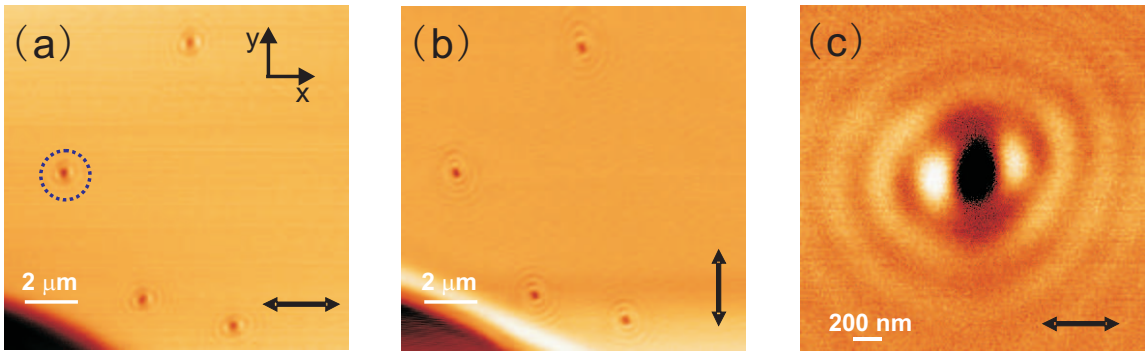

Fig 2.10: Confocal scanning micrograph (x, y plane) via the episcopic illumination mode without the beam stop under two orthogonal polarizations (arrows). (c) is a close up image of the selected particle enclosed by a blue circle in (a).

and the scattered field by the particle. At the glass/air interface, the reflected field E_r for the incident angle above the critical angle experiences a phase shift of $-\pi/2$ with respect to the incident field E_i [106]. This can be formulated as $E_r = rE_i e^{-\pi/2}$, where r denotes the reflection coefficient. For a spherical nanoparticle (diameter $D \ll \lambda$), the scattered light propagates as a spherical wave and interferes with E_r. The scattered field can be expressed as $E_s = sE_i$ where $s = |s|e^{i\varphi}$ is the complex scattering amplitude with phase φ [107] and is proportional to the polarizability of the particle. The measured intensity I_m can be written as [108]:

$$I_m = |E_r + E_s|^2 = |E_i|^2(r^2 + |s|^2 - 2r|s|\sin\varphi). \tag{2.16}$$

The first term in Eq. 2.16, related to r^2, is simply treated as the background intensity. The second term proportional to $|s|^2$ is associated with the scattering signal and scales as D^6. The last term is a function of D^3. The second term changes faster than the last term

as the particle diameter varies. There is therefore a subtle balance between the second and the last terms. For large particles, the second term dominates and the particles appear brighter than the background. Whereas, for small particles, the last term becomes more important and the particles appears darker than the background.

2.3.2 Conoscopic imaging

Conoscopy refers to an imaging technique employed to measure the intensity of light distributed at the back focal plane of a microscope objective. This particular plane corresponds to the so-called Fourier plane of the lens system. It is well-known that a lens acts as a Fourier transformer [109, 104]: the electric field distribution located at the focal plane is Fourier-transformed by a lens at the back focal plane.

All the scattered waves in object plane maintain their phase and amplitude relationships in the Fourier plane. Therefore, a screen or a charged-couple device(CCD) placed at Fourier plane can image the angular intensity distribution and give important parameters of scattering, notably the distribution of wavevectors $\boldsymbol{k}$.

By using an aplanatic, infinity-corrected objective, the angular distribution of emission is converted into a circular intensity distribution in the back focal plane. A linear relationship exists between the sine of the angle θ of emission emanating from the collecting objective's focus and the radius r (distance between the optical axis and the point of interest at the Fourier plane [110]:

$$r = fn\sin\theta, \tag{2.17}$$

where f is the focal length of the objective. Accordingly, the N. A. ($nsin\theta$) or wavevector k is proportional to r in the Fourier plane. This results in a conversion of angular emission distribution to an intensity distribution over the Fourier plane and a direct measurement of the wavevectors scattered at the object plane. In a standard inverted microscope, the back focal plane for high N.A. lens is situated inside the body of the objective. To access the back focal plane, a Bertrand lens is usually inserted before the eyepieces. To project the plane outside the microscope a series of relay lenses are typically employed [111, 112]. A schematic representation of the setup retrofitted for conoscopic observation is depicted in Fig. 2.11. A couple of relay lens placed after the tube lens of the microscope were appropriately placed to project the complete Fourier plane onto the chip of a CCD camera.

For calibration purposes, a 633 nm laser beam was focused onto a glass/air interface by the diascopic arm (0.65 N. A. objective). A 532 nm laser was simultaneously sent to the

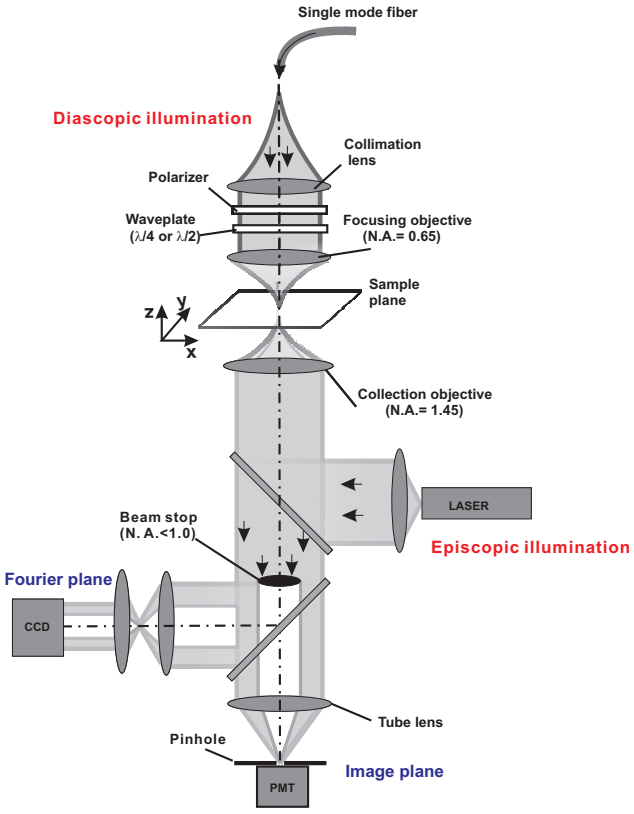

Fig 2.11: Experimental setup for conoscopic observation.

episcopic path and was focused by the oil-immersion objective. Figure 2.12 (a) shows the image acquired by the CCD camera. A green ring is visible in the image of Fig. 2.12(a). This ring arises from the total internal reflection (TIR) of the 532 nm laser beam following the episcopic path. The inner edge of the ring represents the critical angle (N.A.=1.0) of TIR while the outer edge of the ring is given by the N.A. of the oil-immersion lens, that is 1.45. This illumination mode is particularly convenient to adjust the position of the relay lenses and calibrate the Fourier plane.

The calculation of the value of N. A. in the Fourier plane is based on the linear relation between r and the N.A. as shown in Eq. 2.17 by considering the N. A. value of the critical angle (denoted as N.A.$_c$) being 1. If r_0 (Fig. 2.12 (a)) represents the radius corresponding to the critical angle, the N.A. value of a given radius r' at the Fourier plane can be written as N.A. = N.A.$_c \times r'/r_0 = r'/r_0$. Superimposed to the green annulus, a red disk at the center of the Fourier plane is also visible. The disk represents the signature of the diascopic illumination. Using the considerations discussed above, the diameter of the red disk is estimated to be about 0.61, a number slightly smaller than the value specified by

the manufacturer.

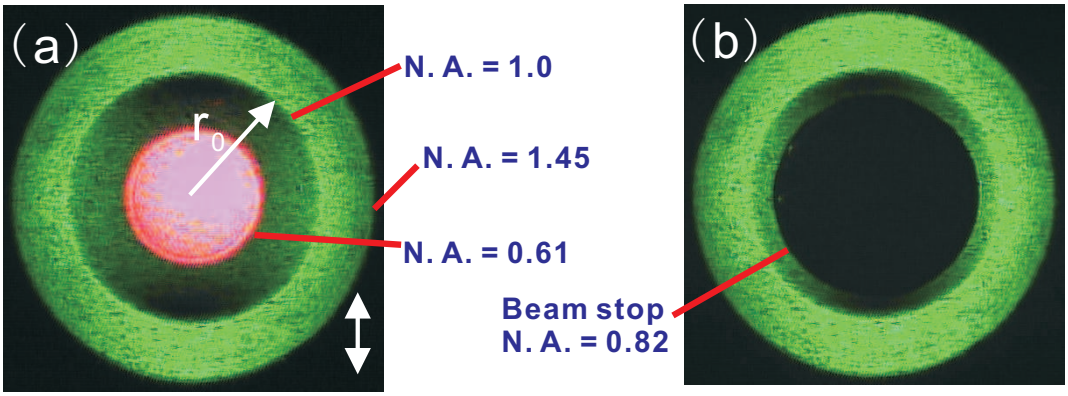

Fig 2.12: Conoscopic images obtained with an episcopic illumination ($\lambda = 532$nm) and a diascopic illumination ($\lambda = 633$nm). (a) without a beam stop. (b): with a beam stop blocking the diascopic illumination.

Figure 2.12 (b) shows the image of the Fourier plane when a beam stop is in place thus rejecting the illumination wavevectors. Here, a beam stop with a diameter corresponding to a N.A. of 0.82 was used. It is clear from the image that the beam stop plays its blocking role: there is no evidence of a red contribution in the Fourier plane.

Radiation patterns of a dipole

At that point it is important to note that the Fourier plane depicted in Fig. 2.12 was obtained without any structures and had the only purpose of adjusting and calibrating the conoscopic mode. What can we expect in the presence of nanoparticles? At first approximation, a nanoparticle much smaller than the wavelength can be considered as a dipole. The validity of this statement will be experimentally confirmed later on. In free space, a dipole always shows a spindle like far-field radiation pattern aligned perpendicularly to its moment orientation as depicted in Fig. 2.13(a). However, for a dipole emission close to an interface, the power distribution of a dipole changes dramatically and a significant portion of the dipole emission is emitted in the glass substrate, especially around the critical angle θ_c. Figure 2.13 (b) to (d) show the modified emission diagram for a dipole oriented in the plane of the interface and for an orientation normal to the interface. The emission patterns are calculated in the back focal plane of a microscope with a high N. A. objective (see Ref.[113]).

It is clear from this discussion that the radiation emitted in the superstrate can be reasonably omitted since most of the dipole radiation is transferred inside the highest

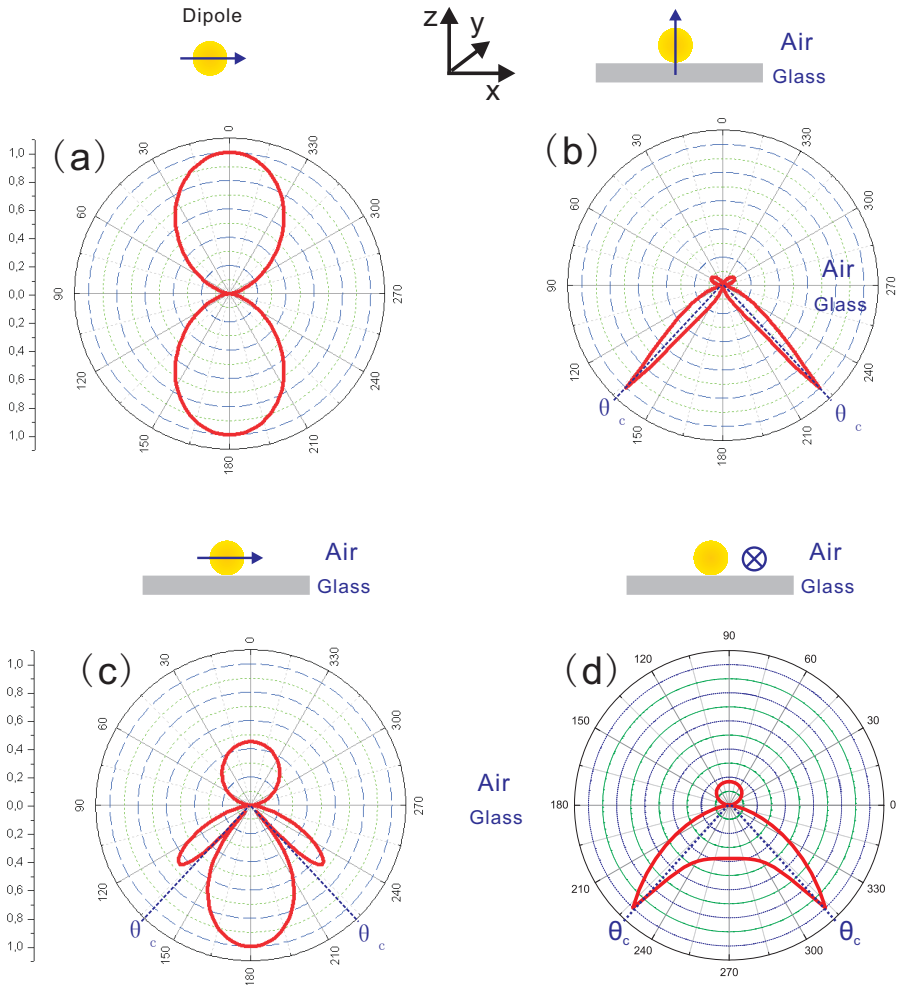

Fig 2.13: Calculations of the intensity distribution of a dipole placed (a) in free space and oriented in the x, y plane. (b) The dipole is placed at a air/glass interface and is oriented along the x-direction and (c) along the z-direction. The upper panels indicate the orientation of the dipole moment (black arrows) and its surrounding medium. The calculations (method see Ref.[113])were courtesy provided by Dr. A. Bruyant (LNIO-UTT) and Dr. G. Colas des Francs.

dielectric medium [114]. Furthermore, propagating and evanescent components of the dipole emission are angularly separated in the glass substrate by θ_c (N.A.=1) [86]. Since most of the portion situated below θ_c is removed by a beam stop, the detected signal originates therefore from the evanescent components of the scattered spectrum converted by the substrate.

2.4 Far-field imaging of optical corrals and stadiums

In this section, we will validate our approach by measuring the optical response of an arrangement of nanoparticles. We have chosen two well-know configurations for the measurement: corrals and stadium constituted of individual gold nanoparticles. The choice over these two designs was motivated by the facts that they were already characterized experimentally by Chicanne *et al.* [66] using near-field techniques and were also numerically investigated by Colas des Francs [79] in terms of the LDOS and could serve therefore as a point of comparison with our results.

The samples were fabricated by electron-beam lithography. Briefly, the procedure is detailed as follow. A 300nm-thick layer of PMMA (Polymethyl Methacrylate diluted in Cholorobenzene) was deposited on an ITO-covered glass substrate by spin-coating. After a bake out of the sample to remove the excess of solvent, the pattern was inscribed in the resist by electron-beam lithography. The sample was then developed to expose the patterns prior to metal deposition. A typically 70nm thick gold layer was thermally evaporated on the sample. The remaining PMMA layer was then lift-off to reveal the final structures. A micrograph of a fabricated structure is shown in Fig. 2.14 where a series of individual gold disks are arranged to form a corral.

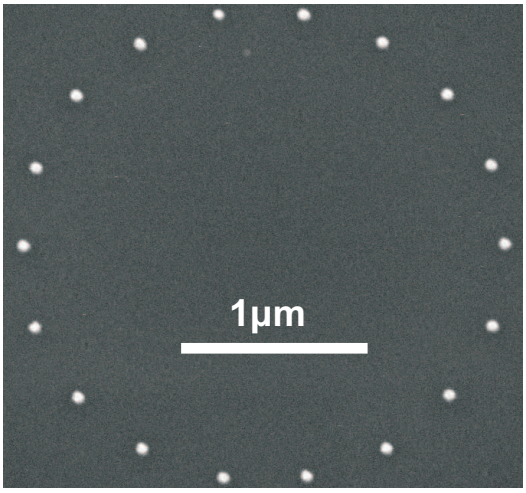

Fig 2.14: Scanning electron micrograph of a corral-like structure fabricated by electron-beam lithography. The corral is constituted of 18 gold nanoparticles. The corral and the particles are 2.5μm and 80nm in diameter, respectively

2.4.1 Optical corrals and the LDOS

The type of structure depicted in Fig.2.14 is optical arrangement analogous to electronic quantum corrals [79]. To mimic the formation of the optical corral, we have fabricated a series of structures showing a step-by-step construction of the complete optical corral. Figure 2.15(a)-(c) show micrographs of the four different phases of construction starting from a random arrangement of the nanoparticles to a final corral.

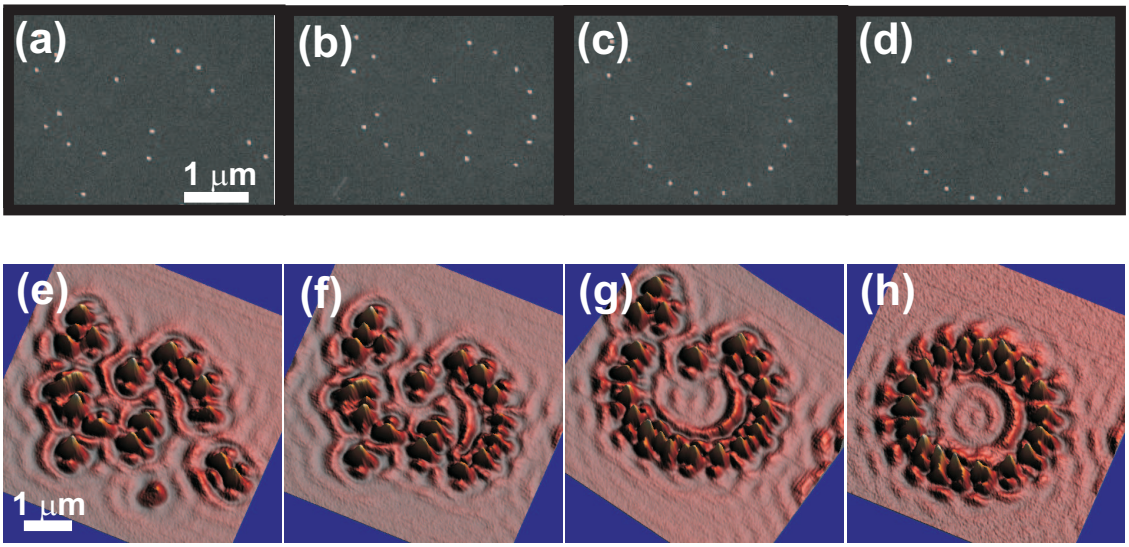

Fig 2.15: (a) to (d) Scanning electron micrographs corresponding to a step-by-step construction of optical corral. (e) to (h) are three-dimensional rendering of the experimental confocal images corresponding to the construction phases. The excitation wavelength is λ=633nm and circularly polarized. The particles are identical (70 nm diameter and 50 nm height).

Figure 2.15(e)-(h) show the images obtained with our microscope at an excitation wavelength of 633nm and a circular polarization. An increase of intensity is occurring at each particle as a result of the converted evanescent signal and the rejection of the illumination wave vectors. Surrounding each particle, the spatial variation of differential scattering cross-section displays concentric rings that were recognized at typical modulation of the LDOS [79], albeit convoluted by the point spread function of the apparatus (diffraction-limited). Figure 2.15(h) shows the distribution issued from the completed corral. Interestingly, we observe a significant modulation of the DSCS inside the corral, notably a bright maximum right at the center of the corral. A two-dimensional representation is shown in Fig. 2.16(a). It is important to point out that the diameter of the illumination region is estimated at $\sim$1200nm for an excitation wavelength λ=633nm. When the particles are scanned through the focus, a number of them are illuminated

simultaneously, while the confocal detection picks them individually. At the center of the corral, the particles are approximately 1μm away from the illuminated region, and the detection collects on a location where no particles are present, yet a signal is detected!

Following the full multiple scattering formalism [79], we calculated the total LDOS $\rho(\mathbf{r})$ 100nm above the corral. The two-dimensional distribution of the LDOS is shown in Fig. 2.16(b). We observe a large LDOS at the site of the particles, together with a series of concentric rings inside the corral that recall the modulation of the experimental differential scattering cross section (DSCS). The correlation between the modulation of $\rho(\mathbf{r})$ and the experiment is illustrated in Fig. 2.16(c). The experimental data (blue circles) are offseted for clarity. Figure 2.16(c) shows that our measurement is in qualitative agreement with the pattern of the calculated LDOS. In particular, the period of the internal concentric rings is measured at 350nm on both graphs suggesting a significant angular emission inside our detection (no important wavevectors are missing).

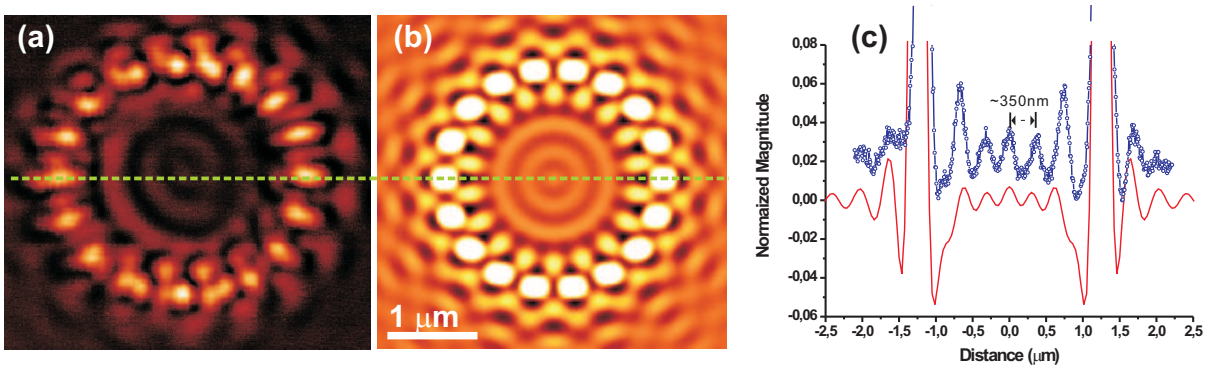

Fig 2.16: (a) Experimental (λ = 633 nm with circular polarization) and (b) calculated LDOS $\Delta\rho^E$ at 100 nm above the complete corral. (c) Experimental (blue circles) and calculated (red solid) profiles taken along the dashed lines in (a) and (b). The broken zones in the curves in (c) are due to the magnitude of the LDOS diverging on the particle.

Our measure is in quantity different from the LDOS because a complete measurement of the LDOS is possible only if all the modes allowed by the structures are excited and the detection is integrated over a large solid angle [70]. Our approach makes an attempt to partially fulfill these two requirements, but some limitations remain.

First, as the result of excitation, the scattered field consists of a wavevector distribution dictated by the diffracting characteristics of the object, *i.e.* its differential scattering cross section. For small particles, the scattered wavevector spectrum is broad and contains both propagation and evanescent components. This scattered wavevector continuum provides

an efficient excitation source to populate the allowed intrinsic optical modes of the object itself, very much like what a dipole would do. However, not all the modes are accessible by our approach in particular the higher-order modes are likely to remain unpopulated by our illumination scheme [115]. Second, although the scattered signal is mainly distributed at the critical angle [86] (Fig. 2.13), the part that is tightly bound to the surface is not converted by the glass interface and is therefore not detected. Finally, the portion of transmission blocked by the mask is also missing in the total DSCS. Despite a non ideal excitation, *i.e.* a finite spectrum of wave vectors and a partial integration of the differential cross section, the most dominant modes of the corral are excited and detected by our approach. Although our approach cannot render a quantitative image of the LDOS, it provides with a rapid and easily-implemented qualitative measurement describing the main characteristics of the LDOS. Our approach avoids some disadvantages brought by the near-field imaging with the tip [66] such as the tip shape and the tip-sample interaction.

For the sake of comparison , we also measured the corral with the episcopic illumination mode of Fig. 2.5(b). Figure 2.17 shows a "negative" contrast at the position of particles already mentioned in Fig. 2.10. Importantly, there is no evidence of a modulation inside the corral demonstrating the uniqueness of the signal collected by our approach.

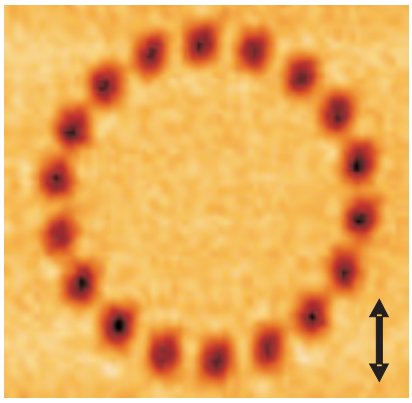

Fig 2.17: Experimental image of the corral via the episcopic illumination mode (λ=532nm) without a beam stop.

2.4.2 Optical stadium and projected LDOS

We then investigated a polarization-sensitive structure taking the form of an optical stadium. The stadium structure consists of 34 identical gold particles. The long and short axis are 4 μm and 2 μm, respectively. A micrograph is shown in Fig. 2.18. The excita-

tion wavelength λ used is 532nm with a linear polarization oriented along either of the principal axis of the stadium.

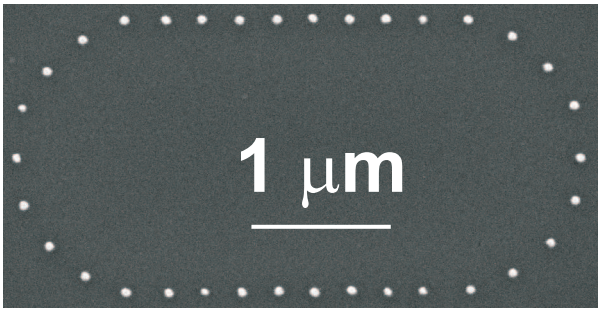

Fig 2.18: Scanning electron micrograph of an optical stadium constituted of 34 gold particles (thickness: 50nm thick; diameter: 70nm). The long and short axis are 4μm and 2 μm, respectively.

Figure 2.19(a)-(b) show the experimental mapping of the stadium's differential scattering cross section for a polarization oriented with the long and short axis, respectively. Similar to corral, we observe a significant modulation of the DSCS signal inside the stadium for the two state of polarizations, but significant differences on the pattern are visible. In particular, the stadium's foci are well emphasized for a polarization oriented with the short axis (Fig. 2.19(b)).

To have a better insight into the mechanism of LDOS reconstruction, we analyzed the image formation of our setup using the reciprocity theorem [116]. The theorem implies that the signal recorded with the experimental setup shown in Fig. 2.5(a) is strictly equivalent to the signal measured when the illumination and detection positions are exchanged. Therefore, we consider the reciprocal system in which the sample is illuminated isotropically from the substrate by a N.A.=1.45 lens with an incoherent source having both TE and TM polarizations [116]. Figure 2.19(c)-(d) represents the square modulus of the x and y components of the electric field $|E_x|^2$ and $|E_y|^2$. The calculation was performed 100 nm above the stadium, and according to the reciprocity theorem, with the oil-immersion objective excitation. Within the constraint imposed by the diffraction limit, these intensities are similar to the signal detected by the N.A.=0.65 lens.

Figure 2.19(e)-(f) show the projected LDOS $\rho_x(\mathbf{r})$(resp. $\rho_y(\mathbf{r})$) calculated 100 nm above the surface which were obtained by orienting a point-like dipolar source along the x (resp. y) direction [117]. The intensity distribution of the electric field $|E_x|^2$ (resp. $|E_y|^2$) reproduces the main features, notably the inside modulations, of the calculated projected LDOS. Good agreement between the two calculated quantities indicates that the reciprocal illumination efficiently excites the dominant modes of the structure. Furthermore,

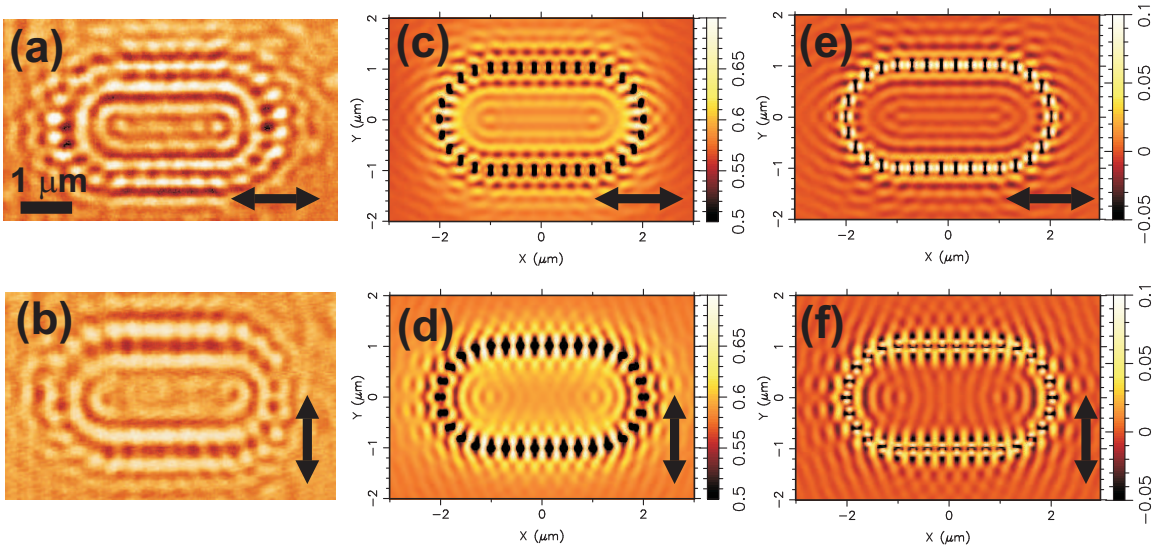

Fig 2.19: (a-b) Experimental images of the stadium's DSCS for two orthogonal polarizations. The arrows indicate the polarizations. (c-d) $|E_x|^2$ and $|E_y|^2$ intensities calculated 100 nm above the surface, respectively. (e-f) Normalized projected $\Delta\rho_x^E(r)$ and $\Delta\rho_y^E(r)$ LDOS calculated 100 nm above the surface, respectively.

because the intensity and the projected LDOS concur, inserting a polarizer in the initial (nonreciprocal) setup should reproduce the projected LDOS with respect to the polarizer orientation. The inner modulation of the intensity and the projected LDOS resembles the experimental images: the weak modulation inside the stadium for a polarization along the short axis is reasonably reproduced in all images. Some discrepancies are visible at the location of the nanoparticles, indicating that some higher-order modes are either not excited or not detected. By using the reciprocity theorem, we conclude that the modes populated in the structure can be efficiently collected by the 1.45 N.A. objective in the nonreciprocal experimental setup of Fig. 2.5(a).

To compare our data with LDOS measurements taken by near-field technique, we reproduce in Fig. 2.20 the images obtained by Chicanne *et al.* using a SNOM tip to illuminate the sample, the detection being done by blocking the portion of the transmission located below the critical angle [66]. Our results (Fig. 2.19 (a) and (b)) are similar to the near-field images presented in Fig. 2.20 for the two polarizations suggesting thus that for this type of arrangement and structures, a significant number of modes can be excited using our approach and a near field approach isn't required.

To quantify the amount of projected LDOS on the detected signal, we recorded the scattered intensity for an incident polarization oriented along the minor axis for two ana-

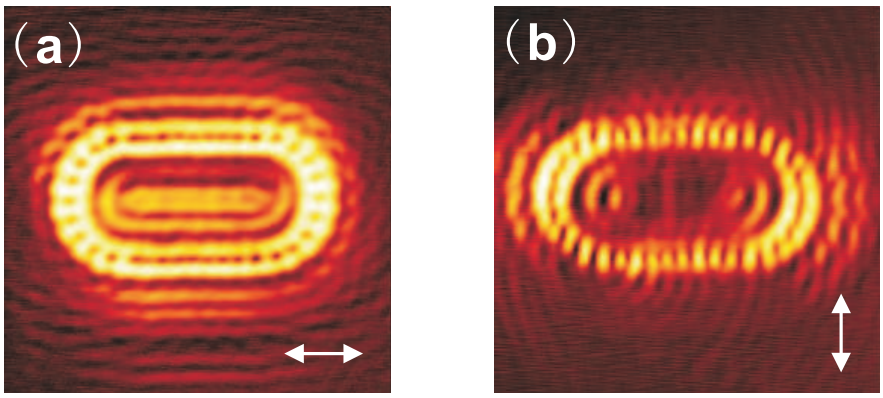

Fig 2.20: Near-field experimental SNOM images of a 4μm $\times 2\mu$m stadium with the two orientations (white arrows) of the source dipole. The size of gold nanoparticles are 100 nm $\times$ 100 nm $\times$ 50 nm. Image adapted from Ref. [66].

lyzer orientations. The main features of Fig. 2.19(f), *i.e.*, $\rho_y(\mathbf{r})$, are again well reproduced for a parallel analyzer, notably the positions and the shapes of the stadium's foci as shown in Fig. 2.21(a). Figure 2.21(b) shows the image obtained for an orthogonal analyzer. Despite a weaker signal, the shape of the modulations indicated that we have to account for a small portion of $\rho_x(\mathbf{r})$ in the detected signal. Compared with the relative scattered intensities maxima, the detected information is the linear superposition of approximately $0.95\rho_{\parallel}(\mathbf{r}) + 0.05\rho_{\perp}(\mathbf{r})$, where the labels $\parallel$ and $\perp$ stand for parallel with and perpendicular to the incident polarization, respectively. We neglected the out-of-plane $\rho_z(\mathbf{r})$ because of the relatively small longitudinal depolarization induced the 0.65 N.A. lens.

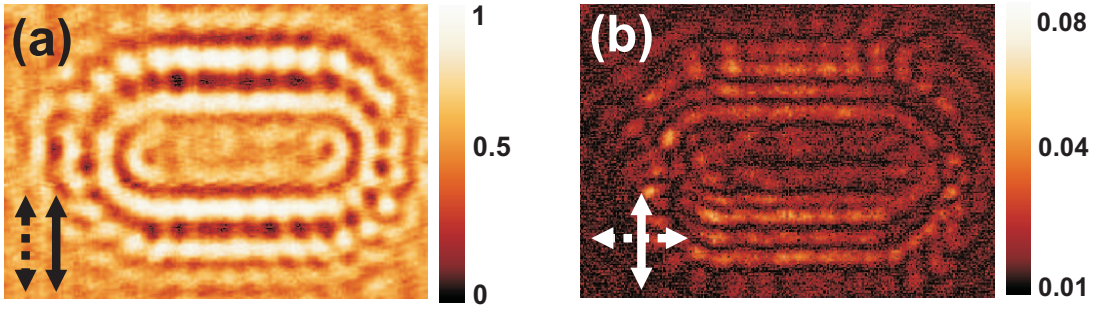

Fig 2.21: Experimental LDOS for an incident y polarization (thick arrows) in the presence of parallel (a) and perpendicular (b) analyzer orientations (dotted arrows).

We have also investigated a larger stadium of the diameter 5μm $\times$ 3μm and Fig. 2.22 (a) and (b) show the experimental images. Significant differences with the previous stadium size are visible, notably in the number and contrast of the inner fringe pattern. Since

the stadium consists of the same number of particles, increasing the overall dimensions implies a greater distance between particles, and therefore a reduced collective interaction. Figure 2.22 (c) and (d) represents the calculated projected LDOS along the polarization direction. Here too, the calculated pattern qualitatively agree with the experimental images.

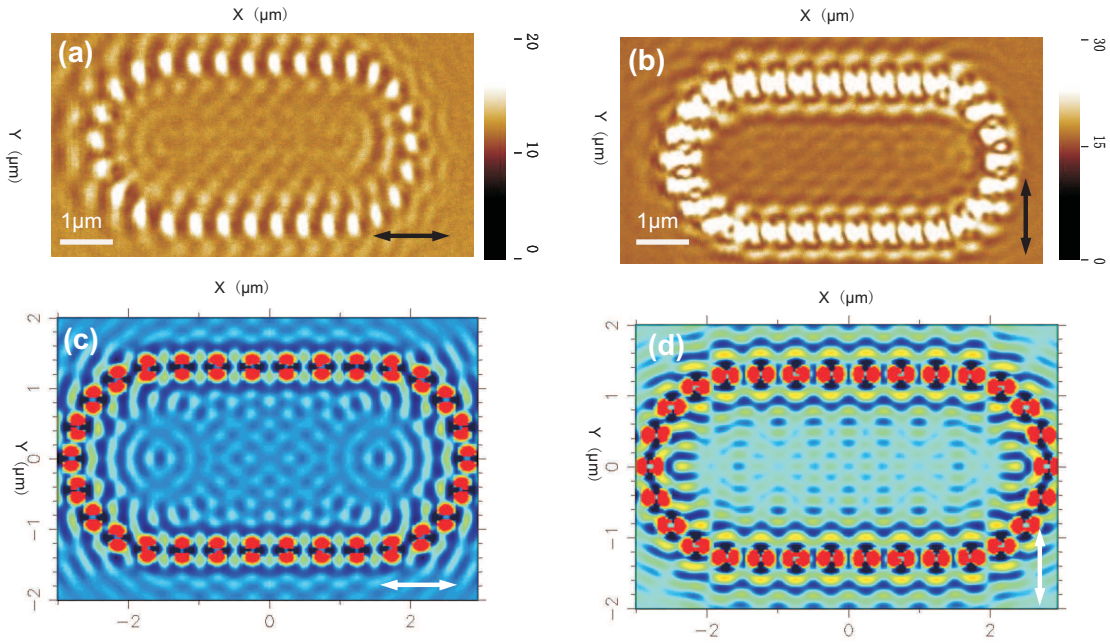

Fig 2.22: 5μm×3μm stadium. (a-b) Experimental images for two orthogonal excitation polarization as indicated by the arrows. (c-d) calculated LDOS $\Delta\rho_x^E(r)$ and $\Delta\rho_y^E(r)$ for a dipole placed at 100 nm above the surface for the corresponding dipolar orientations.

2.5 Conclusion

In electromagnetic theory, the density of optical states is directly related to the square modulus of the electric field associated with all the electromagnetic eigenmodes of a given structure and is therefore independent on the illumination mode. For a dipole in free space, the LDOS stays constant, but it changes in the presence of a surface or nanostructures. This variation reflects the intrinsic response of the surface or the nanostructures. The control of the LDOS with optical antennas is in its infancy and requires a profound understanding of antenna's characteristics before harnessing light-matter interactions. With this chapter, we have introduced and characterized a novel imaging technique capable to

qualitatively assess the local electromagnetic density of states. We have demonstrated that detecting the differential scattering cross sections of small particle gives valuable information about the underlying LDOS. The detected signal reflects the intrinsic scattering response of the photonic structures and renders the partial LDOS dominated by evanescent modes. We also demonstrated a theoretical understanding of the LDOS image formation and showed a qualitative agreement between experimental images and theoretical maps.

We conclude that the local density of electromagnetic states can be qualitatively imaged without introducing external dipole-like emitters providing that the more significant modes of the object can be excited by the scattered wave-vector spectrum. Although our approach remains diffraction-limited, we will use it in the following chapters to characterize the important parameters defining individual optical antennas.

Chapter 3

General characteristics of optical antennas

In the visible and infrared regimes, optical antennas, constituted of metal nanoparticles have distinct properties and functions, different from radio-frequency antennas. Optical antennas are generally characterized by their capabilities to strongly confined light and to enhance an optical response. Optical antennas are also a prime device to engineer radiation emitted by quantum systems. Investigating the characteristics of optical antennas are generally inferred from indirect measurements. The field enhancement factor for instance, is often derived from measurements involving the optical response to amplify: Raman scattering [118], fluorescence [18], or nonlinear photoluminescence [47, 119, 120]. However, an additional external molecular reporter introduces a perturbative influence on antenna characteristics [121] since the variation of the load medium modifies the plasmonic properties of the antennas and leads to a measurement characteristic of the antenna plus the reporter system, but not the antenna itself. Moreover, the characterization of optical antennas without probe molecules is usually restricted to their spectral properties, that is the position of the surface plasmon resonances.

Alù *et al.* took a somewhat different approach [122]. They defined antenna parameters such as gain and radiation efficiency to analyze plasmonic structures. Following Alù's analogy with the terminology used in antenna theory, we will describe in this chapter a new set of characteristics. We introduce and measure critical scattering parameters defining an optical antenna: operating wavelength and bandwidth, detuning and gain from an excitation wavelength, and radiation pattern. These parameters reflect the performance of antennas interacting with light. These parameters depend on the localized surface plasmon resonance which is strongly affected by the morphologies of the particles [123,

124, 125]. Therefore, controlling the essential characteristics defining an optical antenna by changing the design geometry provides a passive control over the optical device.

3.1 Fundamental parameters of an antenna: efficiency, gain and directivity

Efficiency, gain and directivity are standard parameters describing the characteristics of radio frequency antennas. According to antenna theory [126], the relative power radiated by an antenna, or the antenna radiation efficiency η_{rad} is defined as:

$$\eta_{rad} = P_{rad}/P_0 = P_{rad}/(P_{rad} + P_{loss}), \tag{3.1}$$

where P_0, P_{rad}, P_{loss} are the input power, radiated power and power dissipated into heat and other channels, respectively. By integrating the angular radiation intensity $p(\theta, \varphi)$, P_{rad} can be formulated as:

$$\int_0^{2\pi} \int_0^{\pi} p(\theta, \varphi) sin\theta \mathrm{d}\theta \mathrm{d}\varphi = P_{rad}, \tag{3.2}$$

where θ, φ denote the polar angle and the azimuthal angle, respectively. By reflecting the ability of an antenna to convert feed energy into a specific direction, the gain G is defined as :

$$G(\theta, \varphi) = \frac{p(\theta, \varphi)}{P_0/4\pi}. \tag{3.3}$$

The term $P_0/(4\pi)$ could be considered as the average distribution of the input power over the radiation sphere in steradian. The gain of an actual antenna is usually measured at the peak radiation intensity and exhibits the extent (ability) of the concentration of the power. However, it is not practical even difficult in the context of optical antenna to measure the input power in practice. Therefore we define the relative gain for optical antennas as a normalization of the maximum intensity from an antenna of interest over that of a reference antenna, which will be well discussed in the following section. A dipole antenna is usually used as a reference because the dipolar emission pattern is the simplest and is well characterized. In our work, we will therefore serve an antenna, essentially behaving as an optical dipole, as reference to evaluate the relative gain of more complex designs.

Another important parameter is so-called directivity which gives the antenna's ability to concentrate radiated power in a specific direction and can be written as:

$$D(\theta, \varphi) = \frac{p(\theta, \varphi)}{P_{rad}/4\pi}, \tag{3.4}$$

where the term $P_{rad}/4\pi$ represents the average radiation intensity over the whole solid angle. The definition of directivity is similar to that of gain G, but using the term P_{rad} instead of P_0. When the direction (θ, φ) is not specified, we often calculate the directivity at the direction of maximum intensity:

$$D_{max} = \frac{p_{max}(\theta, \varphi)}{P_{rad}/4\pi}. \tag{3.5}$$

It is also difficult for optical antennas to measure the term P_{rad} by integrating the differential radiated power over the whole solid angle. However, we introduce another related parameter – the radiation pattern to investigate the directivity. The radiation pattern describes the intensity distribution in a specific direction, which is also our measure of interest. Because the vectorial character of the field, the radiation pattern can be separated into two orthogonal polarization components by using a collinear or crossed analyzer before the detection.

By combining Eq. 3.1, Eq. 3.3 and Eq. 3.4, we can get the relationship between gain G and directivity D:

$$G = \frac{4\pi p(\theta, \varphi)}{P_0} = \eta_{rad} D \tag{3.6}$$

From Eq. 3.6, gain and directivity differ only by the efficiency, but directivity is easily estimated from scattered patterns. Therefore, we analyze in the following section the radiation patterns in the azimuthal plane in order to estimate qualitatively the directivity of optical nano-antennas.

3.2 Sample fabrication

Antennas consisting of individual gold nano-particles and dimers were fabricated by following the fabrication steps described in Chapter 2. The layout of sample is schematically shown in Fig. 3.1 (a). The fabricated array is designed to represent a parametric space where the particle diameter and inter-particle distance is systematically changed: all the antennas are nominally different.

The individual nanoparticles have a varying diameter ranging from 66 to 90 nm along y-direction. For the dimer antennas, the gap distance between element particles (edge-to-edge) was systematically decreased from 140 nm down to contact with a minimum separation distance of 10 ± 2nm along x-direction. Figure 3.1 (b) and (c) show electron micrographs of a part of antennas array together with close up images of selected single and pairs. The first column on the left corresponds to single gold nanoparticles, whereas the last two columns on the right of the array are bridged particles. The spacing among dimers was kept constant to 3μm to avoid any significant array-induced optical coupling between dimers.

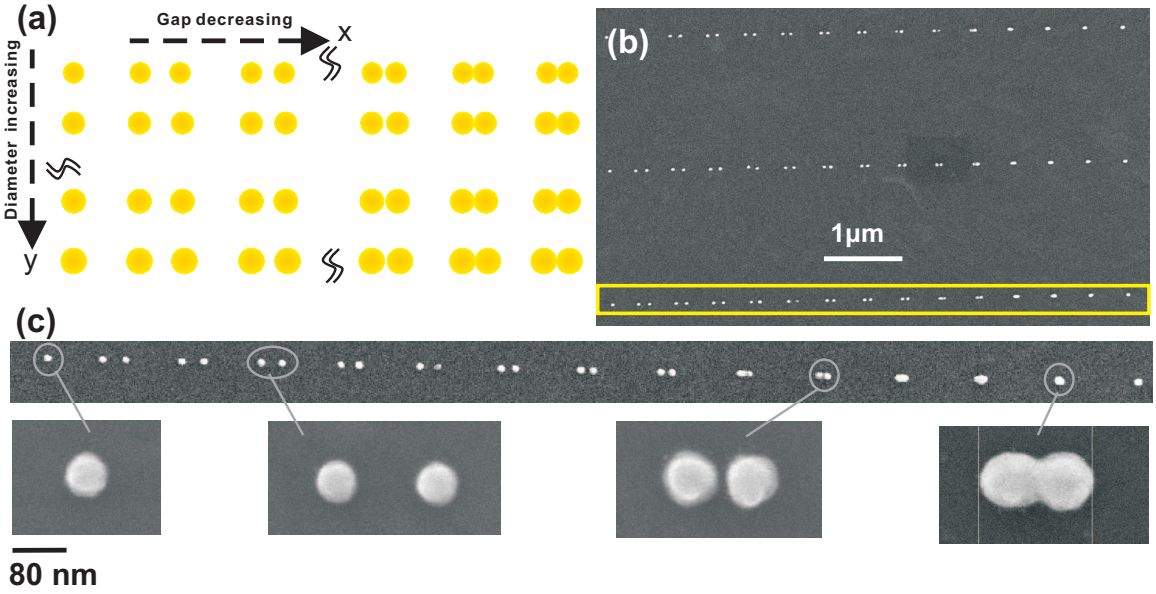

Fig 3.1: (a) Schematic view of antennas array (20 rows × 15 columns). Spacing among single dimers is 3μm. The first column on the left are single-particle antennas, and the last two columns are bridged particles. Interparticle gap within dimers decreases from 140 nm down to contact with a minimum separation distance of 10 ± 2nm along x-direction. Particle diameters increase from 66 nm at the top row up to 90 nm at the bottom one. Scanning electron microscope images: (b) three adjacent rows within the antennas array and (c) the selected row boxed in (a). The lower panel shows close up images of the single particle and several typical dimer antennas.

3.3 Confocal scanning imaging

The experimental setup used in this chapter adopts the concept developed in Chapter 2 and is based on the detection of the differential scattering cross-section of our optical antennas. As a reminder, our detection scheme retains only the frustrated evanescent

components of the scattering spectrum. We note that this detection scheme is different to other confocal approaches where the contrast originates from propagating components [125]. In this reference, the experiment was performed by scanning confocal dark-field microscopy. The illumination is restricted to a grazing-incidence ring of ~ 0.95 N.A. which highly limits the excitation modes. Moreover, since the majority of the dipole emission is concentrated around the critical angle, the higher modes of the scattering spectrum off the antennas could not be detected by using a 0.9 N. A. objective which results in a lower resolution and a significant loss of information. However, this kind of imaging affords a manner to understand the performance of optical antennas, which is a complementary means to our approach.

3.3.1 Excitation at λ=633nm

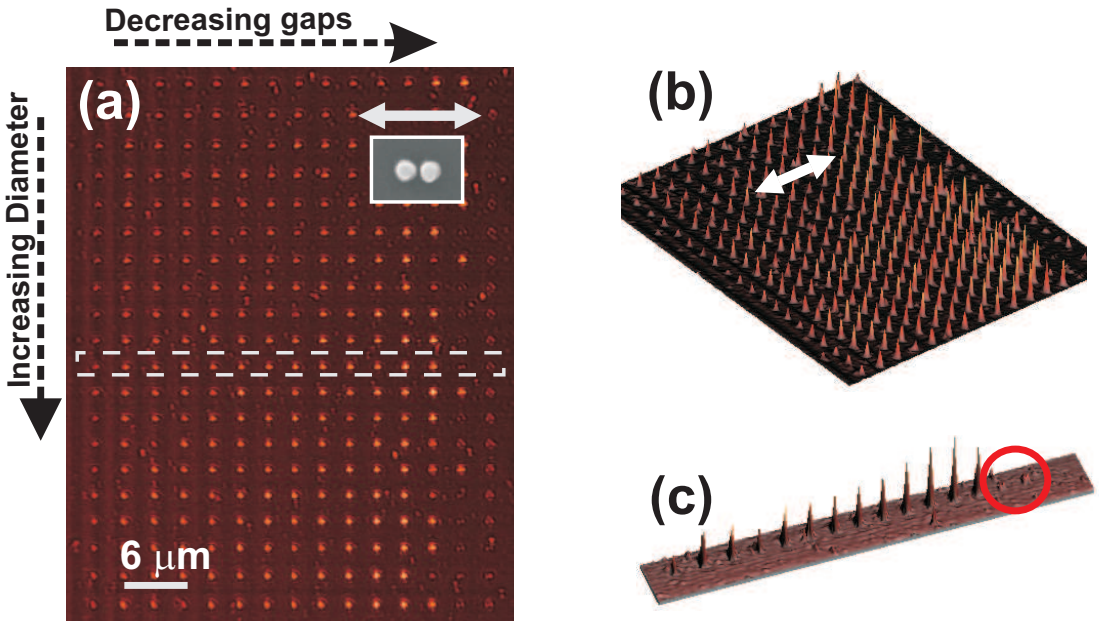

Fig 3.2: (a) Scattered intensities at $\lambda = 633$ nm from individual antennas constituted of gold nanoparticle dimers for a polarization(white arrow) parallel to the dimer axis. The first column on the left are single-particle antennas, and the two last columns on the right are bridged particles. Top line displays particles with diameter of 66 nm increasing up to 90 nm for the bottom line. (b) Three-dimensional rendering of the intensity distribution of (a). (c) is three-dimensional rendering of the line of antennas extracted from (a) (dotted box).

Figure 3.2 shows a two-dimensional scan of the differential scattering intensity from the array of antennas at an excitation wavelength $\lambda_{exc} = 633$ nm. The polarization

of the incident light was oriented along the dimer axis (line connecting the particle's centers) as indicated by the white arrows. The magnitude of the scattered intensity is not constant within the array. In Fig. 3.2(b), the brightest antennas appear for larger particle diameters located on the bottom half of the array. This is consistent with Eq. 2.11 showing an increase of the scattering efficiency Q_{scat} with the diameter of the particle. The single particles located at the first column on the left show a relative weak intensity with respect to the same line of dimer antennas. Figure 3.2(c) shows that the scattered intensity increases by reducing the gap distance between dimers. At first sight, one may reasonably assume the point spread function of the microscope to be responsible for this observation since the size of the pair for the largest gaps is comparable to the detection response of our apparatus. It is probably true for the largest gaps where the particles have a limited mutual interaction. This is confirmed by the images of Figure 3.3 where two dimers, one with a small gap separation (26 nm) and an another with a large separation (126 nm) were imaged. The images display similar patterns for the two dimers with a slight elongation along the dimer axis for the largest gap. There are no significant differences in the magnitude of the scattered intensity between the two antennas.

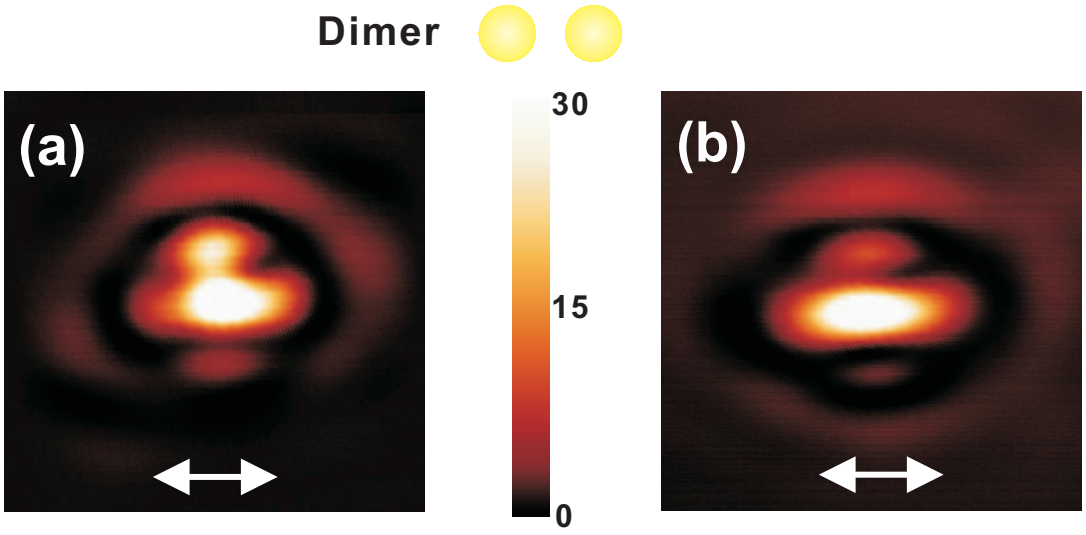

Fig 3.3: Scattered intensities at λ=633nm from single dimers with a gap distance of (a) 26nm and (b) 126nm. Individual particle diameter is of 80nm. The arrows represent the polarization. The image size is of 2μm. The top panel indicates the orientation of the dimers.

The argument about the PSF may not be the only explanation since an abrupt falloff of the scattered intensity is observed for bridged pairs (circle in Fig. 3.2(c)). Furthermore, when the polarization is orientated perpendicular to the dimer axis, the contacted dimers

recover some scattering strength as shown in Fig. 3.4(a). For this polarization, the largest particles are also more efficient scatterers (Fig. 3.4 (b)). However, to the difference with the polarization aligned along the dimer axis, the magnitude of the scattered intensity is almost constant regardless of the gap distance (Fig. 3.4(c)).

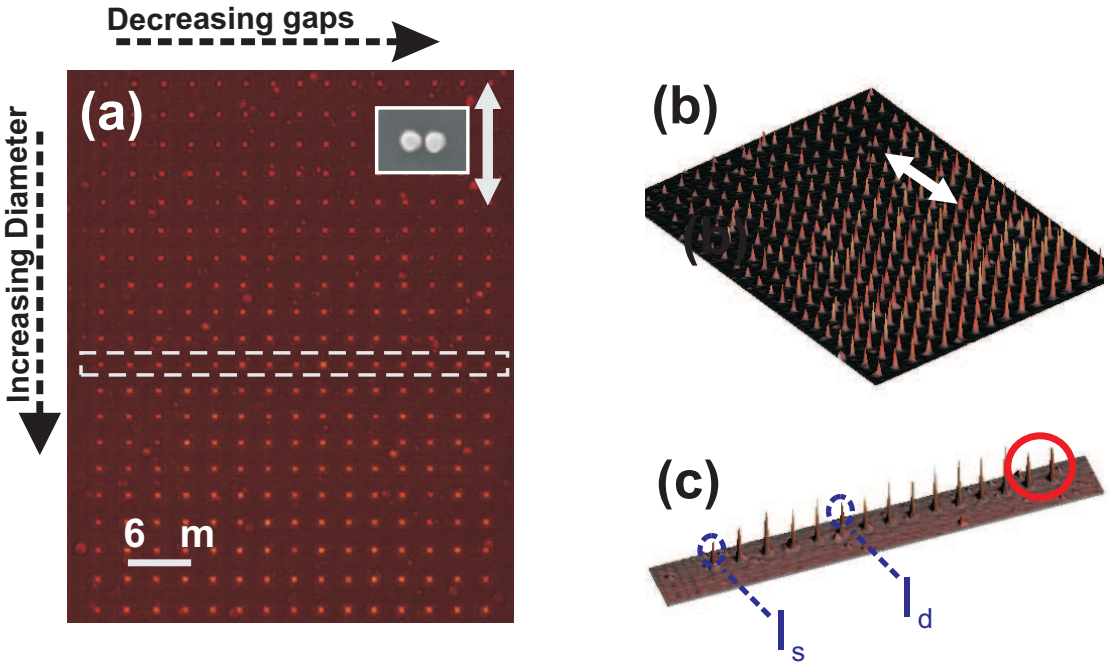

Fig 3.4: (a) Scattered intensities at λ=633nm from single antennas constituted of gold nanoparticle dimers for a polarization (white arrow) perpendicular to the dimer axis. The first column on the left are single-particle antennas, and the two last columns on the right are bridged particles. Top line displays particles with diameter of 66nm increasing up to 90nm for the bottom line. ((b) Three-dimensional rendering of the intensity distribution of (a). (c) is three-dimensional rendering of a line of antennas extracted from (a)(dotted box). I_s and I_d represent the intensities of the reference single particle and of a dimer, respectively.

3.3.2 Excitation at λ=780nm

To get further information of the influence of the excitation frequency on the scattering intensity, the antennas array was then excited at $\lambda_{exc} = 780$ nm and for the two crossed polarizations. The scattered intensities of the antennas at this excitation wavelength behave quite differently as shown in Fig. 3.5. The intensity increases with the reduction of the gap distance and even reaches the maximum for the bridged dimers (the column indicated by the yellow arrow in Fig. 3.5(a)). However, the isolated particles (the column indicated by the blue arrow) are almost within the background noise of our system. For

the perpendicular polarization, Fig. 3.5 (b) demonstrates a negligible intensity variation in the antennas array with the gap distance.

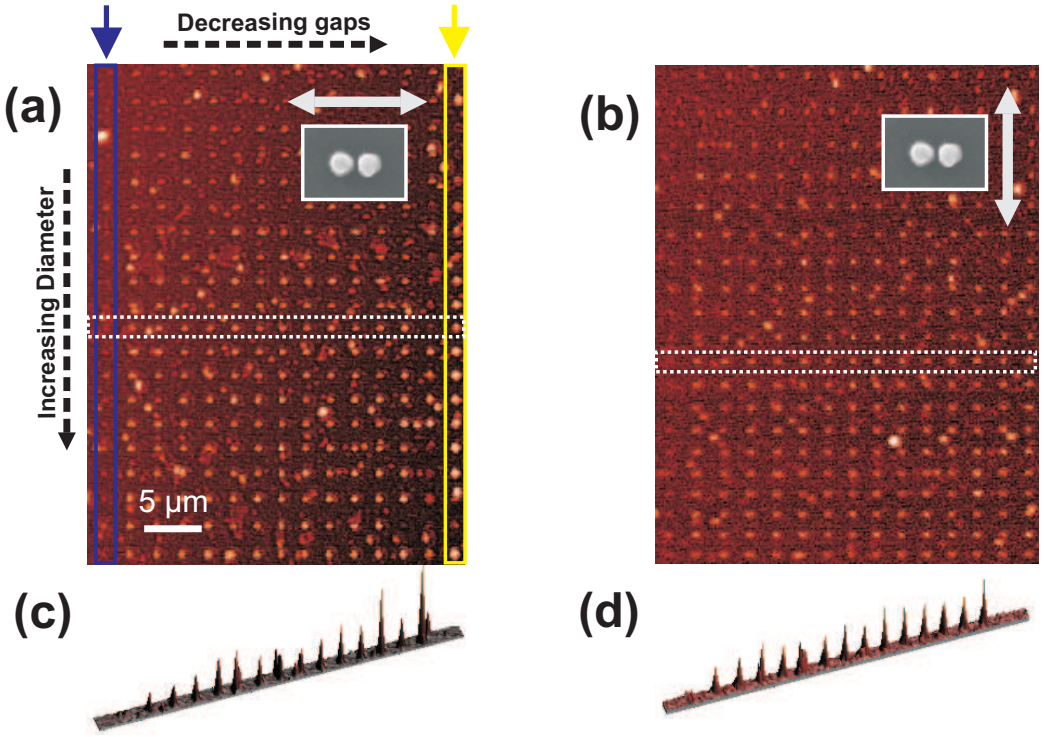

Fig 3.5: (a) and (b): Scattered intensities at $\lambda = 780$ nm from antennas array consisting of single and dimer gold nanoparticle(s) for a polarization (white arrows) parallel to the dimer axis and perpendicular to it, respectively. The first column on the left is single-particle antenna, and the two last columns on the right are bridged particles. The scattering magnitude of the single particles antennas is weak (indicated by a blue arrow) in (a), whereas the bridged pairs experience high scattering cross section (shown by a yellow arrow in (a)). (c) and (d) are three-dimensional renderings of a line of antennas extracted from (a) and (b) (dotted box), respectively.

The images of Fig. 3.6 show the evolution of intensity distribution for increasing gap separations (contact, 15 nm and 131 nm) and an on-axis polarization. It is clear that the magnitude of the scattered intensity increases with smaller gaps.

At that point of the discussion it is interesting to propose a hypothesis to explain the results exposed in these few pages. To summarize in few words the results, the intensity scattered off the antennas depends on a series of parameters. The morphology of the antenna (particle size, gap distance), the orientation of the polarization and the operating wavelength are all playing a role in the magnitude of the measured signal. We also know that these series of parameters are strongly affecting the position of the surface plasmon resonances in these systems. It is therefore tempting to hypothesize that plasmon

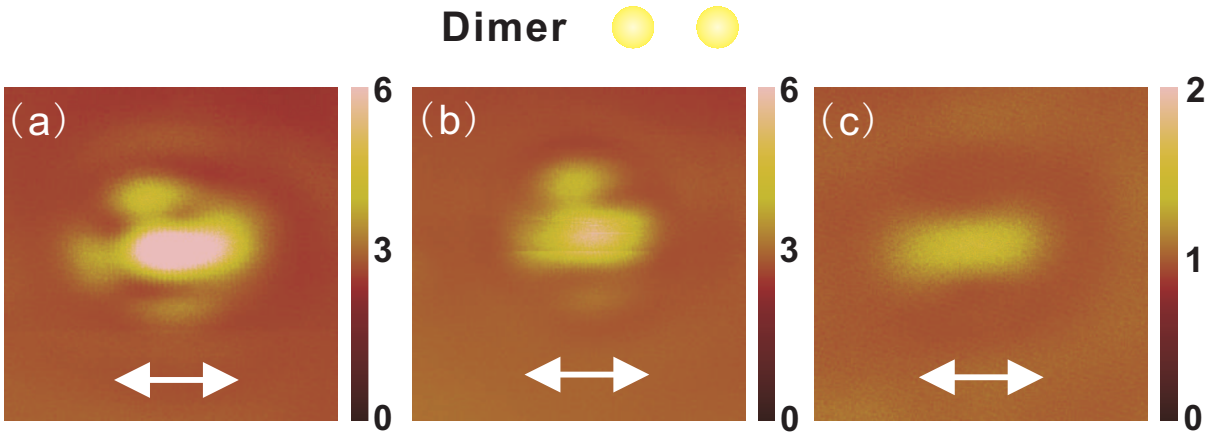

Fig 3.6: Scattered intensities at λ =780 nm from single dimers with a gap of (a) contact, (b) 15 nm and (c) 131 nm. Individual particle diameter is $\sim$ 80 nm. The arrow represents the polarization. The image size is of 2μm. The top panned indicates the orientation of the dimer.

resonances are inherently linked to the change of scattered intensity through Eq. 2.11: an increased scattering efficiency taking place at the plasmon resonance. In turns, when the antenna is excited close to its plasmon resonance, the scattering signal will be maximal. To verify our hypothesis, we have measured the spectral response of our antennas by using dark-field spectroscopy.

3.4 Spectral characteristics of individual and dimer particles

3.4.1 Dark-field imaging

The antenna array was mounted on a conventional dark-field microscope equipped with a spectrometer to measure spectral properties of antennas and deduce the position of their surface plasmon resonances. The illumination geometry consists of a cone of grazing-incidence wave-vectors defined by a $0.85-0.95$ N.A. illumination ring. Scattered photons are collected by a $40\times$, 0.60 N.A. long-working-distance objective and detected, after an entrance slit, by a high-sensitivity charge-coupled device (CCD). This apparatus can be employed to record images or spectra by changing the orientation of the optical grating. We note that the dark-field images reflect the scattered radiation originating only from the propagative components of antennas. The evanescent components are not collected by the objective's N.A. We assume therefore that the spectral content of the signal scattered

off the antennas is independent of the emission angle. Figure 3.7(a) shows a dark-field false-color CCD image of a part of the antennas array by using a white light source. Each bright dot represents an individual antenna (single or dimer). The orientation of the image is the same as of Fig. 3.2. The higher intensities tend to be found for the dimers with larger particles and smaller gaps (indicated by arrows in Fig. 3.7(a)) although this cannot be directly compared with Fig. 3.2 since here the signal is integrated over all the excitation spectrum. Furthermore, since the numerical apertures used for the detection in both apparatus are different, the magnitude at a given wavelength also cannot be compared because the scattered intensity strongly depends on the radiation angle.

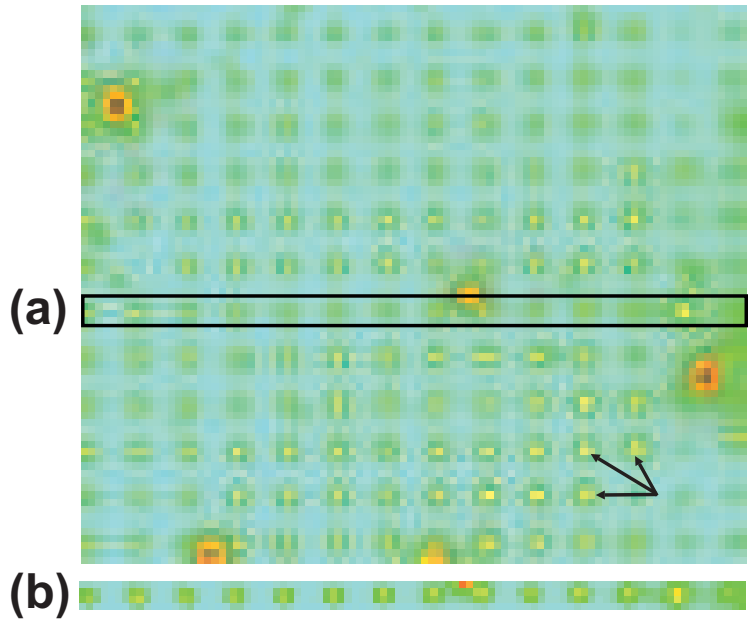

Fig 3.7: False colored CCD images of a part of antennas array recorded by dark-field microscopy with a slit of (a) 2500μm and (b) 250μm. (b) is the row enclosed in (a). The last two columns situated on the right are bridged particles.

In order to measure the scattering spectrum of an individual antenna we have first selected a line of antenna by closing the entrance slit as illustrated in Fig. 3.7(b). We then integrate the received signal only on the pixels corresponding to the location of an antenna.

A typical spectrum of a single particle antenna of diameter $\sim$ 70nm is shown in Fig. 3.8 with a resonance peak at $\sim$ 630nm and its full width at half maximum (FWHM) of 82 nm.

Figure 3.9 shows characteristic spectra originating from an individual dimer with an

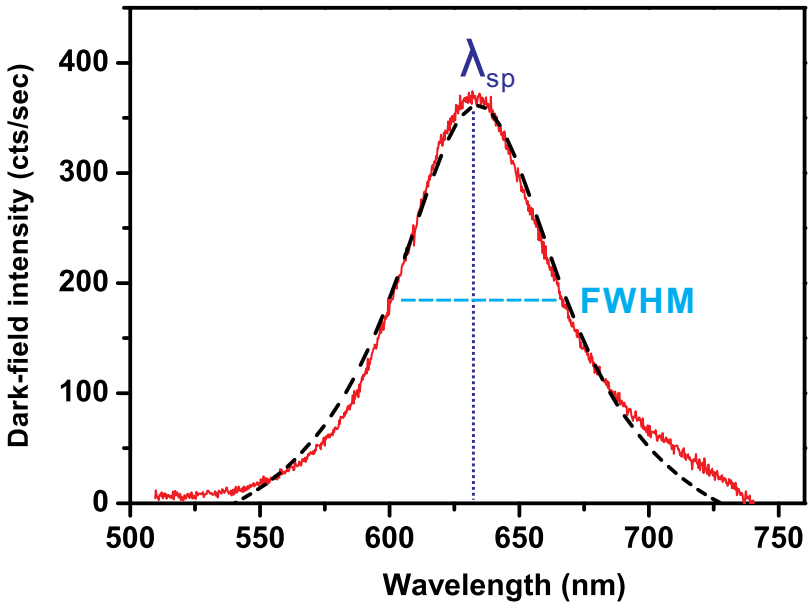

Fig 3.8: Spectrum of a single nanoparticle (diameter $\sim$ 70nm), fitted with a Lorentzian function (dashed black curve). The spectral maximum is denoted as λ_{sp} and its full width at half maximum (FWHM).

approximate 10nm gap and 70nm diameter for an unpolarized and two respective polarized illuminations. A spectral maximum appears at $\sim$ 630nm for the polarization perpendicular to the dimer axis, and a $\sim$ 730nm resonance peak occurs for the parallel polarization. The unpolarized spectrum results from a combination of these two polarization spectra.

λ_{sp} of the two crossed polarization for particle with a diameter of 80 nm is measured and plotted as a function of interparticle gap distance in Fig. 3.10. The vertical bars indicate the FWHM of resonance maxima. The splitting of λ_{sp} starts for particle separation below 30 nm and a redshift of λ_{sp} is observed for a polarization oriented along the main axis of the antennas in accordance with the literature [124, 127, 128, 129, 130, 131]. We note that averaged measurements on large arrays of coupled nanoparticles revealed a small blueshift of the resonance for an electric field perpendicular to the long dimer axis [124, 131, 132]. We do not see such a shift in our single-dimer measurements. Instead, we measured a systematic redshift of the resonances (Fig. 3.10). We attribute this difference to the unique fingerprints of individual dimers. These individual different responses can also be observed from dimers with large gaps ($>$ 50nm) whereby the position of the maxima exhibits spectral oscillations despite nominally comparable particles

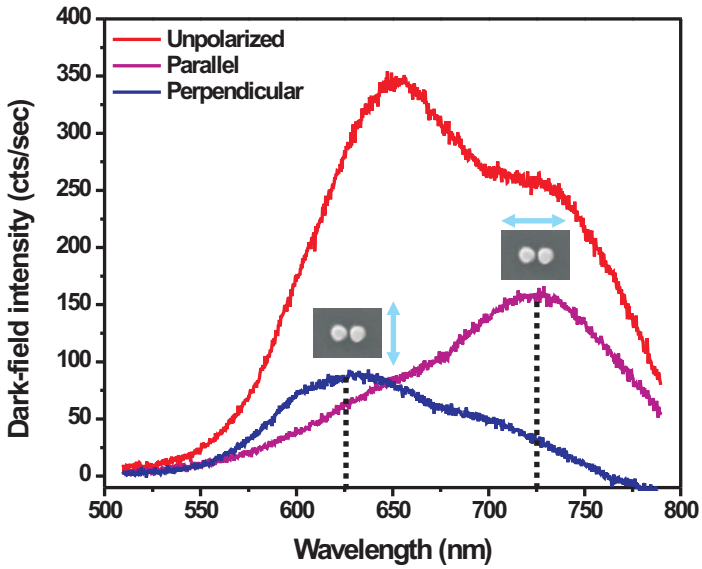

Fig 3.9: Characteristic spectra for an strongly coupled dimer (gap $\sim$ 10nm). The unpolarized spectrum (black) features two polarization-sensitive resonances identified by two polarized excitations (blue and violet).

(Fig. 3.10). The resonance spectra of the coupled-dimer antennas are considerably broadened compared to those of single nanoparticles owing to a strong radiative damping of the coupled antenna modes [125].

3.5 Detuning and relative gain

The scattering field becomes enhanced as metal nanoparticles are excited from off-resonance to in-resonance state. This implies a dependence of the scattered intensity on the excitation wavelength. The scattering intensities excited at $\lambda = 633$ nm and $\lambda = 780$ nm as well as the spectral analysis were accomplished in the previous two sections. To correlate the variations in the scattered intensity at the excitation laser frequency with the spectral signature of the antenna, we define two parameters. The amount of detuning $|\delta\lambda|$ is obtained by measuring the difference between the laser wavelength λ_{exc} and the resonance maxima:

$$|\delta\lambda| = |\lambda_{exc} - \lambda_{sp}|. \tag{3.7}$$

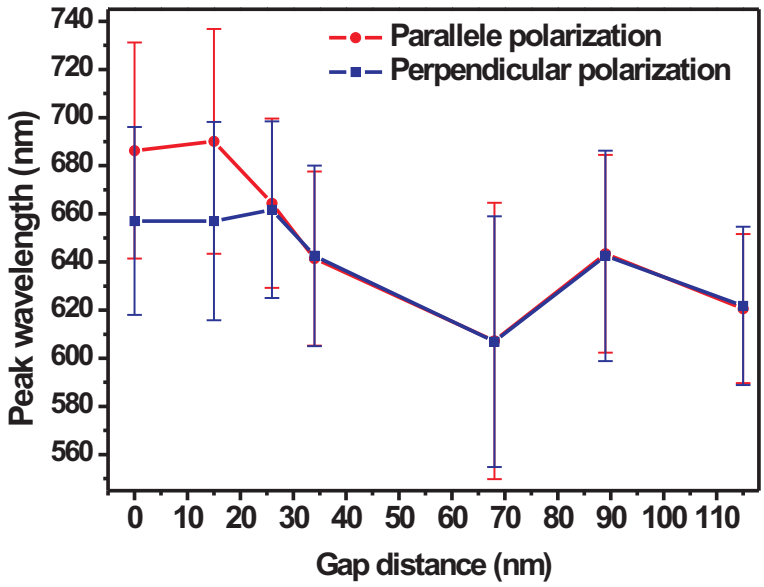

Fig 3.10: Peak wavelength (λ_{sp}) as a function of gap distance. For small gaps (here, < 30nm), a redshift and a hybridization of the resonances are observed. The vertical bars indicate the FWHM of the resonances. The particle diameter is 80nm.

Furthermore, the relative gain G is introduced to describe the ability of an antenna to concentrate light propagation into a certain direction. Gain is usually a ratio of the antenna's radiation intensity (power) normalized to that of a reference radiator, i.e., a dipole [126]. For small particles compared to the wavelength of light, an isolated spherical nanoparticle behaves essentially like a dipole. We therefore define G by measuring the magnitude of the scattered intensities I_d (Fig. 3.4) originating from dimers and normalizing it to the one issued from single-particle antennas I_s of the same diameter:

$$G = I_d/I_s. \tag{3.8}$$

This definition assumes that the scattered angular distribution and the collection efficiency of our experimental setup are constant regardless of the particle arrangement. The validity of this assumption will be asserted in the following subsection.

Figure 3.11 shows the evolution of the parameters $|\delta\lambda|$ and G by reducing the gap between the dimer for an excitation wavelength at 633nm polarized along the dimer axis. For large gaps (> 50nm), detuning from the excitation laser $|\delta\lambda|_{633nm}$ is less than 25nm, indicating that the antennas are close to the resonance with the laser excitation. This is

confirmed by the trend of the G factor, which varies around 2.5. For a group of identical particles characterized by a weak mutual optical interaction, G should scale linearly with the number of particles presented in the detection volume if the excitation is homogeneous. However, the measured value is slightly larger than the expected value of G=2. We think this small difference originates from the polarization-sensitive inhomogeneous field distribution inside the excitation and detection volumes [34].

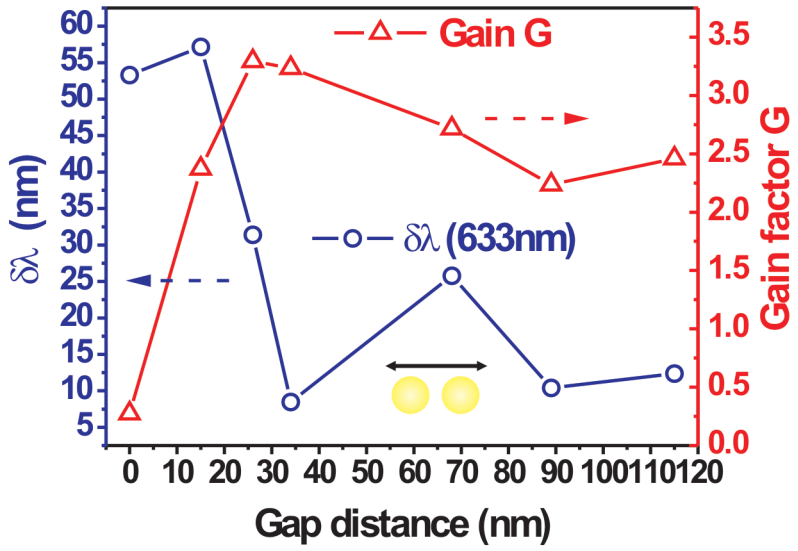

Fig 3.11: Detuning factor $|\delta\lambda|_{633nm}$ (blue) and gain factor G (red) for the parallel polarization (arrow) with respect to the dimer axis. Particle diameter: 80 nm.

For small gaps, a strong electromagnetic coupling occurs between the particles constituting the antenna and $|\delta\lambda|_{633nm}$ increases rapidly even reaches up to 55nm for a 15-nm gap. Under this condition, the antenna is significantly detuned from the excitation wavelength. G dramatically drops from a maximum of 3.3 for a 25-nm gap to a value of 0.3 for the bridged dimer, confirming that the optical antenna is effectively detuned from its optimum excitation frequency.

Figure 3.12 shows the trend of G and $|\delta\lambda|_{633nm}$ as a function of gap for a polarization oriented perpendicular to the dimer. $|\delta\lambda|_{633nm}$ oscillates around 15 nm and stays within the full width at half maximum of the surface plasmon resonances (see Fig. 3.10). The gain forms two platforms of almost constant G values (G=2.3 and 1.6 with variations $\sim$ 10 %) for gaps below 50 nm and gaps above 50 nm, respectively. Since $|\delta\lambda|_{633nm}$ stays near resonance with the excitation line and G is close to its expected value of 2, we also

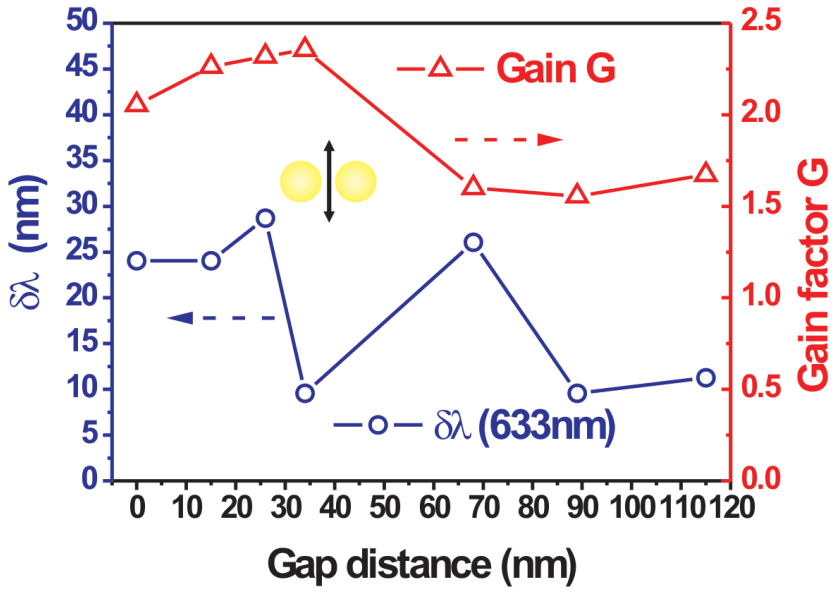

Fig 3.12: Detuning factor $|\delta\lambda|_{633nm}$ (blue) and gain factor G (red) for the perpendicular polarization (arrow) with respect to the dimer axis. Particle diameter: 80 nm.

attribute these two platforms to the inhomogeneity of the focal field distribution: it's only when the particles are close enough to each other that the excitation intensity can therefore be assumed to be spatially constant.

We note that the experimental magnitude of G does not reach very large enhancement values as predicted from strongly coupled nanoparticle pairs and small gaps [55, 133]. This relatively low gain has also been observed in Ref. [134]. It is worth emphasizing that the enhancement factors calculated in the literature are usually normalized to the applied field, whereas in the present work we compare G to a reference dipolar antenna. Furthermore, the fabricated particles are not perfect spheres and a non-negligible loss should be taken into account in the particles. We note that $|\delta\lambda|_{633nm}$, and to some extent G, show some oscillatory behavior with increasing gap distance. This particularity is observed regardless of the particle size within the fabricated array and polarization orientation. We did not see in our measurement a systematic correlation between the positions of the oscillatory peaks and the interparticle distance. We therefore believe that the observed oscillations are resulting from variations in the antenna morphology inherent to the fabrication process.

Only one instance in the study of the array depicted in Fig. 3.2 shows that G significantly increases. Figure 3.13 shows experimental values of G and $|\delta\lambda|_{633nm}$ for the

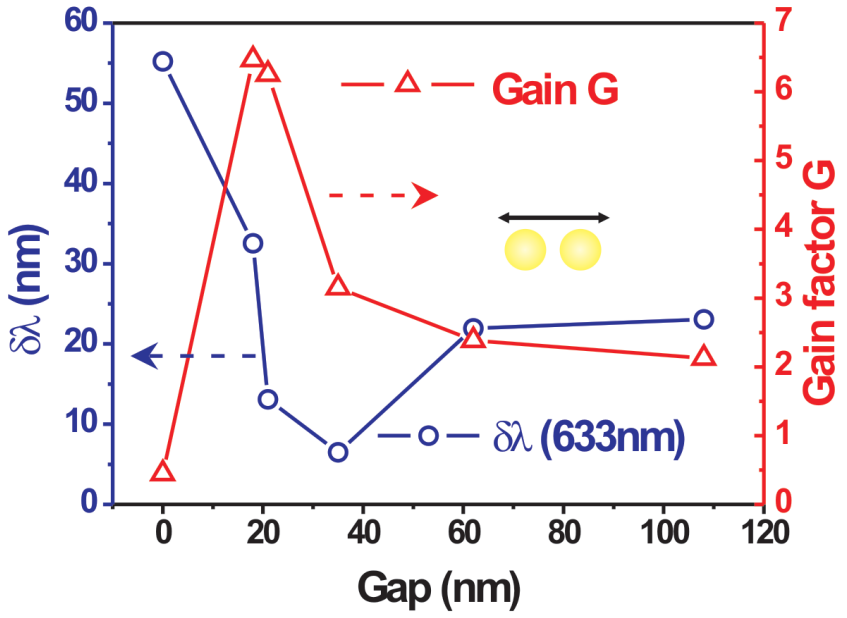

Fig 3.13: Detuning factor $|\delta\lambda|_{633nm}$ (blue) and gain factor G (red) for the parallel polarization (arrow) with respect to the dimer axis, respectively. Particle diameter: 66 nm.

top line of the array (particle diameter is 66 nm) and a polarization oriented along the dimer axis. For large gaps, typical spectral variation in $|\delta\lambda|_{633nm}$ is also observed and similar to that in Fig. 3.11. The gain factor is constant for the two largest gaps ($G \sim 2$) and displays a small increase for the 37-nm-gap dimer consistent with the low value of $|\delta\lambda|_{633nm}$. However, for smaller gaps, G keeps increasing to reach a value of 6.3 for the 18-nm-gap dimer, although the antennas are slightly detuned according to the value of $|\delta\lambda|_{633nm}$. G undergoes then an abrupt falloff for the bridged pair. Despite the antennas being detuned with respect to the laser line, the optical coupling and field amplification characterizing these particular antennas were sufficient to not only compensate G for the detuning of the antenna but also enhance it by a sixfold factor. The measured gain for this coupled antenna was not reproduced inside the fabricated array. It is worth pointing out the difficulty to design electromagnetic hot spots by such fabrication technique with a resolution $\sim$ 40 nm. Although the particle dimensions and gap distance are designed to be identical, in reality, there are always some variations in the exact size and shape of each particle and, in particular, in the separation between particles.

The contacted dimers feature a high detuning value and a very low gain at the excitation of $\lambda = 633$ nm for the parallel polarization (Fig. 3.13). It is therefore expected that

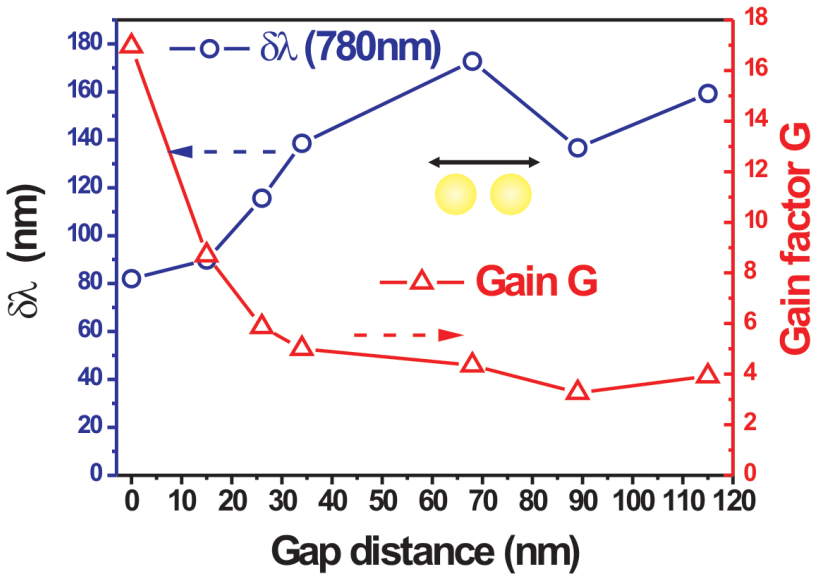

Fig 3.14: Detuning factor $|\delta\lambda|_{780nm}$ (blue) and gain factor G (red) for the parallel polarization (arrow) with respect to the dimer axis, respectively. Particle diameter: 80 nm.

by reducing the detuning the gain will be restored. To account for this phenomenon and confirm our approach to correlate the gain G and the detuning, we have performed our analysis with the excitation wavelength of $\lambda = 780$nm. Figure 3.14 displays the evolution of G and $|\delta\lambda|_{780nm}$ for the same set of antennas and for a polarization parallel to the dimer featured in Fig. 3.11. For decreasing gaps, $|\delta\lambda|_{780nm}$ also decreases as a result of the red shift of the resonance, and as hypothesized, strongly coupled dimers exhibit a significant recovering of G. In particular, the gain reaches the maximum for the contacted pair. To the difference with an illumination at 633 nm, antennas characterized by small gaps are better tuned toward a 780-nm-excitation line. It should be noted that the relatively high values of G (up to ~ 17) is also attributed to the weak intensity I_s scattered by the referenced single particle which is off resonance at 780 nm.

Figure 3.15 reports the case for a perpendicular polarization. $|\delta\lambda|_{780nm}$ indicates that the antenna is significantly detuned for this polarization regardless of the gap size. Accordingly, the antenna gains have low values compared to the orthogonal polarization. Nevertheless, a slow decrease in $|\delta\lambda|_{780nm}$ for small gaps is observed concomitant to a two-fold increase in G.

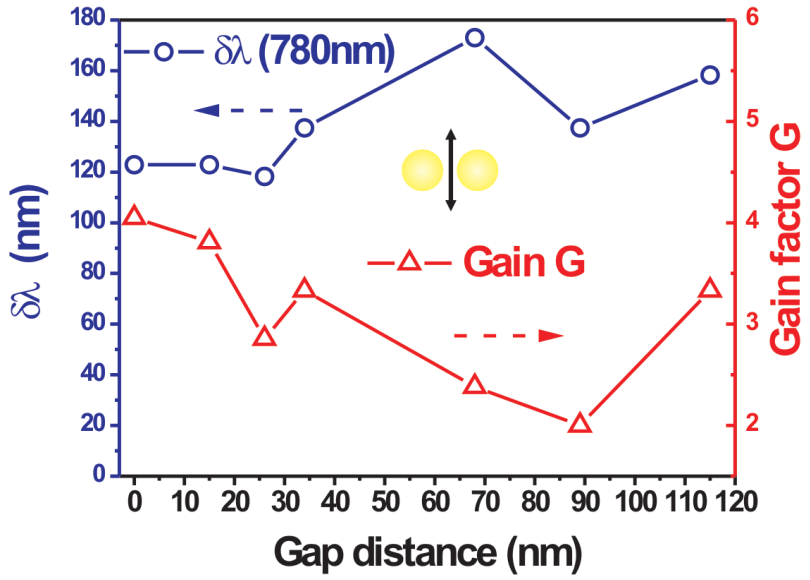

Fig 3.15: Detuning factor $|\delta\lambda|_{780nm}$ (blue)and gain factor G (red) for the perpendicular polarization (arrow) with respect to the dimer axis, respectively. Particle diameter: 80 nm.

3.6 Radiation patterns

In antenna theory, directivity and radiation patterns are key parameters to describe the ability of an antenna to interact electromagnetic wave (for details see subsection 3.1). For radio-frequency antennas, radiation patterns are generally measured in a homogenous dielectric medium (e.g. air). However, for optical antennas, they are traditionally deposited on a substrate like glass. The presence of an interface needs to be taken into account when dealing with the angular distribution of the scattered power. We have seen in the second chapter, and notably with Fig. 2.13, that the substrate converts part of the evanescent components of the scattered spectrum of a dipole [84] into propagating modes inside the substrate. The substrate modifies therefore considerably the radiation pattern and thus the directivity of the dipole.

To retrieve the scattering diagrams of our optical antennas we used the conoscopic apparatus introduced in Fig. 2.11. The experimental procedure consisted at mapping first the in-plane intensity distribution in order to isolate a desired antenna. Conoscopic imaging was then employed to record scattering pattern radiated in the substrate. The precise positioning of the antenna with respect to the excitation and detection foci was finely adjusted by the piezo-actuator. We remind the readership that our detection of the

radiation pattern is a partial determination since our detection path uses a beam stop to angularly filter the contribution of illumination.

3.6.1 Single-particle radiation patterns

Figure 3.16 displays experimental and theoretical scattered diagrams for a single colloidal 80-nm gold nanoparticle illuminated at $\lambda_{exc} = 633$ nm. Note that for this experiment, we used colloidal gold nanoparticle as opposed to e-beam fabricated antennas. Our motivation was to avoid any irregular shape, a fairly standard outcome in the fabrication process, to set a reference radiation pattern for the following. Figure 3.16(a) represents the intensity distribution pattern in the Fourier plane of the microscope for a polarization indicated by the thick arrow. A 150μm pinhole was inserted to spatially filter off-axis scattering. By removing the part of light emitted below θ_c in our measurement, the far field radiation pattern displays a typical two-lobe pattern with the lobes oriented along the polarization. Two lobes are concentrated around θ_c. These lobes are important characteristics of a dipole and their contrast depends sensitively on dipole orientation [84]. This scattered pattern is in very good agreement with our numerical calculation of a dipole emission shown in Fig. 3.16(e). The numerical calculation method used is the one described by Lieb and co-workers in Ref. [113]. Figures 3.16(b) displays the scattered diagram of the same particle analyzed through a parallel polarizer (broken arrow). Although The diagram retains the two-lobe pattern as seen in Fig. 3.16(a), there is a reduction in the intensity of the lobes. This is also obtained for a collinear arrangement of the polarizer and the analyzer regardless the original orientation of the polarizer (Fig. 3.16 (d)). Interestingly, in the presence of the cross polarizer (broken arrow) as shown in Fig. 3.16 (c), the scattered diagram changes dramatically and presents a four-lobe pattern. To account for the variation of the lobes, let us turn our attention to the polarization of the field scattered by the dipole at the surface shown in Fig. 3.17. The two-lobe pattern in Fig. 3.16 (b) corresponds to the zone labeled *a* in Fig. 3.17 where the field lines direction is parallel to the dipole orientation. Differently, the field lines in the zone *b* present two orthogonal components, which are the origin of the four-lobe pattern of Fig. 3.16 (b) and (c). Figures 3.16(f) and 3.16(h) are numerical simulations of the dipole emissions corresponding to the experimental polarizer and analyzer orientations. By comparing the experimental images and the calculations, a good agreement could be found between them, which indicate that the mainly scattered modes can be collected and detected by our apparatus. Moreover, a significant portion of the intensity is located

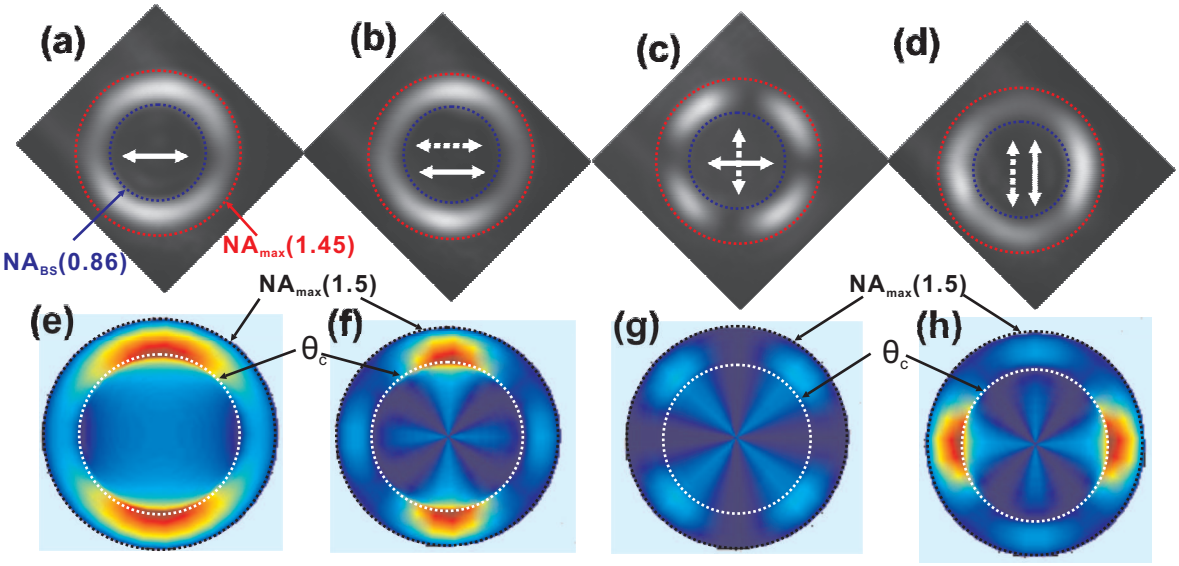

Fig 3.16: (a) to (d) Angular distribution patterns scattered from a single colloidal gold nanoparticle (80 nm diameter). The white thick arrows represent the incident polarizations and the broken arrows indicate the analyzer orientations. The scattered intensity is concentrated at the critical angle. (e) to (h) are the corresponding calculated intensity distributions. Note that the integration of the simulations runs over the complete numerical aperture. The center of experimental images is blocked by a beam stop with a N. A. of 0.86 (blue dashed circles). The N. A. maximum value is 1.45 for the experimental images (red dashed circles), but 1.5 for the calculations. The critical angle θ_c (white dashed circles) indicated in (e) corresponds to N. A.=1.0. The calculations were courtesy provided by Dr. A. Bruyant (LNIO-UTT).

in the vicinity of θ_c, indicating that our Fourier filtering rejects a negligible portion of the scattered diagram. Note that all angles below θ_c were included in the calculations. All the experimental images are rotated to compensate for a 45° tilt of the outport of our microscope.

3.6.2 Radiation diagrams of dimer nanoparticles

For an antenna consisting of more than one nanoparticle, the radiation pattern becomes more complicated and geometry-dependent. Arrangement of strongly interacting Yagi-Uda like nanoantennas were predicted to significantly modify molecular radiation patterns [58]. A different separation between a dipole antenna and a fluorescent molecule results in a considerable variation of the molecular radiation [56].

In the following, we investigated the radiation pattern of the dimer antenna already discussed in the early sections of this chapter. A 50μm pinhole was inserted to spa-

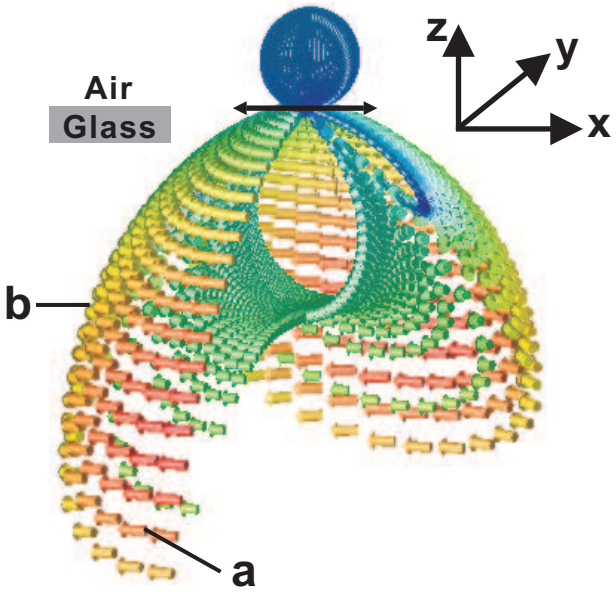

Fig 3.17: Field distribution of a dipole at the air/glass interface. The double arrow represents the orientation of the dipole. The single arrows indicate the electric field vectors. The two zones labeled 'a' and 'b' correspond to the field polarizations measured in Fig. 3.16 (see text for details). The calculation was courtesy provided by Gérard Colas des Francs.

tially filter off-axis scattering. For a coupled dimer (66nm in diameter and a 35nm gap), Fig. 3.18(a) and (d) show the emission diagrams with the polarization parallel to the dimer axis and perpendicular to it, respectively. The illumination wavelength is 633 nm. A two-lobe pattern indicates a dipolar-like emission concentrated at the critical angle similar to the single-particle antenna. In the presence of a collinear analyzer before the CCD, the diagrams stay constant expect for a slight decrease of intensity in the lobes (Fig. 3.18(b) and (e)). The crossed analyzer introduces a strong reduction of the intensity indicating a weak but non-negligible depolarized contribution. The radiation intensity displays a four-lobe pattern (Fig. 3.18(c) and (f)) originating from the orientation of field components of the particle (Fig. 3.17).

Figures 3.19(a)-(c) present a series of radiation patterns for dimer antennas with gap distance of 26, 68, and 126nm, respectively and for a polarization orientated along the dimer axis. The typical two-lobes pattern holds regardless of the gap width. The diameter of individual nanoparticles was fixed at 80nm and the illumination wavelength is 633nm. Figures 3.19 (d)-(e) show the radiation diagrams of 126 nm wide dimer gap analyzed through collinear and crossed analyzers, respectively. As expected from these weakly interacting particles, the radiation patterns are very similar to the single particle pattern.

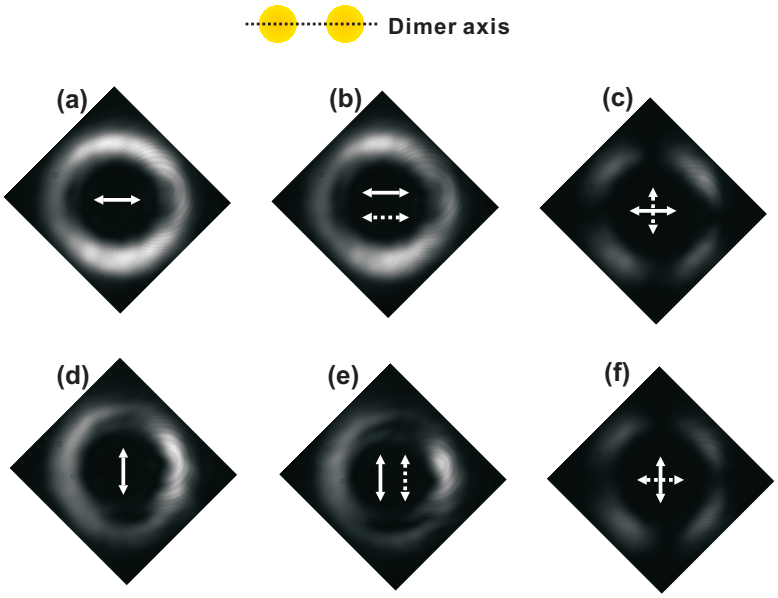

Fig 3.18: Partial scattering pattern for a dimer with gap of 35 nm and its constituted particle diameter of 66 nm. The broken black line shows the orientation of the dimer axis. The white thick arrows represent the incident polarizations and the broken arrows indicate the analyzer orientations. For coupled dimers, the angular emission patterns retain almost dipolar. $\lambda_{exc} = 633$ nm.

Figures 3.19(f)-(g) show the numerical simulations for gap values of 20nm and 150nm, respectively for the same particle diameter and polarization. Here too, the calculations suggest that the dimer antennas essentially have a dipolar response of their radiation pattern even for the strongly coupled dimer.

For the polarization perpendicular to the dimer axis, Figure 3.20 presents the diagrams of the same selected antennas shown in Fig. 3.19. These scattered diagrams have also two-lobe patterns. Interestingly, for a larger gap (> 100 nm) and for the perpendicular polarization, the scattered diagram of Fig. 3.20(c) shows an 90° rotated arrangement of two lobes compared to Fig. 3.20 (a) and (b). The numerical calculation for larger gaps (Fig. 3.20(e)) confirms this lobe-arrangement rotation with a reducing contrast between the intensity maxima and the minima within the lobes. This abnormality originates from the far-field interaction of two individual particles. This interaction mechanism will be discussed in the later.

Although two-lobe patterns are essential radiation characteristics for the dimers, the contrast of the lobes seems to display a variation with the gap width. Therefore, in order to quantify the contrast of the lobes, a parameter η accounting for the visibility of the

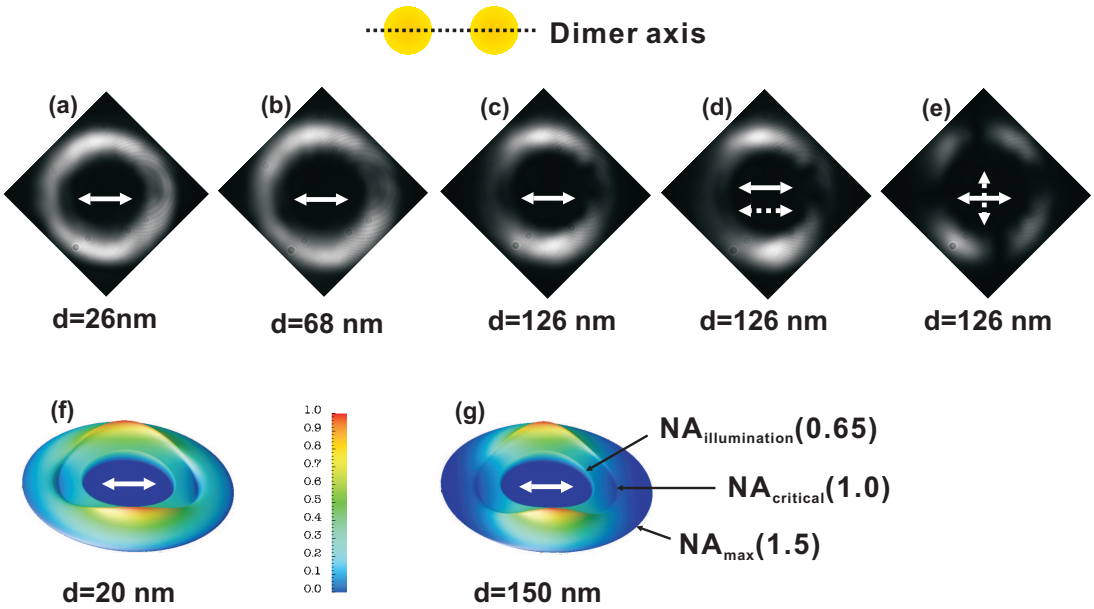

Fig 3.19: Radiation pattern for the dimers of diameter: ((a) 26 nm, (b)68 nm, (c)-(e) 126 nm, (f) 20 nm, (g)150 nm. (f) and (g) are the numerical simulations. λ_{exc} = 633 nm. The N. A. values corresponding to the illumination, the critical angle and the maximum are labeled in (g). The dimer axis is along the horizontal direction. The diameter of individual nanoparticles constituting the dimer is 80 nm. The white thick arrows represent the incident polarizations and the broken arrows indicate the analyzer orientations. The calculations were courtesy provided by Gérard Colas des Francs.

lobes is defined by:

$$\eta = \frac{I_{max} - I_{min}}{I_{max} + I_{min}}, \tag{3.9}$$

where I_{max} and I_{min} represent the maxima and the minima of the intensity within the lobes. η reflects the degree of the angular emission contrast and implies the ability of an optical antenna to radiate light in a certain direction. The measurement of η may be an experimental way to directly assess the directivity of an optical antenna. The value of η extracted from the colloidal particle (Fig. 3.16 (a)) and its corresponding simulation (Fig. 3.16 (e)) are in agreement at 0.5. A deviation of the value of η (η = 0.72) was, however, found for the reference single particle within the antennas array. The difference of η between the colloidal and the isolated lithographed particles may result from the different morphology of the particle. The measured evanescent scattering modes is highly sensitive to the morphology of the antenna [84].

Figure 3.21 shows the trend of η of the optical antennas for varying gaps and for the two orthogonal incident polarizations. For the polarization parallel to the dimer axis, η

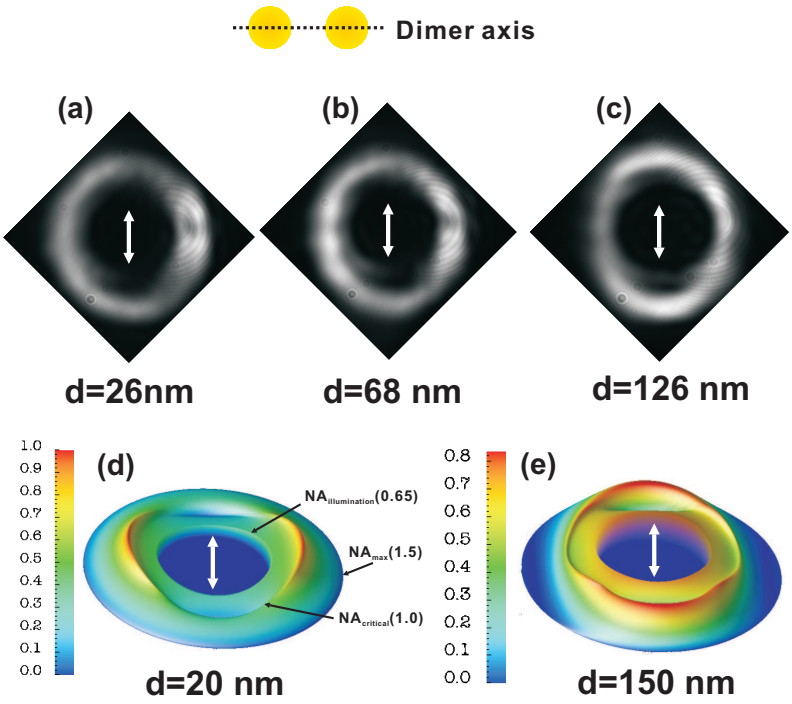

Fig 3.20: Partial radiation pattern for the dimers of diameter: (a) 26 nm, (b) 68 nm, (c) 20nm. The dimer axis is along the horizontal direction. The diameter of individual nanoparticles is 80 nm. The white thick arrows represent the incident polarizations. (c) is the numerical simulation. The N. A. values corresponding to the illumination, the critical angle and the maximum are labeled in (c). λ_{exc} = 633 nm. The calculations were courtesy provided by Gérard Colas des Francs.

increases with the gap distance and reaches a value comparable to the reference single particle (η=0.72). However, for the perpendicular polarization, η is closer to the value of the reference particle for the shortest dimer separation. The magnitude of I_{max} does not significantly vary across the different antennas (variation $< 5\%$). Therefore, the value of η is mainly governed by I_{min} according to Eq. 3.9. In order to account for the different behaviors of the trends of η for the two orthogonal polarizations (Fig. 3.21), let us start from the evolution of the near-field to the far-field radiation patterns (Fig. 3.22) of a dipole.

The radiation pattern of a free-space dipole displays an evolution as a function of propagating distance r as illustrated in Fig. 3.22 [135]. The cross-section of the pattern undergoes a 90° rotation from near field ($r/\lambda = 0.001$) to far field ($r/\lambda = 1$). In our case, the particles/dipoles are sitting on a dielectric interface and the radiated power is mainly emitted in the denser medium around θ_c [114, 86]. Backward scattering can be neglected (see Fig. 2.13 in chapter 2). In the presence of the substrate, the pattern of an in-plane

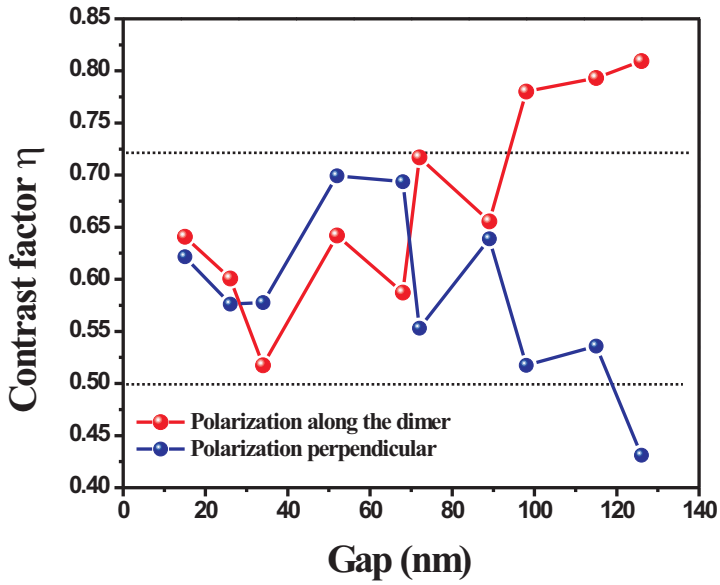

Fig 3.21: Evolution of the contrast factor η with the gap distance for the two incident polarization. The two dashed lines correspond to the contrast factor values of 0.5 and 0.72, respectively.

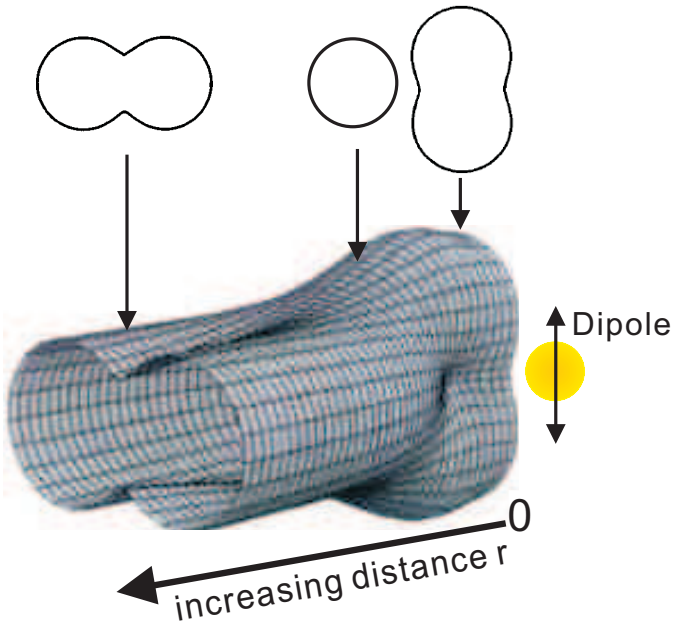

Fig 3.22: An overview of the electric field (lower panel) at different distance r from a dipole in free space. Three cross sections (upper panels) indicate from right to left the radiation patterns at $r = 0.001\lambda$, $r = 0.375\lambda$ and $r = \lambda$, respectively. A 90° rotation of the pattern is observed from near field to far field. Image adapted from Ref. [135].

dipole also displays a 90° rotation from near-field distance to far-field zone [113].

The trend of η could be explained by the field overlap between the two particles constituting the dimer. For a polarization along the dimer, the dipolar characteristics of the emission is perturbed for strongly interacting particles (small gaps). For the perpendicular polarization, however, the far-field radiation patterns of the two particles are aligned with the main axis of the dimer, and the overlap interaction (interference) is therefore stronger for larger gaps (evolving to far-field interaction distance). The evolution of η for this polarization also confirms this hypothesis.

3.7 Conclusion

Optical antennas attract more attentions for their wide applications such as photonic devices, biomedical domains for their ability to operate light at nanoscale volume. To gain more insights of the optical response of antennas, we have performed a study on the optical properties of gold colloidal nanoparticles, disk-shaped gold particles and pairs of such particles prepared by electron beam lithography. By referring to radio-antennas theory, we measured and defined important parameters such as the operating wavelength, the gain, the detuning and the radiation patterns characterizing the behaviors of antennas. We analyzed the spectra of the localized surface plasmon resonance by varying gap separations and particle sizes for two orthogonal incident polarizations. We found that for small gap distances, a pronounced spectral redshift is observed for the polarization along the dimer axis, and a weaker redshift for the polarization perpendicular to the dimer axis. The gain was measured by integrating the differential scattering cross-section using a developed scanning confocal microscopy. The detuning factor is obtained by differentiating the resonance spectral positions and the excitation line. By correlating the detuning and the gain, we demonstrated that the gain decreases as the detuning increases. We also investigated the radiation patterns of single and dimer antennas and found that the measured radiation diagrams remain essentially dipolar. A contrast factor of the radiation patterns is also introduced to describe the influence of interparticle interaction on the directivity of antennas. One important advantage of our approach is allowing us to rapidly characterize the antennas at the excitation frequency without requirement of reporter molecules or nonlinear phenomena to probe the antenna's response. Therefore, our approach is completely non-pertubative.

From this chapter, we gained better insights on the passive control on the antennas by designing the parameters. However, another idea comes into our minds: can we tune the

optical antennas without changing their morphologies? On the basis of this, we present in the following chapter a manner to actively control the behaviors of the antennas by an external command.

Chapter 4

Active control of optical antennas

We have seen in the previous chapter that some of the parameters defining an optical antenna can be adjusted by varying the morphology of the device. In particular, the scattering response of the antennas is governed by the position of the surface plasmon resonances existing in the structure. By analogy with radiowave antennas, changing the design parameters is equivalent to physically adjust the antenna length of a radio receiver to a desired broadcasting station. A more appropriate way of tuning the receiver is to change the electrical lump circuitry of the radio-frequency antenna in order to modify its load and therefore its operating frequency.

In the optical domain, the load of antenna can also be *relatively* adjusted by changing the medium in which the antenna is operated. Engheta et al. [136, 137, 138] introduced an interesting optically equivalent circuitry. These authors defined a material with a positive dielectric constant as an optical capacitor, a material with a negative dielectric constant as equivalent to an optical inductor and a material characterized by a non-zero imaginary part of the dielectric constant as an optical resistor. It is therefore conceptually straightforward to tune the optical antennas by playing with the load medium.

Continuing the analogy with a radio receiver, a particular emitting station is selected by a tuner which essentially consists in a resonant RLC load circuit with a variable capacitor to adjust the resonance frequency. In the optical domain, the variable capacitor can take the form of a medium characterized by an externally controllable index of refraction. An active control of the spectral responses of optical antennas was demonstrated by reversible electrochemical and molecular switches [139, 140] or by an electrooptically active medium [141, 142, 143] but did not focus on measuring the effect of the medium on the other essential parameters defining an optical antenna (gain, emission diagram...). In this chapter, we present an external control over the elastic scattering properties of single

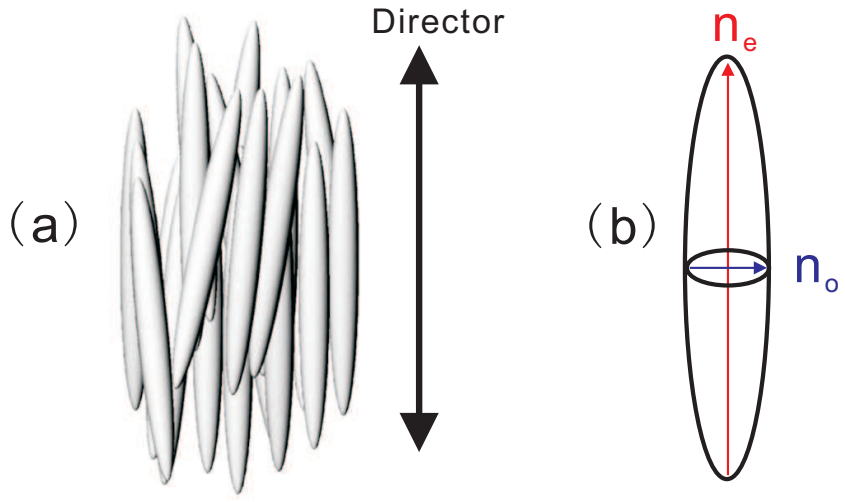

Fig 4.1: (a) Sketch of a small volume of the nematic liquid crystals molecules with the average orientation defined as the director. Image adapted from Ref. [145]. (b) Schematic of ordinary and extraordinary refractive indexes (n_o and n_e) for nematic liquid crystals.

and dimer antennas constituted of two interacting gold nanoparticles. This is achieved by electrically modifying an anisotropic load medium surrounding the antennas. The load medium chosen is a nematic liquid crystal (LC). A liquid crystal is a state of matter that falls in between a conventional liquid and a solid crystal. A LC may act as liquid, but its molecules may be arranged in a crystallin manner. There are several types of LC phases such as nematic, smectic and cholesteric phases, classified according to the amount of order of LC molecules in the material. LCs possess optical and dielectric anisotropies that can be adjusted by external parameters (electric field, temperature,...). In our work, nematic liquid crystals are chosen for their simple molecular ordering and ease of alignment by an external electric field as well as for their transparency in the visible spectrum regime.

4.1 Nematic liquid crystal

Nematic comes from the Greek $\nu\eta\mu\alpha$ meaning thread [144]. Nematic liquid crystals consist of rod-like molecules without any positional order as shown in Fig. 4.1(a). The long axes of neighboring molecules are aligned approximately to one another. The average orientation for a small volume of molecules is defined as the director. Nematic liquid crystal is an anisotropic substance characterized by an ordinary index n_o and an extraordinary one n_e. Figure 4.1 (b) illustrates a sketch of the index ellipsoid for an uniaxial positive

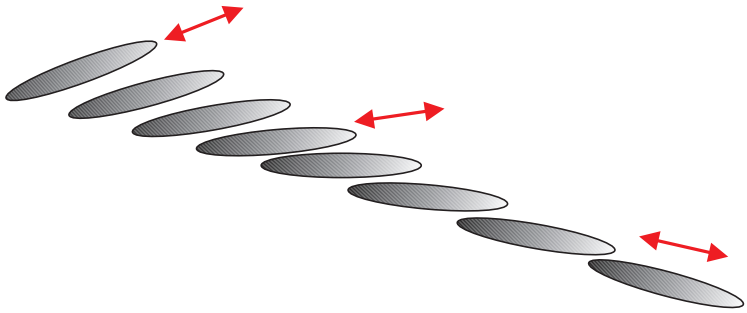

Fig 4.2: The light polarization follows adiabatically the rotation of the optical axis and the outgoing polarization remains the polarization either parallel or perpendicular to it. The beam passes through LCs from top left to bottom right sides. The arrows represent the polarization.

birefringent molecule. The nematic LC used in our work is E7 © (from Merck). This LC has a positive birefringence of Δ n = 0.2179 ($n_e = 1.7354$ and $n_o = 1.5175$ at $\lambda = 644$ nm and T = 20°C [146]) which gives a large anisotropy and offers therefore a large potential of control of the load medium. A few properties of LC cell are briefly introduced in the following.

Fréedericksz's transitions

The orientations of the LCs directors can be adjusted by an external electric field. When the electric field with a sufficient strength is applied, the orientation of LC molecules will realign in response to the external field. This phenomenon is called Fréedericksz's transitions which lead to a distortion of the director field and therefore a polarization change of traveling light. The extent of the polarization modification depends on the strength of the applied electric field. The positive dielectric anisotropy of the LC molecules results in a parallel alignment of the extraordinary refractive index and the electric field line.

Mauguin's theorem

One of the important properties of nematic LCs is their ability to modify the polarization of light. When light travels through liquid crystals with ordinary or extraordinary polarization, its polarization is rotated along the slow distortion of the director. This is referred to as Mauguin's theorem. Figure 4.2 shows an illumination of Mauguin's theorem. When a linear polarization of incident light is parallel or perpendicular to a neutral optical axis at the entrance plane, it will follow adiabatically the rotation of the optical

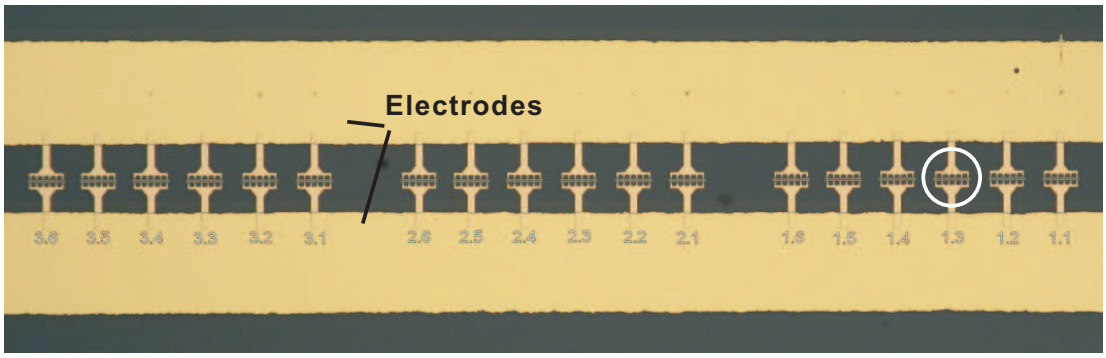

Fig 4.3: Optical micrograph of the sample. Two transverse macroscopic gold electrodes between which there are close-up electrode systems (e. g. circled) and a series of optical antennas (invisible here). See Fig. 4.4 for more details about the sample.

axis at the exit plane by remaining linearly polarized either perpendicular or parallel to it. Mauguin's theorem is often used for analyzing the optical behavior of LC in the presence of twisted structures. It will also be used later on to explain some of the results.

4.2 Liquid crystal cell

The fabrication of the optical antennas embedded in a liquid crystal cell required a two-step fabrication procedure. A first step consisted on the fabrication of the macroscopic gold electrodes for electrically controlling the orientation of the LC director with an in-plane command. We used traditional UV lithography with mask contact to fabricate the layout of the electrodes (macroscopic transverse electrodes in Fig. 4.3). A 100 nm-thick gold layer was then deposited on the substrate prior to the lift-off of the resist. The second fabrication step consisted at fabricated close-up electrode systems (e.g. area circled in Fig. 4.3) and a series of optical antennas by electron-beam lithography already introduced before. The fabrication of the electrodes and optical antennas was done in a collaborative mode with Prof. Bachelot (LNIO, Troyes). Figure 4.4(a) shows a scanning electron micrograph of the selected area (circled in Fig. 4.3) of the sample. The macroscopic planar gold electrodes are separated by a 3.5 μm gap. Optical antennas are located at the center of the gap. The marked numbers (1-6) within the electrodes are for labeling the corresponding zone of the antennas between the electrodes. The axis of dimers orients alternatively, i.e., parallel to (x-direction) and perpendicular to (y-direction) the electrodes as schematically depicted in Fig. 4.4(b). The first particle on the left side is a single particle and will serve as a reference antenna to define the gain G. By design,

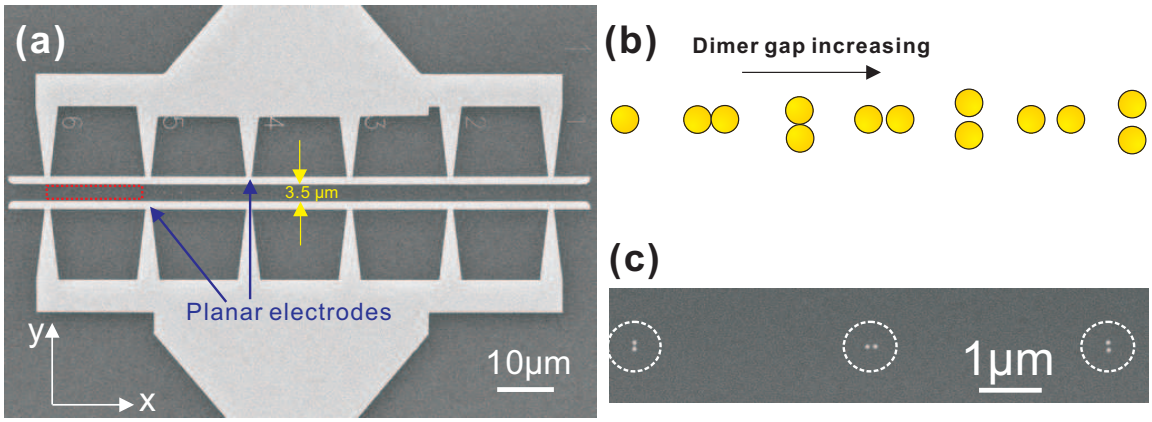

Fig 4.4: (a) Scanning electron micrograph of the selected area (circled in Fig. 4.3) sample. The planar gold electrodes are separated by a 3.5 μm gap. The dimer optical antennas are located at the center of the gap. Particle diameter is $\sim$ 70 nm with interparticle distance varying stepwise from contact to 100 nm (from left to right) for dimer antennas. (b) Schematic of the zone boxed in (a). The left antenna is the single reference particle. The orientation of the dimer (parallel or perpendicular to the electrodes) is alternating for each antenna. (c) Scanning electron micrograph of three dimer antennas (dashed circles) within the zone boxed in (a).

the dimer antennas consist of two identical elements (nanodisks) with a diameter and thickness of approximate 70 and 40nm, respectively. The spacing is varied in the range of 0 to 100 nm. Figure 4.4(c) displays several dimers within the zone boxed in Fig. 4.4(a). The pitch between the dimers was kept constant at 3μm in order to neglect the mutual optical interaction of adjacent dimers. Note that we have not used an ITO layer deposited on the glass substrate since ITO is conductive and would form a short circuit between the electrodes. Therefore, we cannot obtain higher resolution SEM images of dimers since highly gathered electron charges on the bare glass substrate strongly affect the quality of micrograph. The whole sample was then immersed in a nematic liquid crystal E7 © and then capped by a glass slide ($\sim$ 0.17 mm) schematically represented in Fig. 4.5. The thickness of LC layer between two glass slides is $\sim$ 6μm and was adjusted by a spacer layer of latex beads.

4.3 Medium characterization

In our sample, we have not used any alignment-assisted layer [142] or pre-functionalized the surface of gold particles [147] to control the orientation of the LC molecules. The antennas embedded in such a layer or coated by a chemical material would reduce their

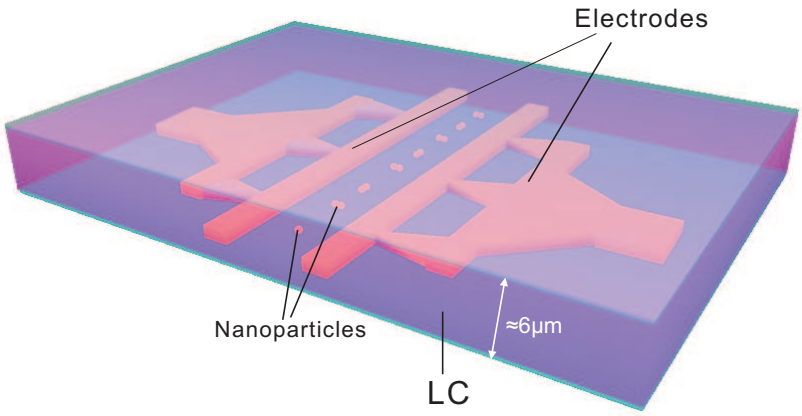

Fig 4.5: Schematic of the LC cell: the electrodes and the antennas are immersed in nematic liquid crystals. The top and the bottom substrates are glass slides ($\sim$ 0.17mm thick). The thickness of LC layer measures $\sim 6\mu$m.

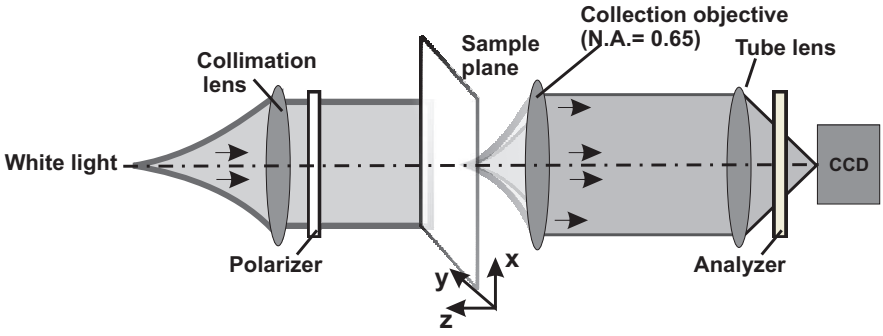

Fig 4.6: Experimental scheme for measuring the polarization response of the cell by transmission and with crossed polarizers.

effective surface interacting with LCs and therefore the influence of LCs on the antennas. In addition, the use of chemical material will introduce a perturbative effect on the scattering properties of the antennas. Before characterizing the optical antennas themselves, preliminary experiments on the polarization properties of the cell were performed by using a crossed-polarized bright-field transmission microscope. An illustration of the configuration is shown in Fig. 4.6. Briefly, the cell was mounted on an inverted optical microscope and illuminated by a bright-field condenser. The polarization was controlled by a simple polarizer. The transmittance of the cell was collected by a low N.A. objective (N. A. = 0.65) and detected by a Charge Couple Device (CCD) camera placed in the image plane. The polarization state at the output of the cell was analyzed with a polarizer located before the CCD camera.

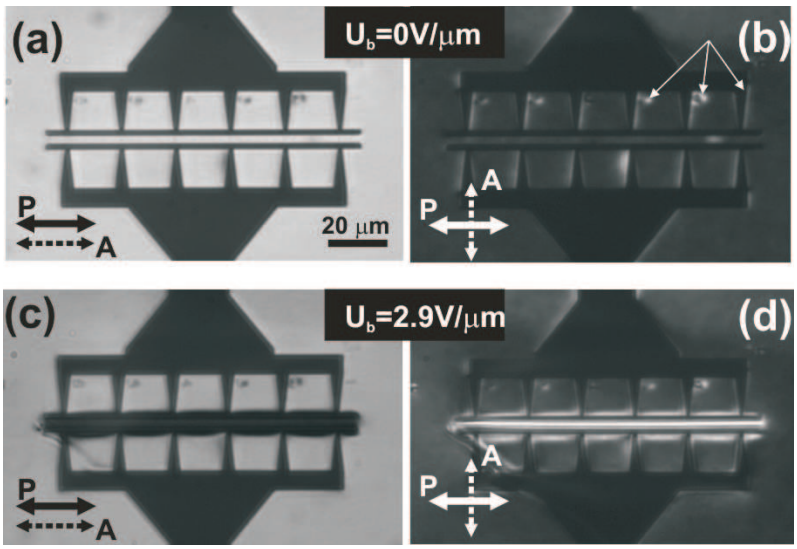

Fig 4.7: Bright-field images of the LC cell at a null bias with (a) collinear polarizer (P, thick arrow) and analyzer (A, dashed arrow) and (b) crossed orientations. (c,d) Same configuration at an electric field of 2.9 V/μm.

4.3.1 Original state of LC molecules

There is a priori no previous knowledge of the ordering of the LC molecules neither at the surface of the antenna nor within the bulk of the cell. Figure 4.7 (a) and (b) show images of the transmitted intensity through the LC cell under a null bias with collinear and crossed analyzers, respectively. In the transmission images, the electrode pattern is well recognized as a dark region because of the finite transmission of the gold layer. Of course, the optical antennas remain indistinguishable from the large transmitted background. It is interesting to note that despite the lack of pre-alignment layer, there is no indication of the presence of domains or domains walls within the field of view indicating a homogeneous orientation of the LC molecules. For the analyzer perpendicular to the polarizer (Fig. 4.7 (b)), there is an obvious extinction of the transmission in the regions embedded in the liquid crystal. This indicates that the light passing through the cell did not acquire a significant retardance. We have varied the orientation of the incident polarization by steps of 45° and verified that the extinction was always obtained for the crossed analyzer. If the cell does do not significantly change the incident polarization under a null bias, it indicates that the index of refraction of the cell is constant (isotropic-like medium). The molecules have therefore arranged under a homeotropic alignment (director perpendicular to the interface) with n_e oriented along the incident plane as illustrated in Fig. 4.8(a). Small contrast differences are visible at some peculiar areas nearby the electrodes (arrows)

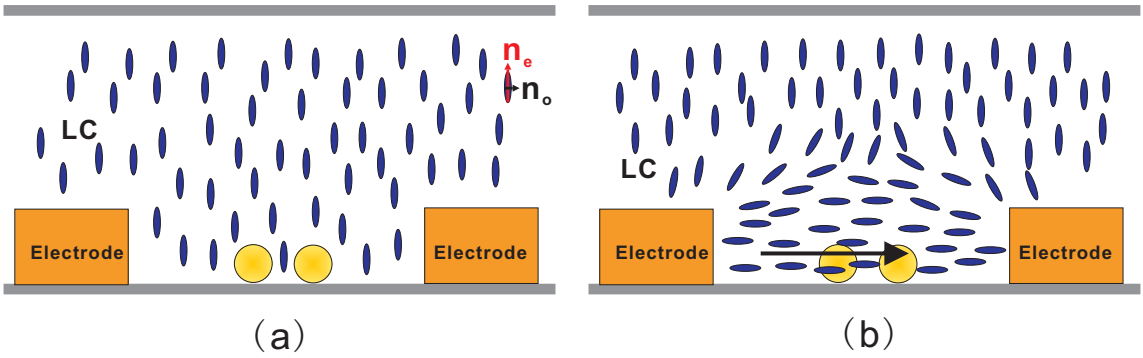

Fig 4.8: Sketch of cross-section of the LC cell with director orientation distribution under (a) a null bias and (b) a bias of 2.9 V/μm applied between the electrodes. The LC director is aligned along the electric field lines joining the two planar electrodes. The arrow represents the electric field.

in Fig. 4.7(b). We believe that the sharp edges of the electrodes are locally affecting the orientation of the LC [148, 149] leading thus to a local change in light polarization.

4.3.2 Electric field induced LC molecules states

In order to observe the response of the LCs to an external electric field, we electrically biased the cell. The electrodes were connected to a function generator. An alternating square waveform at 1 kHz frequency was chosen as it is usually used for LC devices [150]. The response time of the molecules is on the order of tens of millisecond [151], so they do not follow the waveform and will only react to the root mean square of the amplitude. This protocol limits the electrolysis and electrophoresis of the cell and avoid a precipitation of LCs.

Figure 4.7 (c) and (d) display transmission images recorded under the same combinations of polarizer and analyzer with an electric field $U_b = 2.9$ V/μm. For the analyzer parallel to the incident polarization, Fig. 4.7 (c) shows an optical contrast similar to that in Fig. 4.7 (a) except for the zone between the electrodes where the electric field lines are rotating the LC molecules. There is an obvious extinction of the light transmitted in the gap indicating effectively a change of polarization triggered by LC orientation. Figure 4.8(b) illustrates this effect. The directors in the gap underwent an out-of-plane 90° orientation to align the n_e index parallel to the sample plane and perpendicular to the electrode. The molecules located outside the electrode system remain unaffected by the bias since they are at an equipotential. We note that the electric field lines pattern is rather inhomogeneous between the electrodes and it is only at the center of the gap

that the director is in-plane. Further above, and close to the electrodes the molecules are oriented with a complex in-plane and out-of-plane orientations.

Figure 4.7 (d) shows a bright contrast in the gap for the analyzer perpendicular to the polarizer. This confirms that the bias-induced realignment of LCs in the gap region results in a change in the polarization of light passing through the gap.

4.4 Controlling optical antenna's differential scattering cross section

From the considerations above, we understand that when the cell is biased, the polarization at the exit of the cell is modified from that at the entrance of the cell. As the incident polarization undergoes a change through the biased cell, the exact state of polarization impinging the optical antenna is difficult to assess. We will therefore assume in the following that the polarization at the exit of the cell is the same as the one experienced by the antennas since the optical antennas are resting at the bottom of the cell.

To demonstrate a control over the scattering properties of optical antennas by an external electrical command, we have investigated the individual responses of the optical antennas boxed in Fig. 4.4(a). In order to simplify the results, we aimed at two orthogonal polarizations states seen by the antenna corresponding to x- or y- orientation of the dimer axis.

Figure 4.9 shows the distribution of intensity scattered off the optical antennas for two polarizations and for three different biases applied to the electrodes. The top panel sketches the corresponding antenna geometries. The first bright spot on the left side represents the scattered signal from the single particle and will be considered as the reference antenna. At a null bias, Fig. 4.9 (a) shows the x-oriented dimers have a 2-fold higher scattered intensity I_{scat} compared to both the reference antenna and the y-oriented dimers. Profile of the intensity taken through the center of the optical antennas is shown in Fig.4.10. The magnitude of I_{scat} for parallel dimers does not significantly depend on the dimer-gap range considered here and is consistent with the results exposed in chapter 3.

For $U_b = 0.71$ V/μm (Fig. 4.9 (b)), we observe a 30% and 40% reduction of the intensity scattered by the reference and the x-oriented dimers, respectively, while the intensity from the y-oriented dimers is typically increased by 60% (Fig. 4.10). Figure 4.9(c), corresponding to $U_b = 2.57$ V/μm, the intensities of the reference and of the x-oriented dimers

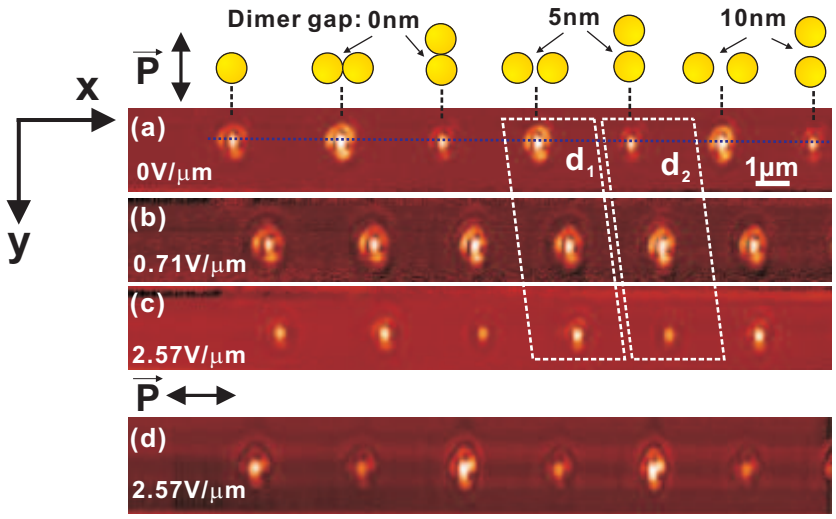

Fig 4.9: (a) Two dimensional intensity distribution of the light scattered by the antennas (boxed area in Fig. 4.4 (a)) obtained with a linear polarization perpendicular to the electrodes and for three values of U_{bias}: (a) 0V/μm, (b) 0.71 V/μm, and (c) 2.57 V/μm. (d) The polarization is parallel to the electrodes and U_{bias} = 2.57 V/μm. The top panel shows the corresponding antennas. $d1$ and $d2$ are two selected dimers of interest. Dashed line taken along the center of the antennas is used for intensity profiling in Fig. 4.10.

are comparable to the case of a null bias. However, the y-oriented dimers display a more than 2-fold decrease of I_{scat}. This 2-fold reduction of the intensity when the polarization is aligned with the axis of the dimer is confirmed in Fig. 4.9(d) for the orthogonal polarization.

4.5 Detuning and relative gain

In order to interpret the modification of I_{scat} by U_b, two phenomena are taken into account. To the difference with the previous chapter, the antennas are immersed in an index-varying medium with a dielectric constant comparable to the glass substrate. The consequence is that this high index medium leads to a significant alteration of scattered angular distribution inside the substrate. The second phenomenon is the concept introduced in Chapter 3. The variation of I_{scat} can be also understood in terms of a detuning factor $|\Delta\lambda| = |\lambda_{laser} - \lambda_{sp}|$, which defines the difference between the excitation wavelength λ_{laser} and the spectral position of the dimers' longitudinal and transverse surface plasmon resonances $\lambda_{sp}^{L,T}$ [128, 130, 152]. These resonances depend on the local refractive index, and for liquid crystals, on the applied voltage [153]. In order to account for this

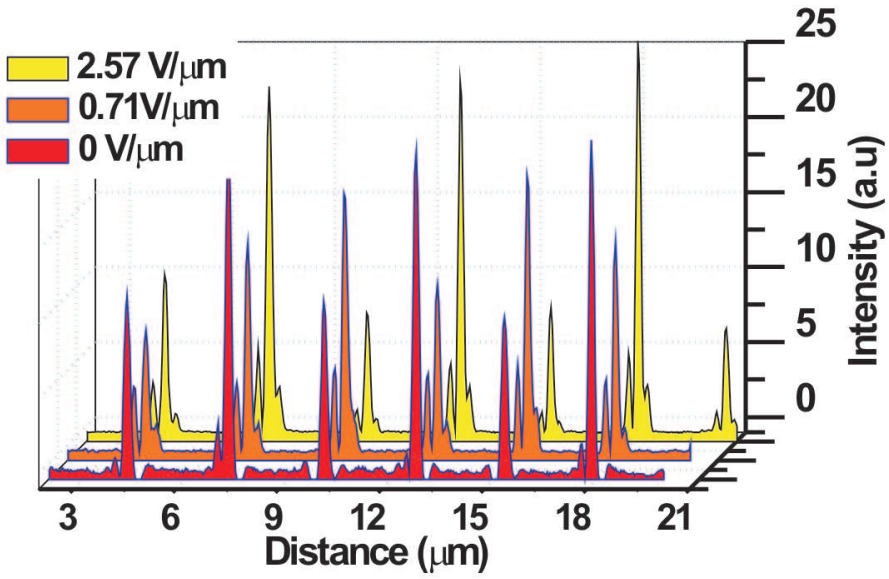

Fig 4.10: Intensity profiles taken from Fig. 4.9 (a-c) of the antennas for the three biasing conditions.

dependance, we chose two dimers labeled d_1 and d_2 (boxed area of Fig. 4.9) characterized by two orthogonal orientation. Figure 4.11 shows the position of the surface plasmon resonance λ_{sp}^{T} for d_2 excited along its transverse polarization and for two biases. The graph illustrates a red shift from λ_{sp}^{T}=645 nm to λ_{sp}^{T}=670 nm when the electric field is increased from 0 to 2.57 V/μm. This red shift, already observed by Müller *et al.*, was discussed in terms of an increased molecular density [141]. Considering the position of the resonance and the conclusions of the previous chapter, I_{scat} is larger for the x-oriented dimers because the laser wavelength (633 nm) is closer to the transverse resonances ($\sim$645 nm) than the red-shifted longitudinal plasmon. Figure 4.12 shows the non-monotonous evolution of I_{scat} for the dimer d_2 ($I_{scat}^{d_2}$) and for the reference antenna (single particle) (I_{scat}^{ref}) as a function of U_{bias}. The intensity scattered from the reference antenna has a weak dependence on U_{bias} with an average amplitude of 10 $\pm$ 2 (arbitrary unit) and point to point variations below 30%. The shaded area in Fig.4.12 delimiting 0.5 V/μm $< U_{bias} <$ 1.25 V/μm is the electric field range where $I_{scat}^{d_2}$ undergoes the most dramatic changes. This range corresponds to the onset of Fréedericksz's transitions between two stationary orientations [153, 154]. This transition range was systematically observed for all the antennas.

Figure 4.12 also shows the detuning factor $|\Delta\lambda|$ where λ_{sp}^{L} was extracted from dark-field spectroscopy [153]. Here too, the largest detuning is obtained for field values comprised within the Fréedericksz's transitions (shadowed area). The exact orientation of the LC

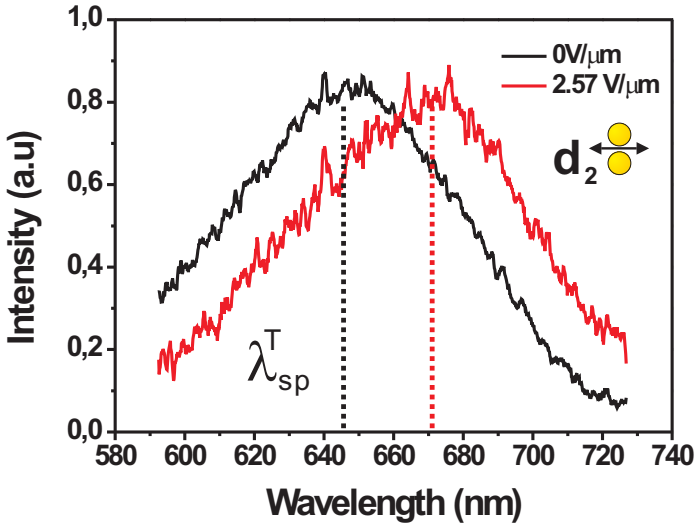

Fig 4.11: Scattered spectra of the λ_{sp}^{T} of d_2 for two biases. The polarization is perpendicular to the dimer axis.

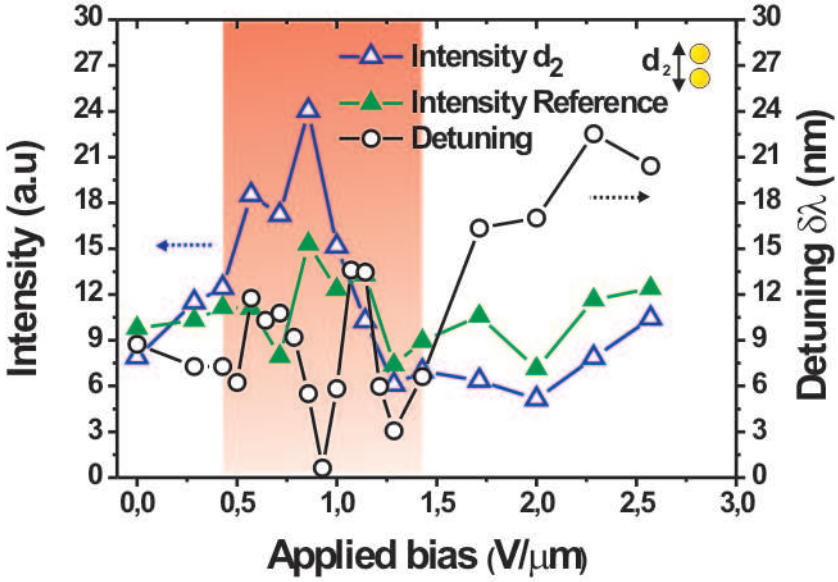

Fig 4.12: Intensity and detuning as a function of U_{bias} for the reference and the dimer d_2 with a y-polarization. Shadowed area represents the onset of the Fréedericksz's transitions.

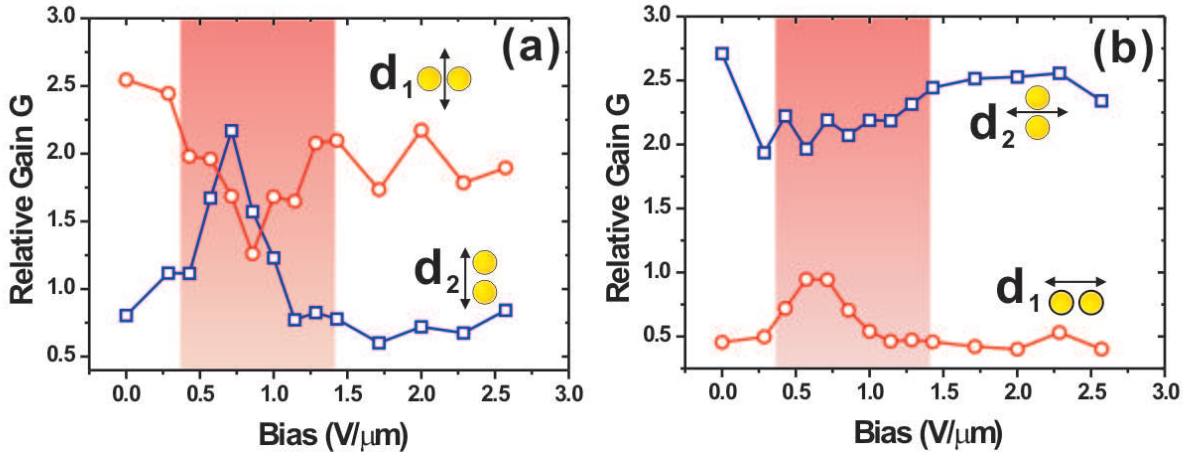

Fig 4.13: Relative gain G of d_1 and d_2 as a function of U_{bias} for (a) y and (b) x polarizations, respectively. The shadowed areas corresponds the onset of Fréedericksz's transitions.

molecules in the vicinity of the antenna is difficult to determine solely from spectroscopic data. However, for this range of U_{bias} and polarization alignment, the surface plasmon resonance has red-shifted by 25 nm from its position at null bias due to a locally higher refractive index. There is a clear opposite trend between the intensity scattered by d_2 and $|\Delta\lambda|$ indicating that I_{scat} is maximum when $|\Delta\lambda| \longrightarrow 0$. We therefore consider that detuning is probably more effective in modifying I_{scat} than the redirection of scattered power out of the detection angles.

4.5.1 Relative gain

One of the important properties of optical antennas is the relative gain G obtained by normalizing the response of an antenna by a reference measurement. Following the approach described in Chapter 3, the scattered intensity I_{scat}^{dimer} radiated by the dimer antennas are therefore normalized to that of the reference single-particle antenna. Figure 4.13 (a) and (b) show the U_{bias}-dependency of the relative antenna gain $G = I_{scat}^{dimer}/I_{scat}^{ref}$ for the two selected dimers d_1 and d_2 with two orthogonal polarizations. Two regimes can be distinguished in the evolution of the G versus U_{bias}. A first range of electric field is where G is significantly modified (shadowed areas). This range corresponds to the onset of Fréedericksz's transitions. A second bias regime located on either side of the Fréedericksz's transitions whereby G oscillates weakly around the value measured at a null bias. d_2 has a much lower G than antenna d_1 because the detuning for d_2 is important outside the Fréedericksz's region (Fig. 4.12).

On the contrary, G is significantly altered by the onset of Fréedericksz's transitions. G of d_1 decreases and reaches half of its magnitude at U_{bias}=0.85V/μm, however d_2 has 3-fold increase in G at U_{bias}=0.75V/μm because the excitation is close to the resonance ($\Delta\lambda \rightarrow 0$). According to the trend outlined by Fig. 4.12, the reorientation of the LC molecules makes the longitudinal plasmon resonance λ_{sp}^{L} closer to the excitation line λ_{laser}. This is confirmed by the evolution of d_2 for a x-polarization (Fig.4.13(b)), probing the transverse resonance λ_{sp}^{T}. Figure 4.13(b) shows a minimum G of d_2 around U_{bias}=0.75V/μm in the Fréedericksz's transitions region where d_1 has a maximum around U_{bias}=0.70V/μm. We note that these graphs represent the behavior of the antennas excited at a 633 nm laser line. The dependence and amplitude of G versus U_{bias} will be modified with a different laser (see Chapter 3).

4.6 Radiation pattern

To fully characterize the scattering properties of the antennas, we measured their scattering diagrams by detecting the angular distribution of the intensity in a conjugated Fourier plane (setup see Fig. 2.11). To the difference with the measurement performed in the previous chapters, the presence of the nearby electrodes generated a background signal. A 30μm pinhole was therefore inserted to spatially filter off-axis scattering.

4.6.1 Single particle antenna

Figures 4.14 shows the bias-dependance evolution of scattering diagram of the reference antenna radiated in the substrate. The diagrams represent the angular distribution of the intensity for a fixed polarization incident of the cell (y-direction). The inner edge of the diagrams corresponds to the beam stop measures N.A.$_{\mathrm{BS}}$=0.85 and the outer one N.A.$_{\mathrm{max}}$=1.45 (Fig. 4.14(a)). When the electrodes are biased, the orientation of the polarization of the incident light is modified as it travels through the cell (Mauguin's theorem). The previous chapter demonstrated the scattered diagram of small antennas essentially reproduces the emission of a dipole with a characteristic two-lobe pattern oriented perpendicular to the incident polarization. This two-lobe pattern is recognized in Fig. 4.14(a) confirming two conclusions from the previous sections. First, from the orientation of the two-lobe, the polarization at the antenna seems to be primarily oriented along the y direction and therefore did not change when passing through the cell. This is consistent with a homeotropic alignment at a null bias (polarization parallel to n_o

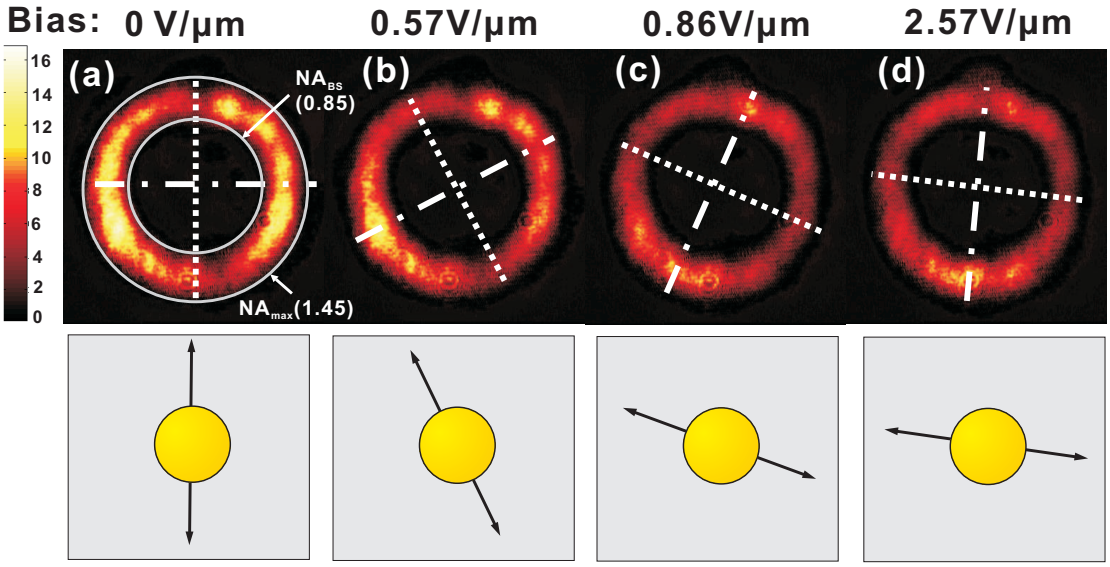

Fig 4.14: (a)-(d) False color CCD images of the angular distribution of the scattered intensity from the reference antenna as a function of electric field for a fixed incident polarization (y-direction). The bottom panel indicates the polarization (arrow) seen by the corresponding antenna, which is obtained by analyzing the two-lobe pattern (dotted and dash dotted lines). The calibration of the N. A. values is reported on the first diagram. The top panel shows the corresponding applied bias.

regardless of the incident orientation). Second, despite the presence of a high dielectric medium, a significant portion of the light is emitted in the substrate by forward scattering.

When U_{bias} increases, the LC director gradually aligns with field lines in a planar arrangement between the electrodes thus imposing a change of the polarization . The consequence of the change is the rotation of the two-lobe pattern as a function of U_{bias} observed in Fig. 4.14(b-c). Figure 4.14(d) shows that increasing U_{bias} above the Fréedericksz's transitions leads to a nearly 90° shift of the polarization. Note that the rotation occurs in the Fréedericksz's region and the diagram of Fig. 4.14(d) does not evolve for U_{bias} comprised between 1.42V/μm and 2.57V/μm because of a relative stable alignment of the director field. The rotation of the two-lobe pattern as a function of U_{bias} provides a means to electrically control *in-situ* the radiation diagram of a single optical antenna.

4.6.2 Dimer antenna

Figure 4.15 shows a series of scattering diagrams obtained for the dimer d_2 as a function of U_{bias}. To the difference to the previous measurement, the shift of polarization through the biased cell was pre-compensated in order to keep the polarization seen by the antenna

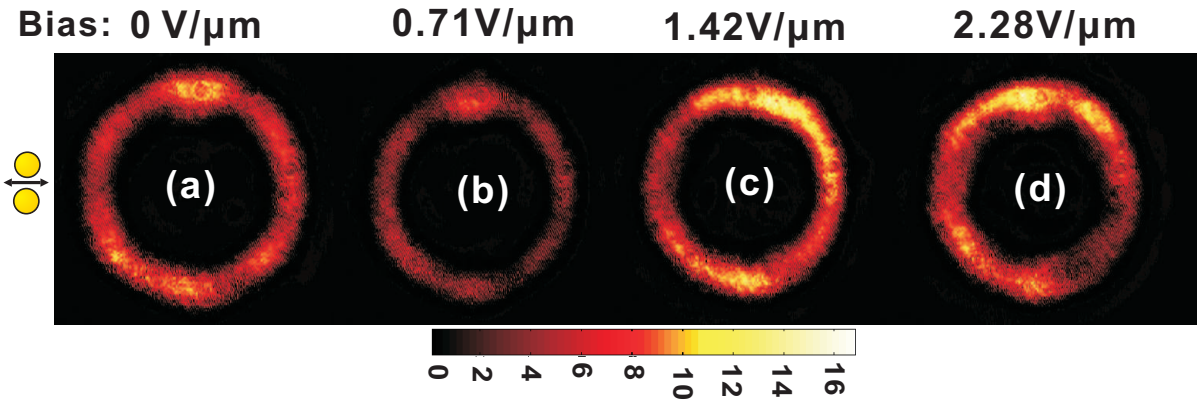

Fig 4.15: (a)-(d) Scattering diagrams for the antenna d_2 as a function of applied electric field U_{bias} and for a x polarization. The top panel shows the corresponding applied bias.

constant, here aligned along the x-direction.

At a null bias (Fig. 4.15(a)), the angular intensity distribution presents an ill-defined two-lobe pattern. This is consistent with the previous chapter where the near-field interaction between the individual particles constituting the dimer was affecting the contrast ratio η. Figure 4.15(b) shows the intensity distribution for U_{bias} comprised within the Fréedericksz's transitions. The azimuthal distribution of the light is rather homogeneous with an overall reduction of the received intensity. Despite some local inhomogeneities in the azimuthal distribution due to spatial filtering, the radiation diagrams do not drastically change their overall angular response with U_{bias} (Fig. 4.15(a-d)). The integrated intensity (Fig. 4.15(a) to (d)) follows the evolution of G of d_2 measured in Fig. 4.13(b). In particular, the reduced relative gain around the Fréedericksz's transitions is confirmed by Fig. 4.15(b) for U_{bias}=0.71V/μm.

4.7 Conclusion

In this chapter, we have demonstrated a control over the scattering response of individual optical antennas. The amount of detuning, the relative gain and the scattering diagram can be electrically adjusted. This command is achieved by modifying the load of the antenna, very much like the tuner in a radio receiver. In our investigations, the load in which the antenna is operating is a liquid crystal formulation chosen for its electro-optically activity and very large anisotropy. Our results showed that the variation of the response of the optical antenna is maximized for electric field corresponding to the onset of Fréedericksz's transitions and not necessarily at the largest applied bias. This fact

is promising for a perspective of application since Fréedericksz's transitions are usually triggered by weak electric field (<1V/μm in our case).

To continue with the radio-frequency analogy, it is interesting to remark that the capability of acting on the relative gain of an optical antenna offers a way to encode information in a nanoscale optical wireless device, very much like the amplitude-modulation (AM) used for transmitting data in a radio carrier wave. Although the time response of traditional liquid crystals is rather slow (tens of millisecond [155]), ferroelectric liquid crystals for instance have a faster response (ms) [156] that may be sufficient for applications where fast switching is not required.

Conclusions and perspectives

Optical antennas are devices capable of interfacing far-field radiation to interactions occurring at the nanoscale. This capability is inferred from fascinating optical properties characterizing optical antennas: field confinement, intensity enhancement, and radiation engineering. Therefore, a complete characterization of optical antennas became a necessity. Interestingly, this characterization is often performed by indirect means, for instance by looking at the modified response of an external emitter (fluorescence life time, ...). This method certainly brings a wealth of information about the *coupled* system, but fails to bring insight about the response of the antenna itself.

To overcome this limitation, we present in this thesis a series of measurements aimed at characterizing the main properties of individual optical antennas. Our approach relies on the determination of important parameters deduced from Rayleigh scattering. We have based our measurement on the detection of the differential scattering cross sections of optical antennas by developing novel experimental tools. The determination of the differential scattering cross section gives us some informations about the local density of electromagnetic modes supported by the devices which contain the complete optical response. We demonstrate our approach by imaging optical corral and stadium and showed reasonable agreement between the experimental maps and the calculated density of states.

We applied our principle to characterize optical antennas. In this thesis, we essentially focused on simple geometries, namely disk-shaped antennas and coupled antenna forming dimers. The optical responses of these antennas are discussed in the frame work of classical antenna theory notably by introducing concepts like gain, detuning and radiation pattern. We showed that these parameters can be adjusted by varying the morphology of the antennas (size, gap width) but also by the excitation conditions (wavelength, polarization). Drawing an analogy with radio-frequency antennas, this is equivalent at adjusting the length and orientation of a wire antenna on a receiver to detect a desired broadcasting station. The introduction of a tuner to match the impedance of the antenna to the equip-

ment greatly improved the bandwidth of receivers without changing the dimension of the antenna itself. We used a similar approach to actively command the scattering properties of optical antennas by using a controllable load medium. In our case, the adjusting parameter of the load is not a variable capacitor as in the case of a radio tuner, but its optical equivalent: the refractive index. We demonstrate that by electrically acting on the index of refraction in which the optical antenna is operating, the main characteristics of the antenna can be tuned and possibly modulated.

What are the different perspectives of the research presented here? For one, the geometries considered here were restricted to simple examples. Numerical calculations showed that multi-element antennas may respond beyond a dipolar response, notably by concentrating the angular distribution in well-defined domains in an optical equivalent of Yagi-Uda antenna. Figure 4.16(a) shows a scanning electron micrograph of fabricated gold Yagi-Uda optical antenna with its feed and parasitic elements. The geometry of the different parts was adjusted to an operating wavelength of 633 nm. Figure 4.16(b) and (c) show the spatial distribution of the differential scattering cross section for two polarization orientation. The images depict a complex intensity distribution because the footprint of the antenna is much larger than the detection and excitation focal areas. Figure 4.16(d) and (e) illustrate the angular distribution of the light scattered inside the substrate for the two polarizations considered. It is evident that the antenna is not functioning properly because the intensity distribution in the azimuthal plane is symmetric. The two vertical dark lines are the results of a Fraunhofer interference triggered by the presence of the parasitic elements.

This example nicely illustrates the limitation of our approach. A Yagi-Uda antenna (radiowave or optical regime) is essentially a near-field device. When operating as a transmitter or a receiver, the equipment is connected solely to the feed element. In our case, the feed and the adjacent elements are simultaneously excited because our excitation/detection is diffraction-limited. In order to characterize the scattering pattern of such an antenna, it is therefore necessary to use a local source. The precise placement of a molecule or a quantum dot at the feed point is extremely difficult. However, a near-field nanometer-size aperture tip can be positioned accurately above the structure and would allow a point-by-point analysis of the real emission diagram.

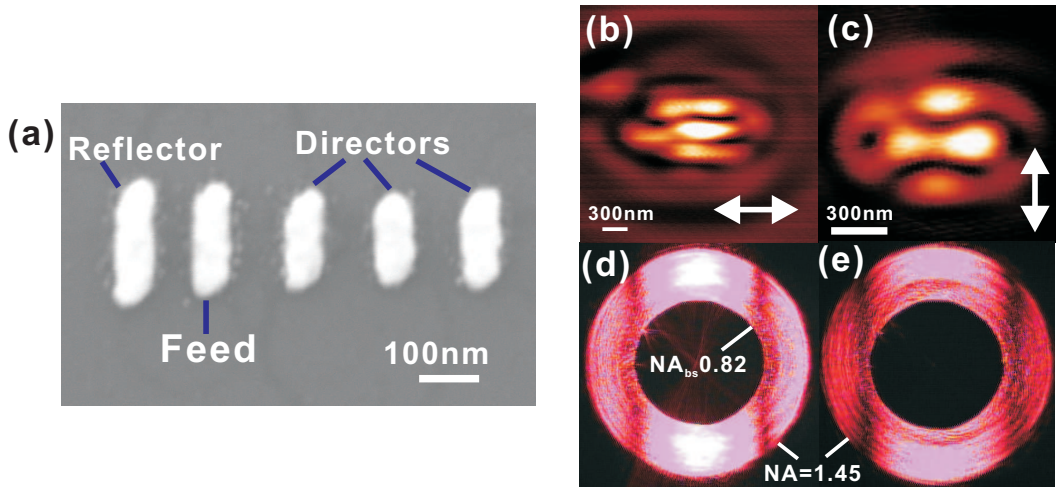

Fig 4.16: (a)Scanning electron micrograph of the optical equivalent of Yagi-Uda antenna. (b) and (c) Spatial distribution of the intensity scattered by the antenna for two polarizations (arrow). (d) and (e) are the corresponding scattering diagram recorded.

Bibliography

[1] J. Homola, S. S. Yee, and G. Gauglitz. Surface plasmon resonance sensors: review. *Sens. Actuat. B*, 54(1-2):3 – 15, 1999.

[2] H. Sota, Y. Hasegawa, and M. Iwakura. Detection of conformational changes in an immobilized protein using surface plasmon resonance. *Anal. Chem.*, 70(10):2019–2024, 1998.

[3] R. Slavík, J. Homola, and J. Ctyroký. Miniaturization of fiber optic surface plasmon resonance sensor. *Sens. Actuat. B*, 51(1-3):311–315, 1998.

[4] A. G. Brolo, R. Gordon, B. Leathem, and K. L. Kavanagh. Surface plasmon sensor based on the enhanced light transmission through arrays of nanoholes in gold films. *Langmuir*, 20(12):4813–4815, 2004.

[5] T. N. C. Venkatesan and K. Ogawa. Miniaturised, hybrid, 500 mb/s optical receiver package for data-link applications. *Electron. Lett.*, 15(6):171–172, 1979.

[6] S. M. Mansfield, W. R. Studenmund, G. S. Kino, and K. Osatot. High-numerical-aperture lens system for optical storage. *Opt. Lett.*, 18:305–307, 1993.

[7] A. S. Dvornikov, I. Cokgor, M. Wang, F. B. McCormick, Jr. S. C. Esener, and P. M. Rentzepis. Materials and systems for two photon 3-d rom devices. *IEEE Trans. Comp., Pkg., and Mfg. Techn., Part A,*, 20:203–211, 1997.

[8] S. Balslev, A. M. Jorgensen, B. Bilenberg, K. B. Mogensen, D. Snakenborg, O. Geschke, J. P. Kutter, and A. Kristensen. Lab-on-a-chip with integrated optical transducers. *Lab Chip*, 6:213–217, 2006.

[9] C. Huang, K. Bonroy, G. Reekmans, W. Laureyn, K. Verhaegen, I. De Vlaminck, L. Lagae, and G. Borghs. Localized surface plasmon resonance biosensor integrated with microfluidic chip. *Biomed. Microdevices*, 11:893–901, 2009.

[10] R. Corkish, M. A. Green, and T. Puzzer. Solar energy collection by antennas. *Sol. Energy*, 73(6):395 – 401, 2002.

[11] W. U. Huynh, J. J. Dittmer, and A. P. Alivisatos. Hybrid nanorod-polymer solar cells. *Science*, 295(5564):2425–2427, 2002.

[12] V. E. Ferry, L. A. Sweatlock, D. Pacifici, and H. A. Atwater. Plasmonic nanostructure design for efficient light coupling into solar cells. *Nano Lett.*, 8(12):4391–4397, 2008.

[13] M. Aeschlimann, M. Bauer, D. Bayer, T. Brixner, F. G. de Abajó, W. Pfeiffer, M. Rohmer, C. Spindler, and F. Steeb. Adaptive subwavelength control of nano-optical fields. *Nature*, 446:301–304, 2007.

[14] P. Vasa, C. Ropers andR. Pomraenke, and C. Lienau. Ultra-fast nano-optics. *Laser & Photon. Rev.*, 3:483–507, 2009.

[15] L. Novotny and S. J. Stranick. Near-field optical microscopy and spectroscopy with pointed probes. *Annu. Rev. Phys. Chem.*, 57:303–331, 2006.

[16] H. Heinzelmann and D. W. Pohl. Scanning near-field optical microscopy. *Appl. Phys. A*, 59:89–101, 1994.

[17] A. Bouhelier, M. R. Beversluis, and L. Novotny. Applications of field-enhanced near-field optical microscopy. *Ultramicroscopy*, 100(3-4):413 – 419, 2004. Proceedings of the Fifth International Conference on Scanning Probe Micrscopy, Sensors and Nanostructures.

[18] T. H. Taminiau, R. J. Moerland, F. B. Segerink, L. Kuipers, and N. F. van Hulst. $\lambda/4$ resonance of an optical monopole antenna probed by single molecule fluorescence. *Nano Lett.*, 7(1):28–33, 2007.

[19] J. Michaelis, C. Hettich, J. Mlynek, and V. Sandoghdar. Optical microscopy using a single molecule light source. *Nature*, 405:325, 2000.

[20] P. Bharadwaj, B. Deutsch, and L. Novotny. Optical antennas. *Adv. Opt. Photon.*, 1(3):438–483, 2009.

[21] J. Wessel. Surface-enhanced optical microscopy. *J. Opt. Soc. Am. B*, 2:1538–1540, 1985.

[22] X. Zhu and M. Ohtsu, editors. *"Near-field optics seen as an antennas problem", Near-field Optics: Principles and Applications*. Word Scientific, 2000.

[23] C. L. Du, Y. M. You, X. J. Zhang, K. Johnson, and Z. X. Shen. Polarization-dependent confocal imaging of individual ag nanorods and nanoparticles. *Plasmonics*, 4:217–222, 2009.

[24] F. Jackel, A. A. Kinkhabwala, and W. E. Moerner. Gold bowtie nanoantennas for surface-enhanced raman scattering under controlled electrochemical potential. *Chem. Phys. Lett.*, 446:339–343, 2007.

[25] N. Félidj, J. Aubard, G. Lévi, J. R. Krenn, M. Salerno, G. Schider, B. Lamprecht, A. Leitner, and F. R. Aussenegg. Controlling the optical response of regular arrays of gold particles for surface-enhanced raman scattering. *Phys. Rev. B*, 65(7):075419, 2002.

[26] N. A. Mirin and N. J. Halas. Light-bending nanoparticles. *Nano Lett.*, 9(3):1255–1259, 2009.

[27] L. Novotny. Effective wavelength scaling for optical antennas. *Phys. Rev. Lett.*, 98:266802, 2007.

[28] C. Hubert, A. Rumyantseva, G. Lerondel, J. Grand, S. Kostcheev, L. Billot, A. Vial, R. Bachelot, P. Royer, S. Chang, S. K. Gray, G. P. Wiederrecht, and G. C. Schatz. Near-field photochemical imaging of noble metal nanostructures. *Nano Lett.*, 5(4):615–619, 2005.

[29] J. P. Kottmann, O. J. F. Martin, D. R. Smith, and S. Schultz. Non-regularly shaped plasmon resonant nanoparticle as localized light source for near-field microscopy. *J. Microsc.*, 202:60–65, 2001.

[30] P. Galletto, P. F. Brevet, H. H. Girault, R. Antoine, and M. Broyer. Enhancement of the second harmonic response by adsorbates on gold colloids: The effect of aggregation. *J. Phys.Chem.B*, 103(41):8706–8710, 1999.

[31] A. Bouhelier, M. Beversluis, A. Hartschuh, and L. Novotny. Near-field second-harmonic generation induced by local field enhancement. *Phys. Rev. Lett.*, 90:013903, 2003.

[32] M. Lippitz, M. A. van Dijk, and M. Orrit. Third-harmonic generation from single gold nanoparticles. *Nano Lett.*, 5(4):799–802, 2005.

[33] S. V. Popruzhenko, D. F. Zaretsky, and W. Becker. Third harmonic generation by small metal clusters in a dielectric medium. *J. Phys. B: At. Mol. Opt. Phys.*, 39(23):4933–4943, 2006.

[34] M. R. Beversluis, A. Bouhelier, and L. Novotny. Continuum generation from single gold nanostructures through near-field mediated intraband transitions. *Phys. Rev. B*, 68(11):115433, 2003.

[35] R. Esteban, M. Laroche, , and J.-J. Greffet. Influence of metallic nanoparticles on upconversion processes. *J. Appl. Phys.*, 105:033107, 2009.

[36] H. R. Stuart and D. G. Hall. Absorption enhancement in silicon-on-insulator waveguides using metal island films. *Appl. Phys. Lett.*, 69:2327–2329, 1996.

[37] K. R. Catchpole and S. Pillai. Absorption enhancement due to scattering by dipoles into silicon waveguides. *J. Appl. Phys.*, 100(4):044504, 2006.

[38] M. Kirkengen, J. Bergli, and Y. M. Galperin. Direct generation of charge carriers in c-si solar cells due to embedded nanoparticles. *J. Appl. Phys.*, 102(9):093713, 2007.

[39] S. Pillai, K. R. Catchpole, T. Trupke, and M. A. Green. Surface plasmon enhanced silicon solar cells. *J. Appl. Phys.*, 101(9):093105, 2007.

[40] S. Nie and S. R. Emory. Probing single molecules and single nanoparticles by surface- enhanced raman scattering. *Science*, 275(5303):1102–1106, 1997.

[41] L. Qin, S. Zou, C. Xue, A. Atkinson, G. C. Schatz, and C. A. Mirkin. Designing, fabricating, and imaging raman hot spots. *Proc. Natl. Acad. Sci.*, 103(36):13300–13303, 2006.

[42] D. A. Genov, A. K. Sarychev, V. M. Shalaev, and A. Wei. Resonant field enhancements from metal nanoparticle arrays. *Nano Lett.*, 4(1):153–158, 2004.

[43] V. A. Markel, V. M. Shalaev, P. Zhang, W. Huynh, L. Tay, T. L. Haslett, and M. Moskovits. Near-field optical spectroscopy of individual surface-plasmon modes in colloid clusters. *Phys. Rev. B*, 59(16):10903–10909, 1999.

[44] S. Kühn, U. Håkanson, L. Rogobete, and V. Sandoghdar. Enhancement of single-molecule fluorescence using a gold nanoparticle as an optical nanoantenna. *Phys. Rev. Lett.*, 97:017402, 2006.

[45] P. Anger, P. Bharadwaj, and L. Novotny. Enhancement and quenching of single-molecule fluorescence. *Phys. Rev. Lett.*, 96:113002, 2006.

[46] P. Bharadwaj, P. Anger, and L. Novotny. Nanoplasmonic enhancement of single-molecule fluorescence. *Nanotechnology*, 18(4):044017, 2007.

[47] P. Mühlschlegel, H.-J. Eisler, O. J. F. Martin, B. Hecht, and D. W. Pohl. Resonant optical antennas. *Science*, 308(5728):1607–1609, 2005.

[48] S. Palomba, M. Danckwerts, and L. Novotny. Nonlinear plasmonics with gold nanoparticle antennas. *J. Opt. A: Pure Appl. Opt.*, 11:114030, 2009.

[49] O. L. Muskens, V. Giannini, J. A. Sánchez-Gil, and J.Gómez Rivas. Strong enhancement of the radiative decay rate of emitters by single plasmonic nanoantennas. *Nano Lett.*, 7(9):2871–2875, 2007.

[50] A. Wokaun, H.-P. Lutz, A. P. King, U. P. Wild, and R. R. Ernst. Energy transfer in surface enhanced luminescence. *J. Chem. Phys.*, 79(1):509–514, 1983.

[51] J. R. Lakowicz. Radiative decay engineering 5: metal-enhanced fluorescence and plasmon emission. *Analytical Biochemistry*, 337(2):171 – 194, 2005.

[52] M. Thomas, J.-J. Greffet, R. Carminati, and J. R. Arias-Gonzalez. Single-molecule spontaneous emission close to absorbing nanostructures. *Appl. Phys. Lett.*, 85(17):3863–3865, 2004.

[53] H. Kuhn. Classical aspects of energy transfer in molecular systems. *J. Chem. Phys.*, 53(1):101–108, 1970.

[54] F. Tam, G. P. Goodrich, B. R. Johnson, and N. J. Halas. Plasmonic enhancement of molecular fluorescence. *Nano Letters*, 7(2):496–501, 2007.

[55] E. Hao and G. C. Schatz. Electromagnetic fields around silver nanoparticles and dimers. *J. Chem. Phys.*, 120:357, 2004.

[56] T. H. Taminiau, F. D. Stefani, F. B. Segerink, and N. F. van Hulst. Optical antennas direct single-molecule emission. *Nature Photon.*., 2:234, 2008.

[57] W. Lukosz. Light emission by magnetic and electric dipoles close to a plane dielectric interface. iii radiation patterns of dipoles with arbitrary orientation. *J. Opt. Soc. Am.*, 69:1495–1503, 1979.

[58] J. Li, A. Salandrino, and N. Engheta. Shaping light beams in the nanometer scale: A yagi-uda nanoantenna in the optical domain. *Phys. Rev. B.*, 76:245403, 2007.

[59] H. F Hofmann, T. Kosako, and Y. Kadoya. Design parameters for a nano-optical yagi-uda antenna. *New J. Phys.*, 9(7):217, 2007.

[60] T. H. Taminiau, F. D. Stefani, and N. F. van Hulst. Enhanced directional excitation and emission of single emitters by a nano-optical yagi-uda antenna. *Opt. Express*, 16(14):10858–10866, 2008.

[61] P. Bharadwaj and L. Novotny. Spectral dependence of single molecule fluorescence enhancement. *Opt. Express*, 15(21):14266–14274, 2007.

[62] Y. Chen, K. Munechika, and D. S. Ginger. Dependence of fluorescence intensity on the spectral overlap between fluorophores and plasmon resonant single silver nanoparticles. *Nano Lett.*, 7:690–696, 2007.

[63] Y. Chen, K. Munechika, I. J.-L. Plante, A. M. Munro, S. E. Skrabalak, Y. Xia, and D. S. Ginger. Excitation enhancement of cdse quantum dots by single metal nanoparticles. *Appl. Phys. Lett.*, 93:053106, 2008.

[64] W. L. Barnes. Fluorescence near interfaces: the role of photonic mode density. *J. Mod. Opt.*, 45:661–699, 1998.

[65] J. P. Hoogenboom, G. Sanchez-Mosteiro, G. Colas des Francs, D. Heinis, G. Legay, A. Dereux, and N. F. van Hulst. The single molecule probe: Nanoscale vectorial mapping of photonic mode density in a metal nanocavity. *Nano Lett.*, 9:1189–1195, 2009.

[66] C. Chicanne, T. David, R. Quidant, J. C. Weeber, Y. Lacroute, E. Bourillot, A. Dereux, G. Colas des Francs, and C. Girard. Imaging the local density of states of optical corrals. *Phys. Rev. Lett.*, 88:097402, 2002.

[67] K. Joulain, R. Carminati, J. P. Mulet, and J. J. Greffet. Definition and measurement of the local density of electromagnetic states close to an interface. *Phys. Rev. B*, 68:245405, 2003.

[68] K. Joulain, J. P. Mulet, F. Marquier, R. Carminati, and J. J. Greffet. Surface electromagnetic waves thermally excited: Radiative heat transfer, coherence properties and casimir forces revisited in the near field. *Surf. Sci. Rep.*, 57(3-4):59 – 112, 2005.

[69] G. S. Agarwal. Quantum electrodynamics in the presence of dielectrics and conductors. iii. relations among one-photon transition probabilities in stationary and nonstationary fields, density of states, the field-correlation functions, and surface-dependent response functions. *Phys. Rev. A*, 11(1):253–264, 1975.

[70] G. Colas des Francs, C. Girard, J. C. Weeber, and Alain Dereux. Relationship between scanning near-field optical images and local density of photonic states. *Chem. Phys. Lett.*, 345:512–516, 2001.

[71] C. Girard. Near fields in nanostructures. *Rep. Prog. Phys.*, 68(8):1883–1933, 2005.

[72] A Dereux, Ch Girard, C Chicanne, G Colas des Francs, T David, E Bourillot, Y Lacroute, and J C Weeber. Subwavelength mapping of surface photonic states. *Nanotechnology*, 14:935–938, 2003.

[73] K. Imura, T. Nagahara, and H. Okamoto. Characteristic near-field spectra of single gold nanoparticles. *Chem. Phys. Lett.*, 400(4-6):500 – 505, 2004.

[74] J. Tersoff and D. R. Hamann. Theory of the scanning tunneling microscope. *Phys. Rev. B*, 31:805–813, 1985.

[75] M. F. Crommie, C. P. Lutz, and D. M. Eigler. Confinement of electrons to quantum corrals on a metal surface. *Science*, 262:218–220, 1993.

[76] E. J. Heller, M. F. Crommie, C. P. Lutz, and D. M. Eigler. Scattering and absorption of surface electron waves in quantum corrals. *Nature*, 369(6480):464–466, 1994.

[77] R. Carminati and J.J. Sáenz. Scattering theory of bardeen's formalism for tunneling: New approach to near-field microscopy. *Phys. Rev. Lett.*, 84:5156–5159, 2000.

[78] A. Dereux, Ch. Girard, and J.C. Weeber. Theoretical principles of near–field optical microscopies and spectroscopies. *J. Chem. Phys.*, 112:7775–7789, 2000.

[79] G. Colas des Francs, C. Girard, J. C. Weeber, C. Chicanne, T. David, A. Dereux, and D. Peyrade. Optical analogy to eletronic quatum corrals. *Phys. Rev. Lett.*, 86:4950, 2001.

[80] K. Imura, T. Nagahara, and H. Okamoto. Near-field optical imaging of plasmon modes in gold nanorods. *J. Chem. Phys.*, 122(15):154701, 2005.

[81] J. R. Guest, T. H. Stievater, Gang Chen, E. A. Tabak, B. G. Orr, D. G. Steel, D. Gammon, and D. S. Katzer. Near-Field Coherent Spectroscopy and Microscopy of a Quantum Dot System. *Science*, 293(5538):2224–2227, 2001.

[82] K. Matsuda, T. Saiki, S. Nomura, M. Mihara, Y. Aoyagi, S. Nair, and T. Takagahara. Near-field optical mapping of exciton wave functions in a gaas quantum dot. *Phys. Rev. Lett.*, 91(17):177401, 2003.

[83] K. Imura, T. Nagahara, and H. Okamoto. Imaging of surface plasmon and ultrafast dynamics in gold nanorods by near-field microscopy. *J. Phys. Chem. B*, 108:16344, 2004.

[84] L. Novotny. Allowed and forbidden light in near-field optics. i. a single dipolar light source. *J. Opt. Soc. Am. A*, 14(1):91–104, 1997.

[85] L. Novotny. Allowed and forbidden light in near-field optics. ii. interacting dipolar particles. *J. Opt. Soc. Am. A*, 14(1):105–113, 1997.

[86] H. F. Arnoldus and J. T. Foley. Spatial separation of the traveling and evanescent parts of dipole radiation. *Opt. Lett.*, 28(15):1299–1301, 2003.

[87] S. Underwood and P. Mulvaney. Effect of the solution refractive index on the color of gold colloids. *Langmuir*, 10(10):3427–3430, 1994.

[88] P. Mulvaney. Surface plasmon spectroscopy of nanosized metal particles. *Langmuir*, 12(3):788–800, 1996.

[89] M. M. Miller and A. A. Lazarides. Sensitivity of metal nanoparticle surface plasmon resonance to the dielectric environment. *J. Phys.Chem.B*, 109(46):21556–21565, 2005.

[90] K. Lance Kelly, Eduardo Coronado, Lin Lin Zhao, and Geoge C. Schatz. The optical properties of metal nanoparticles: The influence of size, shape, and dielectric environment. *J. Phys. Chem. B*, 107:668–677, 2003.

[91] C. F. Bohren and D. R. Huffman, editors. *Absorption and Scattering of Light by Small Particles*. Wiley & Sons, Inc., New York, 1998.

[92] H. C. van de Hulst. *Light scattering by small particles*. Dover Publications, Inc. New York, 1981.

[93] P. W. Barber, R. K. Chang, and H. Massoudi. Surface-enhanced electric intensities on large silver spheroids. *Phys. Rev. Lett.*, 50(13):997, Mar 1983.

[94] M. Meier and A. Wokaun. Enhanced fields on large metal particles: dynamic depolarization. *Opt. Lett.*, 8(11):581–583, 1983.

[95] A. Wokaun, J. P. Gordon, and P. F. Liao. Radiation damping in surface-enhanced raman scattering. *Phys. Rev. Lett.*, 48(14):957–960, Apr 1982.

[96] K. A.Willets and R. P. Van Duyne. Localized surface plasmon resonance spectroscopy and sensing. *Annu. Rev. Phys. Chem.*, 58:267–297, 2007.

[97] A. J. Haes and R. P. Van Duyne. A nanoscale optical biosensor: Sensitivity and selectivity of an approach based on the localized surface plasmon resonance spectroscopy of triangular silver nanoparticles. *J. Am. Chem. Soc.*, 124(35):10596–10604, 2002.

[98] L. S. Jung, C. T. Campbell, T. M. Chinowsky, M. N. Mar, and S. S. Yee. Quantitative interpretation of the response of surface plasmon resonance sensors to adsorbed films. *Langmuir*, 14(19):5636–5648, 1998.

[99] J. J. Mock, D. R. Smith, and S. Schultz. Local refractive index dependence of plasmon resonance spectra from individual nanoparticles. *Nano Lett.*, 3:485–491, 2003.

[100] S. K. Eah, H. M. Jaeger, G. P. Wiederrecht N. F. Scherer, and X. M. Lin. Plasmon scattering from a single gold nanoparticle collected through an optical fiber. *Appl. Phys. Lett.*, 86:031902, 2005.

[101] M. Futamata, Y. Maruyama, and M. Ishikawa. Local electric field and scattering cross section of ag nanoparticles under surface plasmon resonance by finite difference time domain method. *J. Phys. Chem. B*, 107:7607–7617, 2003.

[102] J. Zhu, Y. Wang, L. Huang, and Y. Lu. Resonance light scattering characters of core-shell structure of au-ag nanoparticles. *Physics Letters A*, 323(5-6):455 – 459, 2004.

[103] J. Chen, F. Saeki, B. J. Wiley, H. Cang, M. J. Cobb, Z. Y. Li, L. Au, H. Zhang, M. B. Kimmey, X. Li, and Y. Xia. Gold nanocages: Bioconjugation and their potential use as optical imaging contrast agents. *Nano Lett.*, 5(3):473–477, 2005.

[104] E. Hecht. *Optics*. Addison Wesley, 4 edition, 2001.

[105] S. Wilhelm, B. Gröbler, M. Gluch, and H. Heinz. *Confocal Laser Scanning Microscopy Principles*. C a r l Z e i s s Jena GmbH.

[106] L. Novotny, D. R. Grober, and 2001. K. Karrai **26**, 789. Reflected image of a strongly focused spot. *Opt. Lett.*, 26:789, 2001.

[107] V. Jacobsen, P. Stoller, C. Brunner, V. Vogel, and V. Sandoghdar. Interferometric optical detection and tracking of very small gold nanoparticles at a water-glass interface. *Opt. Express*, 14:405, 2006.

[108] K. Lindfors, T. Kalkbrenner, P. Stoller, and V. Sandoghdar. Detection and spectroscopy of gold nanoparticles using supercontinuum white light confocal microscopy. *Phys. Rev. Lett.*, 93(3):037401, Jul 2004.

[109] J. Knopp and M. F. Becker. Virtual fourier transform as an analytical tool in fourier optics. *Appl. Opt.*, 17(11):1669–1670, 1978.

[110] L. Dai, I. Gregor, I. von der Hocht, T. Ruckstuhl, and J. Enderlein. Measuring large numerical apertures by imaging the angular distribution of radiation of fluorescing molecules. *Opt. Express*, 13(23):9409–9414, 2005.

[111] A. L. Baudrion, F. de Léon-Pérez, O. Mahboub, A. Hohenau, H. Ditlbacher, F. J.Garcia-Vidal, J. Dintinger, T. W. Ebbesen, L. Martin-Moreno, and J. R. Krenn. Coupling efficiency of light to surface plasmon polariton for single subwavelength holes in a gold film. *Opt. Express*, 16:3420–3429, 2008.

[112] A. Drezet, A. Hohenau, D. Koller, A. Stepanov, H. Ditlbacher, B. Steinberger, F.R. Aussenegg, A. Leitner, and J.R. Krenn. Leakage radiation microscopy of surface plasmon polaritons. *Mater. Sci. Eng. B*, 149(3):220 – 229, 2008.

[113] A. Lieb, J. M. Zavislan, and L. Novotny. Single-molecule orientations determined by direct emission pattern imaging. *J. Opt. Soc. Am. B*, 21:1210, 2004.

[114] W. Lukosz and R. E. Kunz. Light emission by magnetic and electric dipoles close to a plane interface. i total radiated power. *J. Opt. Soc. Am.*, 67:1607–1614, 1977.

[115] G. Schider, J. R. Krenn, A. Hohenau, H. Ditlbacher, A. Leitner, and F. R. Aussenegg. Plasmon dispersion relation of au and ag nanowires. *Phys. Rev. B.*, 68:155427, 2003.

[116] E. R. Méndez, J.J. Greffet, and R. Carminati. On the equivalence between the illumination and collection modes of the scanning near-field optical microscope. *Opt. Comm.*, 142:7–13, 1997.

[117] G. Colas des Francs, C. Girard, J. C. Weeber, and A. Dereux. Relationship between scanning near-field optical images and local density of photonic states. *Chem. Phys. Lett.*, 345:512, 2001.

[118] S. Lal, N. K. Grady, G. P. Goodrich, and N. J. Halas. Profiling the near field of a plasmonic nanoparticle with raman-based molecular rulers. *Nano Lett.*, 6:2338, 2006.

[119] P. J. Schuck, D. P. Fromm, A. Sundaramurthy, G. S. Kino, and W. E. Moerner. Improving the mismatch between light and nanoscale objects with gold bowtie nanoantennas. *Phys. Rev. Lett.*, 94:017402, 2005.

[120] A. Bouhelier, R. Bachelot, G. Lerondel, S. Kostcheev, P. Royer, and G. P. Wiederrecht. Surface plasmon characteristics of tunable photoluminescence in single gold nanorods. *Phys. Rev. Lett.*, 95:267405, 2005.

[121] J. N. Anker, W. P. Hall, O. Lyandres, N. C. Shah, J. Zhao, and R. P. V. Duyne. Biosensing with plasmonic nanosensors. *Nature Mater.*, 7:442, 2008.

[122] A. Alù and N. Engheta. Hertzian plasmonic nanodimer as an efficient optical nanoantenna. *Phys.Rev.B*, 78(19):195111, 2008.

[123] T. Klar, M. Perner, S. Grosse, G. von Plessen, W. Spirkl, and J. Feldmann. Surface-plasmon resonances in single metallic nanoparticles. *Phys. Rev. Lett.*, 80(19):4249–4252, May 1998.

[124] W. Rechberger, A. Hohenau, A. Leitner, J. R. Krenn, B. Lamprecht, and F. R. Aussenegg. Optical properties of two interacting gold nanoparticles. *Opt. Commun.*, 220(1-3):137 – 141, 2003.

[125] O. L. Muskens, V. Giannini, J. A. Sánchez-Gil, and J.Gómez Rivas. Optical scattering resonances of single and coupled dimer plasmonic nanoantennas. *Opt. Express*, 15:17736, 2007.

[126] Th. A. Milligan. *Modern Antenna Design.* John Wiley & Sons, Inc, 2005.

[127] R. Ruppin. Surface modes of two spheres. *Phys. Rev. B*, 26(6):3440–3444, 1982.

[128] H. Tamaru, H.I Kuwata, H. T. Miyazaki, and K. Miyano. Resonant light scattering from individual ag nanoparticles and particle pairs. *Appl. Phys. Lett.*, 80:1826, 2002.

[129] K.-H. Su, Q.-H. Wei, X. Zhang, J. J. Mock, D. R. Smith, and S. Schultz. Interparticle coupling effects on plasmon resonances of nanogold particles. *Nano Lett.*, 3(8):1087–1090, 2003.

[130] P. Nordlander, C. Oubre, E. Prodan, K. Li, and M. I. Stockman. Plasmon hybridization in nanoparticle dimers. *Nano. Lett.*, 4:899, 2004.

[131] I. Romero, J. Aizpurua, G. W. Bryant, and F. Javier García De Abajo. Plasmons in nearly touching metallic nanoparticles: singular response in the limit of touching dimers. *Opt. Express*, 14(21):9988–9999, 2006.

[132] T. Atay, J. H. Song, and A. V. Nurmikko. Strongly interacting plasmon nanoparticle pairs: From dipole-dipole interaction to conductively coupled regime. *Nano Lett.*, 4:1627–1631, 2004.

[133] Brian Stout, J. C. Auger, and Alexis Devilez. Recursive t matrix algorithm for resonant multiple scattering: applications to localized plasmon excitations. *J. Opt. Soc. Am. A*, 25(10):2549–2557, 2008.

[134] A. L. Lereu, G. Sanchez-Moistero, P. Ghenuche, R. Quidant, and N. F. Van Hulst. Individual gold dimers investigated by far- and near-field imaging. *J. Microsc.*, 229:245, 2008.

[135] V. Sandogdhar. Trends and developments in scanning near-field optical microscopy. *Nanometer Scale Science and Technology*, pages 65–119, (IOS Press, Amsterdam, 2001).

[136] N. Engheta, A. Salandrino, and A. Alù. Circuit elements at optical frequencies: Nanoinductors, nanocapacitors, and nanoresistors. *Phys. Rev. Lett.*, 95(9):095504, 2005.

[137] A. Alù and N. Engheta. Input impedance, nanocircuit loading, and radiation tuning of optical nanoantennas. *Phy. Rev. Lett.*, 101:043901, 2008.

[138] N. Engheta. Circuits with Light at Nanoscales: Optical Nanocircuits Inspired by Metamaterials. *Science*, 317(5845):1698–1702, 2007.

[139] Y. R. Leroux, J. C. Lacroix, K. I. Chane-Ching, C. Fave, N. Felidj, G. Levi, J. Aubard, J. R. Krenn, and A. Hohenau. Conducting polymer electrochemical switching as an easy means for designing active plasmonic devices. *J. Am. Chem. Soc*, 127(46):16022–16023, 2005.

[140] Y. B. Zheng, Y. W. Yang, L. Jensen, L. Fang, B. K. Juluri, A. H. Flood, P. S. Weiss, J. F. Stoddart, and T. J. Huang. Active molecular plasmonics: Controlling plasmon resonances with molecular switches. *Nano Lett.*, 9(0):819, 2009.

[141] J. Müller, C. Sonnichsen, H. von Poschinger, G. von Plessen, T. A. Klar, and J. Feldmann. Electrically controlled light scattering with single metal nanoparticles. *Appl. Phys. Lett.*, 81(1):171–173, 2002.

[142] K. C. Chu, C. Y. Chao, Y. F. Chen, Y. C. Wu, and C. C. Chen. Electrically controlled surface plasmon resonance frequency of gold nanorods. *Appl. Phys. Lett.*, 89(10):103107, 2006.

[143] P. R. Evans, G. A. Wurtz, W. R. Hendren, R. Atkinson, W. Dickson, A. V. Zayats, and R. J. Pollard. Electrically switchable nonreciprocal transmission of plasmonic nanorods with liquid crystal. *Appl. Phys. Lett.*, 91(4):043101, 2007.

[144] P. G. de Gennes. *The physics of liquid crystals*. Clarendon Press, 1993.

[145] T. Scharf. *Polarized light in liquid crystals and polymers*. John Wiley & Sons, 2007.

[146] W. C. Hung, W. H. Cheng, M. S. Tsai, Y. C. Juan, I. M. Jiang, and P. Yeh. Surface plasmon enhanced diffraction in cholesteric liquid crystals. *Appl. Phys. Lett.*, 90(18):183115, 2007.

[147] G. M. Koenig, B. T. Gettelfinger, J. J. de Pablo, and N. L. Abbott. Using localized surface plasmon resonances to probe the nanoscopic origins of adsorbate-driven ordering transitions of liquid crystals in contact with chemically functionalized gold nanodots. *Nano Lett.*, 8(8):2362–2368, 2008.

[148] B. Jérôme. *Rep. Prog. Phys.*, 54:391–451, 1991.

[149] R R. J. Ondris-Crawford, G. P. Crawford, S. Zumer, and J. W. Doane. Curvature-induced configuration transition in confined nematic liquid crystals. *Phys. Rev. Lett.*, 70(2):194–197, 1993.

[150] P. A. Kossyrev, A. Yin, S. G. Cloutier, D. A. Cardimona, D. Huang, P. M. Alsing, and J. M. Xu. Electric field tuning of plasmonic response of nanodot array in liquid crystal matrix. *Nano Lett.*, 5(10):1978–1981, 2005.

[151] H. Ren, S.-T. Wu, and Y.-H. Lin. Single glass substrate liquid crystal device using electric field-enforced phase separation and photoinduced polymerization. *Appl. Phys. Lett.*, 90(19):191105, 2007.

[152] C. Huang, A. Bouhelier, G. Colas des Francs, A. Bruyant, A. Guenot, E. Finot, J.-C. Weeber, and A. Dereux. Gain, detuning, and radiation patterns of nanoparticle optical antennas. *Phys. Rev. B*, 78:155407, 2008.

[153] J. Berthelot, A. Bouhelier, C. Huang, J. Margueritat, G. Colas des Francs, E. Finot, J. C. Weeber, A. Dereux, S. Kostcheev, H. I. E. Ahrach, A. L. Baudrion, J. Plain, R. Bachelot, P. Royer, and G. P. Wiederrecht. Tuning of an optical dimer nanoantenna by electrically controlling its load impedance. *Nano Lett.*, 9:3914–3921, 2009.

[154] V. Fréedericksz and V. Zolina. Forces causing the orientation of an anisotropic fluid. *Trans. Faraday Soc.*, 29:919–930, 1933.

[155] I. C. Khoo. *Liquid crystals*. Wiley, 2 edition, 2007.

[156] K. S. Choi, H. W. Kim, J. Y. Kim, T. M. Kim, Y. B. Kim, and J.-D. Kim. Electro-optical response of ferroelectric liquid crystal cells with photo-dimerization alignment layer. *Opt. Mater.*, 21(1-3):651 – 656, 2003.

List of publications

- *Surface plasmon interference excited by tightly focused laser beams,*
  A. Bouhelier, F. Ignatovich, A. Bruyant, C. Huang, G. Colas des Francs, J. -C. Weeber,A. Dereux, G. P. Wiederrecht, and L. Novotny. Opt. Lett. 32, 2535 (2007).

- *Far-field imaging of the electromagnetic local density of optical states,*
  C. Huang, A. Bouhelier, G. Colas des Francs, G. Legay, J. -C. Weeber, A. Dereux. Opt. Lett. 33, 300 (2008).

  This paper is highlighted in *Nature photonics* 2, 134 (2008)

- *Gain, detuning, and radiation patterns of nanoparticle optical antennas,*
  C. Huang, A. Bouhelier, G. Colas des Francs, A. Bruyant, A. Guenot, E. Finot, J. -C. Weeber, and A. Dereux. Phys. Rev. B 78, 155407 (2008).

- *Measuring the differential cross section of Gold nanoparticles,*
  C. Huang, A. Bouhelier, G. Colas des Francs, G. Legay, J. -C. Weeber, A. Dereux. Proceedings of the SPIE, vol 7032 (2008).

- *Tuning of an optical dimer nanoantenna by electrically controlling its load impedance*,
  J. Berthelot, A. Bouhelier, C. Huang, J. Margueritat, G. Colas-des-Francs, E. Finot, J. -C. Weeber, A. Dereux, S. Kostcheev, H. I. E. Ahrach, A. -L. Baudrion, J. Plain, R. Bachelot, P. Royer and G. P. Wiederrecht. Nano Lett. 9, 3914-3921 (2009).

  This paper is highlighted in *Nature Photonics* 4, 6 - 7 (2010).

- *External control of the scattering properties of a single optical nano-antenna,*
  C. Huang, A. Bouhelier, J. Berthelot, G. Colas-des-Francs, E. Finot, J. -C. Weeber, A. Dereux, S. Kostcheev, A.-L. Baudrion, J. Plain, R. Bachelot, P. Royer and G. P. Wiederrecht. Appl. Phys. Lett. in progress.